Transport through a Tight Binding Chain with Periodically Driven Impurities

Florin Hemmann

Masterarbeit in Physik
angefertigt im Physikalischen Institut

vorgelegt der
Mathematisch-Naturwissenschaftlichen Fakultät
der
Rheinischen Friedrich-Wilhelms-Universität
Bonn

Dezember 2022

I hereby declare that this thesis was formulated by myself and that no sources or tools other than those cited were used.

Bonn, 21.12.2022 .....
Date

F. Hemmann .....
Signature

1. Gutachterin: Prof. Dr. Corinna Kollath
2. Gutachterf: Prof. Dr. Stefan Linden

Acknowledgment

I would like to thank Prof. Dr. Corinna Kollath for giving me the opportunity to pursue this interesting master thesis project in her research group. Moreover, I would like to thank her and Dr. Ameneh Sheikhan for the supervision and the many helpful discussions which were a great support in advancing with my project.

I would like to thank the whole research group for creating a very pleasant atmosphere. Special thanks go to Dr. Ameneh Sheikhan, Dr. Anne-Maria Visuri, Dr. Franco Lisandrini, Dr. Neda Ahmadi and Karin Haderlein for proof-reading my thesis and for some helpful tips on English grammar. Also, many thanks go to Karin Haderlein, Luisa Tolle and Simon Wittum for being great office mates to share scientific discussions and coffee breaks with.

Furthermore, I would like to thank Prof. Dr. Stefan Linden for being the second examiner of this thesis.

Contents

CHAPTER 1

Introduction

Dynamical control of quantum systems is an essential requirement for the design of electronic devices on the nanoscale. Recent progress in experimental techniques has enabled the realization of nanoscale quantum systems with a high degree of control and coherence [1–3]. To study characteristics of such quantum matter systems, ultracold quantum gases in optical lattices have proven to be a versatile platform [4]. The insertion of a small number of impurities into such quantum gases [5] and the control of individual lattice sites by means of external fields [6, 7] renders highly localized manipulation of these quantum systems possible.

In experimental setups, dynamical control of quantum systems is typically achieved by means of external time-periodic fields [8], such as laser light [6, 7] or AC gate voltages [3]. Floquet theory provides a powerful method to understand such time-periodic systems [9–12]. Moreover, Floquet engineering of quantum systems has been employed to tune system parameters in order to achieve a plethora of interesting phenomena, such as dynamical localization [13], photon assisted tunneling [14], artificial magnetic fields [15] and induced phase transitions [16].

In the context of engineering future nanoelectronics, a strong focus lies on the study of transport phenomena. In such electronic systems of discrete nature, the tight binding model has been demonstrated to be a useful tool to analyze transport phenomena, e. g. in quantum dot arrays [17] and molecular electronic devices [18].

On the one hand, driven tight binding models have been studied by means of Floquet analysis in systems where the external periodic field is applied to the entire system [19, 20]. In contrast, the effects of an external field impinging only on a small region of the system can be investigated. To this end, Thuberg et al. [21] studied transport phenomena of the tight binding model with a single periodically driven impurity. For well-tuned parameters, they predicted the formation of bound states in the continuum which lead to a total destruction of tunneling through the impurity site. This effect was related to Fano interference, which occurs when a propagating state interacts with discrete energy levels and which produces transmission resonances with an asymmetric line shape. Such Fano resonances have previously attracted attention in the context of transport in continuous systems with oscillating potential barriers [22–24] and quantum pumps [25].

Reyes et al. [26] extended the model of [21] by additionally considering a non-homogeneous hopping amplitude to the impurity site. This model is expected to better describe possible experimental realizations where the tunneling amplitude to an impurity may be suppressed or enhanced. They found that this change in hopping amplitude alters the energy of the Fano resonance and can eliminate or

restore the resonance, depending on the energy of the resonance with respect to the continuum. A further extension of the locally driven tight binding chain was regarded in [27], where an additional interaction between multiple fermionic particles was considered. In this Fermi-Hubbard model, at strong attractive interactions, the formation of pairs is observed, whose transport properties differ significantly from those of single particles. This difference was utilized to design pair and single particle filters.

In this thesis, the tight binding chain with a driven impurity [21, 26] is extended by adding a second driven impurity site to the system. The resulting model of two periodically driven impurities in a tight binding chain is introduced in chapter 2. The following chapter 3 gives an introduction to the concepts of Floquet theory which are then applied to the driven tight binding chain in chapter 4. We find that in the Floquet formalism, the system's periodic time dependence is mapped onto a virtual spatial dimension. The one-dimensional time-periodic system is thus transformed into a two-dimensional time-independent system which consists of an infinite number of replicas of the original chain. These copies lie at different equidistant energies and couple to each other at the impurity sites.

To gain analytic insight into the Floquet transformed multichannel system, in chapter 5, the high frequency limit is considered, where the energy of the driving frequency $\hbar\omega$ is much larger than the bulk hopping amplitude which sets the internal energy scale of the tight binding system. In this limit, the original model reduces to an effective one-dimensional system where the external driving field induces modified tunneling amplitudes to the impurities. We show that in the continuum limit of small spacing between adjacent sites, this high frequency model behaves like a continuous system of two delta potential peaks representing the impurities. With this analogy in mind, we find several striking transport characteristics of the high frequency model, such as perfect transmission which is accompanied by a cavity-mode-like enhancement of the wavefunction in between the impurities. Furthermore, we demonstrate that, for a critical value of the effective hopping amplitude to the impurities, perfect transmission at zero momentum arises as a threshold anomaly.

In the final chapter 6, we return to the full Floquet picture derived in chapter 4 where particle transmission is determined by solving a multichannel scattering problem. To this end, an analogue multichannel continuous model is derived. Then, after summarizing previous results on single impurity transport [21, 23, 26], we find that Fano resonances also occur in the model with two driven impurities. At sufficiently large driving amplitudes however, the effects of Fano interference compete with effects that are associated to the cavity in between the impurities. Similar to the cavity modes found in the high frequency model, at lower frequencies, wavefunction enhancement occurs which leads to prominent transmission maxima.

CHAPTER 2

Model description

The goal of this thesis is the analysis of transport properties of a one-dimensional tight binding chain with two AC driven impurities. In this section, the Hamiltonian operator of this system is introduced and some general characteristics of tight binding systems are discussed before turning to the effect of the external drives in the next sections.

The Hamiltonian of the system at hand consists of two parts. The first part is the time-independent Hamiltonian of a tight binding chain with homogeneous hopping amplitude J. Only the tunneling amplitudes to the two impurities at sites $j = 0$ and $j = l$ differ from the homogeneous hopping and possess amplitudes J_1 and J_2, respectively. This Hamiltonian is thus given by

$$\hat{H}_{\text{tb}} = -J \sum_{j\neq -1,0,l-1,l} (\hat{c}_j^\dagger \hat{c}_{j+1} + \hat{c}_{j+1}^\dagger \hat{c}_j) - J_1 \sum_{j=-1,0} (\hat{c}_j^\dagger \hat{c}_{j+1} + \hat{c}_{j+1}^\dagger \hat{c}_j) - J_2 \sum_{j=l-1,l} (\hat{c}_j^\dagger \hat{c}_{j+1} + \hat{c}_{j+1}^\dagger \hat{c}_j) \tag{2.1}$$

where $\hat{c}_j^\dagger$ creates and $\hat{c}_j$ annihilates a particle at site j. Since this thesis only deals with single particles one does not need to specify whether it obeys Bose or Fermi statistics if not stated otherwise.

The second part of the Hamiltonian is given by two driving terms. They describe two oscillating chemical potentials at the impurity sites with driving frequency ω, amplitudes μ_1 and μ_2 and a relative phase ϕ. The time-dependent driving Hamiltonian is therefore given by

$$\hat{H}_{\text{drive}}(t) = -\mu_1 \cos(\omega t)\hat{c}_0^\dagger \hat{c}_0 - \mu_2 \cos\big(\omega t + \phi\big)\hat{c}_l^\dagger \hat{c}_l. \tag{2.2}$$

This entire system is thus described by the Hamiltonian

$$\hat{H}(t) = \hat{H}_{\text{tb}} + \hat{H}_{\text{drive}}(t). \tag{2.3}$$

and depicted in figure 2.1.

Due to the periodic external drive $H(t)$ is time-periodic with period $T = \frac{2\pi}{\omega}$. Very useful concepts to study such time-periodic systems are provided by Floquet theory. The principles of Floquet theory are introduced in section 3 and applied to the system at hand in section 4.

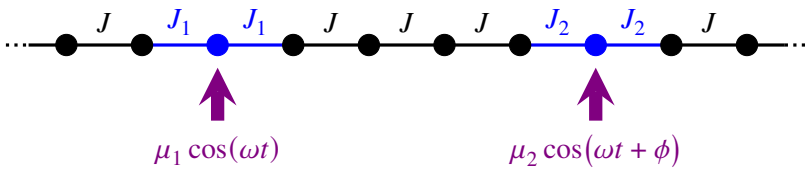

Figure 2.1: Illustration of the model with Hamiltonian (2.3) that is analyzed in this thesis.

CHAPTER 3

Floquet theory

The one-dimensional tight binding system introduced in section 2 is described by the time-periodic Hamiltonian (2.3). For such time-periodic systems, the Floquet formalism provides a method to treat time as a coordinate under time-periodic boundary conditions [9–12]. This often simplifies the calculation of the system's physical properties and their time evolution. In order to apply Floquet analysis to the tight binding chain with two AC driven impurities in section 4, the general concepts of Floquet theory are explained in this section.

3.1 Floquet states

A time periodic Hamiltonian $H(t) = H(t+T)$ possesses stroboscopically stationary states $\psi_\alpha(t)$ called Floquet states [12]. According to the Floquet theorem they solve the time-dependent Schödinger equation

$$i\hbar \mathrm{d}_t \left|\psi(t)\right\rangle = \hat{H}(t) \left|\psi(t)\right\rangle \tag{3.1}$$

and can be written in terms of real quasienergies ϵ_α and time-periodic Floquet modes $\left|u_\alpha(t)\right\rangle = \left|u_\alpha(t+T)\right\rangle$ as [9]

$$\left|\psi_\alpha(t)\right\rangle = e^{-i\varepsilon_\alpha t/\hbar} \left|u_\alpha(t)\right\rangle . \tag{3.2}$$

Thus, one finds that Floquet states are eigenstates of the time evolution operator over one driving period

$$\hat{U}\left(t_0+T, t_0\right) \left|\psi_\alpha\left(t_0\right)\right\rangle = e^{-i\varepsilon_\alpha T/\hbar} \left|\psi_\alpha\left(t_0\right)\right\rangle . \tag{3.3}$$

For any fixed time t, it is possible to choose the Floquet states to form a complete orthonormal basis. According to equation (3.2) the time evolution operator can thus be written as

$$\hat{U}\left(t_2, t_1\right) = \sum_\alpha e^{-i\varepsilon_\alpha\left(t_2-t_1\right)/\hbar} \left|u_\alpha\left(t_2\right)\right\rangle \left\langle u_\alpha\left(t_1\right)\right| . \tag{3.4}$$

Furthermore, any state $|\psi(t)\rangle$ can be expressed in terms of Floquet states and modes as

$$\begin{aligned} |\psi(t)\rangle &= \sum_\alpha c_\alpha e^{i\varepsilon_\alpha t_0/\hbar} |\psi_\alpha(t)\rangle \\ &= \sum_\alpha c_\alpha e^{-i\varepsilon_\alpha (t-t_0)/\hbar} |u_\alpha(t)\rangle \end{aligned} \tag{3.5}$$

with time-independent coefficients $c_\alpha = \langle u_\alpha(t_0)|\psi(t_0)\rangle$. Therefore, if a system is prepared in a Floquet state, its time evolution is governed by the corresponding time-periodic Floquet mode. If the state is a superposition of multiple Floquet states, its time evolution is governed by two contributions. The first one, a time-periodic contribution called micromotion, stems from the Floquet modes that are involved. The second one is a non-periodic contribution that results from the dephasing of phase factors $e^{i\varepsilon_\alpha t_0/\hbar}$. Thus, it is governed by the quasienergies ε_α [12].

3.2 Quasienergy operator and extended Hilbert space

Floquet states $|\psi_\alpha(t)\rangle$ and their eigenvalues $e^{-i\varepsilon_n T/\hbar}$ appearing in equation (3.3) are uniquely defined [12]. One however finds that equation (3.3) does not alter when adding an integer multiple of $\hbar\omega$ to the quasienergy:

$$\varepsilon_\alpha \mapsto \varepsilon_{\alpha n} \equiv \varepsilon_\alpha + n\hbar\omega \quad n \in \mathbb{Z} \qquad \Rightarrow \qquad e^{-i\varepsilon_\alpha T/\hbar} \mapsto e^{-i\varepsilon_\alpha T/\hbar} \underbrace{e^{-in\omega T}}_{1}. \tag{3.6}$$

As the quasienergies are not uniquely defined, neither are the Floquet modes. According to equation (3.2) they can be transformed as

$$|u_\alpha(t)\rangle \mapsto |u_{\alpha n}(t)\rangle \equiv |u_\alpha(t)\rangle e^{in\omega t}. \tag{3.7}$$

From equation (3.2), one can thus write the Floquet states as

$$|\psi_\alpha(t)\rangle = e^{-i\varepsilon_{\alpha n} t/\hbar} |u_{\alpha n}(t)\rangle .$$

Inserting this into the Schrödinger equation (3.1) leads to the Floquet equation

$$\left[\hat{H}(t) - i\hbar \mathrm{d}_t\right] |u_{\alpha n}(t)\rangle = \varepsilon_{\alpha n} |u_{\alpha n}(t)\rangle . \tag{3.8}$$

which is an eigenvalue equation in the extended Floquet Hilbert space

$$\mathcal{F} = \mathcal{H} \otimes \mathcal{L}_T . \tag{3.9}$$

Here, $\mathcal{H}$ is the Hilbert space of a quantum system and $\mathcal{L}_T$ is the space of T-periodically time-dependent functions. According to the notation in reference [12], the element of $\mathcal{F}$ that corresponds to a state $|v(t)\rangle$ in $\mathcal{H}$ is denoted $|v\rangle\!\rangle$ and an operator $\hat{A}$ acting in $\mathcal{H}$ is denoted $\bar{A}$ when it acts in $\mathcal{F}$. The scalar

product in $\mathcal{F}$ is given by the time average of the scalar product in $\mathcal{H}$:

$$\langle\langle u|v\rangle\rangle = \frac{1}{T}\int_0^T \left\langle u(t)\middle|v(t)\right\rangle .$$

The operator on the left hand side of the Floquet equation (3.8) is called quasienergy operator

$$\hat{Q}(t) = \left[\hat{H}(t) - i\hbar \mathrm{d}_t\right].$$

In the extended Hilbert space, the Floquet equation (3.8) can then be written as

$$\bar{Q}|u_{\alpha n}\rangle\rangle = \varepsilon_{\alpha n}|u_{\alpha n}\rangle\rangle. \tag{3.10}$$

A system's Floquet modes and quasienergies can thus be obtained by constructing and diagonalizing the quasienergy operator in the extended Floquet Hilbert space $\mathcal{F}$. The downside of working in a drastically larger Hilbert space comes with the advantage of treating the system in a time-independent fashion by treating time as a coordinate under periodic boundary conditions. In section 4.1, this way of treating the time parameter will be illustrated pictorially when applying Floquet theory to the tight binding chain with two driven impurities.

Note that, even though two solutions $|u_{\alpha n}\rangle\rangle$ and $|u_{\alpha n'}\rangle\rangle$ to equation (3.10) are orthogonal, for $n \neq n'$, they are related by equation (3.7). The same holds for two quasienergies $\varepsilon_{\alpha n}$ and $\varepsilon_{\alpha n'}$ that are related by equation (3.6). The full solution to equation (3.10) thus contains a lot of redundant information and it is sufficient to consider solutions with quasienegies within one interval of width $\hbar\omega$. In analogy to Bloch theory for spatially periodic systems, this interval is called (Floquet) Brillouin zone.

In order to represent the quasienergy operator $\bar{Q}$ as a matrix, a set of basis states $|an\rangle\rangle$ can be constructed from the basis states $|a\rangle$ of $\mathcal{H}$ and the set of time-periodic functions $e^{in\omega t}$ [12]

$$\left|an(t)\right\rangle = e^{in\omega t}\,|a\rangle .$$

In this basis, the matrix elements of the quasienergy operator $\bar{Q}$ are

$$\begin{aligned}\langle\langle a'n'|\bar{Q}|an\rangle\rangle &= \frac{1}{T}\int_0^T \mathrm{d}t e^{-in'\omega t}\langle\langle a'|\hat{H}(t) - i\hbar\mathrm{d}_t|a\rangle\rangle e^{in\omega t} \\ &= \langle\langle a'|\hat{H}_{n'-n}|a\rangle\rangle + \delta_{n'n}\delta_{a'a}n\hbar\omega \end{aligned}\tag{3.11}$$

with the Fourier transformed Hamiltonian

$$\hat{H}_n = \frac{1}{T}\int_0^T \mathrm{d}t e^{-in\omega t}\hat{H}(t) = \hat{H}_{-n}^\dagger \qquad \Leftrightarrow \qquad \hat{H}(t) = \sum_{n=-\infty}^{\infty} e^{in\omega t}\hat{H}_n. \tag{3.12}$$

With respect to the Fourier index n, the quasienergy operator thus features a block structure with block operators

$$\hat{Q}_{n'n} = \hat{H}_{n'-n} + \delta_{n'n}n\hbar\omega. \tag{3.13}$$

3.3 Floquet Hamiltonian and micromotion operator

After having learned how to express any state in a time-periodic system in terms of Floquet modes and quasienergies, and how to obtain these by means of the quasienergy operator, it is time to introduce the so-called Floquet Hamiltonian $\hat{H}^F_{t_0}$. This Floquet Hamiltonian is time-independent and generates the time evolution over a full period after the initial time t_0 [12]

$$\exp\left(-\frac{i}{\hbar}T\hat{H}^F_{t_0}\right) \equiv \hat{U}\left(t_0+T,t_0\right). \tag{3.14}$$

It is thus useful to study the system's evolution over time spans that are long compared to a single driving period. Using the expression (3.4) for the time evolution operator in terms of Floquet modes, one can show that the Floquet Hamiltonian can be expressed as

$$\hat{H}^F_{t_0} = \sum_\alpha \varepsilon_\alpha \left|u_\alpha\left(t_0\right)\right\rangle\left\langle u_\alpha\left(t_0\right)\right|. \tag{3.15}$$

Time evolution in between full periods, that is not contained in the Floquet Hamiltonian, is described by the so-called micromotion operator:

$$\hat{U}_F(t_2,t_1) \equiv \sum_\alpha \left|u_\alpha\left(t_2\right)\right\rangle\left\langle u_\alpha\left(t_1\right)\right|.$$

3.4 Obtaining the Floquet Hamiltonian from the quasienergy operator

In section 3.2 the quasienergy operator was introduced as the Hamiltonian-like operator of Floquet theory. It governs its central eigenvalue equation (3.10) called Floquet equation. With this, the quasienergy operator is necessary to obtain a system's Floquet modes and quasienergies. In this section, it is shown that the quasienergy can in fact also be used to obtain the Floquet Hamiltonian introduced in section 3.3.

For this consider a unitary transformation $\hat{U}_F$ which block diagonalizes the quasienergy operator whith respect to the Fourier index n. Transforming equation (3.11) with this operator yields [12]

$$\langle\langle a'n'|\bar{U}_F^\dagger \bar{Q}\bar{U}_F|an\rangle\rangle = \delta_{n'n}\left(\left\langle a'\middle|\hat{H}_F\middle|a\right\rangle + \delta_{a'a}n\hbar\omega\right) \tag{3.16}$$

with the gauge-transformed and time-independent Hamiltonian

$$\hat{H}_F = \hat{U}_F^\dagger(t)\hat{H}(t)\hat{U}_F(t) - i\hbar\hat{U}_F^\dagger(t)\mathrm{d}_t\hat{U}_F(t) \tag{3.17}$$

which will later be called effective Hamiltonian. The central block ($n = n' = 0$) of the block-diagonal quasienergy operator thus has matrix elements

$$\langle\langle a'0|\bar{U}_F^\dagger \bar{Q}\bar{U}_F|a0\rangle\rangle = \left\langle a'\middle|\hat{H}_F\middle|a\right\rangle. \tag{3.18}$$

In a next step, the quasienergy operator can be rewritten by multiplying $\langle\langle u_{\alpha n}|$ from the right to the

Floquet equation (3.10) and summing over α and n:

$$\bar{Q}\underbrace{\sum_{\alpha}\sum_{n=-\infty}^{\infty}|u_{\alpha n}\rangle\!\rangle\langle\!\langle u_{\alpha n}|}_{\mathbb{I}} = \sum_{\alpha}\sum_{n=-\infty}^{\infty}\varepsilon_{\alpha n}|u_{\alpha n}\rangle\!\rangle\langle\!\langle u_{\alpha n}|$$

$$\Rightarrow \qquad \bar{Q} = \sum_{\alpha}\sum_{n=-\infty}^{\infty}|u_{\alpha n}\rangle\!\rangle(\varepsilon_{\alpha}+n\hbar\omega)\langle\!\langle u_{\alpha n}|$$

where the completeness of the Floquet modes was used and the quasienergy $\varepsilon_{\alpha n}$ was rewritten using equation (3.6). Using equation (3.7), the central block of this representation is written as

$$\bar{Q}_{n=0} = \sum_{\alpha}\left|u_{\alpha}(t)\right\rangle\varepsilon_{\alpha}\left\langle u_{\alpha}(t)\right|. \tag{3.19}$$

Having rewritten the quasienergy operator in these ways, let us return to the task of this section which is determining its relation to the Floquet Hamiltonian. For this, consider the representation (3.15) of the quasienergy operator and insert two complete sets of eigenstates in $\mathcal{H}$:

$$\begin{aligned}
H^F_{t_0} &= \sum_{\alpha}\varepsilon_{\alpha}\left|u_{\alpha}(t_0)\right\rangle\left\langle u_{\alpha}(t_0)\right| \\
&= \sum_{\alpha}\sum_{a'a}\varepsilon_{\alpha}\left|a'0(t_0)\right\rangle\left\langle a'0(t_0)|u_{\alpha}(t_0)\right\rangle\left\langle u_{\alpha}(t_0)|a0(t_0)\right\rangle\left\langle a0(t_0)\right| \\
&\overset{((3.19))}{=} \sum_{a'a}\left|a'0(t_0)\right\rangle\left\langle a'0(t_0)\right|\underbrace{\left[\sum_{\alpha}\left|u_{\alpha}(t_0)\right\rangle\varepsilon_{\alpha}\left\langle u_{\alpha}(t_0)\right|\right]}_{\bar{Q}_{n=0}}\left|a0(t_0)\right\rangle\left\langle a0(t_0)\right| \\
&= \sum_{a'a}\left|a'0(t_0)\right\rangle\langle\!\langle a'0|\bar{Q}|a0\rangle\!\rangle\left\langle a0(t_0)\right| \\
&= \sum_{a'a}\left|a'0(t_0)\right\rangle\hat{U}_F\hat{U}_F^{\dagger}\langle\!\langle a'0|\bar{Q}|a0\rangle\!\rangle\hat{U}_F\hat{U}_F^{\dagger}\left\langle a0(t_0)\right| \\
&\overset{((3.18))}{=} \sum_{a'a}\hat{U}_F\left|a'0(t_0)\right\rangle\underbrace{\langle\!\langle a'0|\bar{U}_F^{\dagger}\bar{Q}\bar{U}_F^{\dagger}|a0\rangle\!\rangle}_{\langle a'|\hat{H}_F|a\rangle}\left\langle a0(t_0)\right|\hat{U}_F^{\dagger} \\
&= \left[\sum_{a'}\hat{U}_F\left|a'0(t_0)\right\rangle\left\langle a'\right|\right]\hat{H}_F\left[\sum_{a}\left|a0(t_0)\right\rangle\left\langle a\right|\hat{U}_F^{\dagger}\right] \\
&= \hat{U}_F(t_0)\hat{H}_F\hat{U}_F^{\dagger}(t_0).
\end{aligned} \tag{3.20}$$

Thus, one finds that the Floquet Hamiltonian $H^F_{t_0}$ can be obtained from the effective Hamiltonian H_F by means of the unitary gauge transformation $\hat{U}_F^{\dagger}$. The challenge lies in finding this transformation which block diagonalizes $\bar{Q}$ and equivalently turns the original Hamiltonian $\hat{H}(t)$ time-independent. In many cases, only approximate transformations and thus Floquet Hamiltonians can be found. One such example for the given model of a driven tight binding chain will be the high frequency effective

Hamiltonian which will be derived in section 5.1.1.

With the tools of Floquet theory for time-periodic systems at hand, it is time to return to the tight binding system with two AC driven impurities introduced in section 2. In the next section, Floquet theory is used to analyze transport properties and time evolution of this model.

CHAPTER 4

Floquet analysis of the model

In section 2, the model of a tight binding chain with two periodically driven impurities was introduced. Next, in section 3, the concepts of Floquet theory were introduced. This theory treats the time-dependence of such a time periodic Hamiltonian as a coordinate and thus in many cases facilitates the calculation of the system's properties. In this section, the tools of Floquet theory will be applied to the driven tight binding chain to determine its time evolution and transport characteristics.

4.1 Quasienergy operator

Section 3.2 introduced the quasienergy operator which can be seen as the Floquet equivalent of the Hamilton operator. It was shown how to obtain the Floquet modes and quasienergies by diagonalizing this operator. Section 3.4 explains how to determine the Floquet Hamiltonian by block diagonalizing the quasienergy operator.

Finding the driven tight binding chain's quasienergy operator is therefore a sensible first step of its Floquet analysis. Equation (3.13) tells us that the blocks of the quasienery operator with respect to the Fourier index n can be found from the Fourier modes of the time periodic Hamiltonian $\hat{H}_n$ introduced in equation (3.12). These Fourier modes can easily be obtained from the model's Hamiltonian (2.3).

The frequency-independent zeroth Fourier mode is simply the Hamiltonian of the undriven tight binding chain (2.1):

$$\hat{H}_0 = \hat{H}_{\text{tb}} \tag{4.1}$$

The frequency-dependent Fourier modes with $n \neq 0$ are obtained by rewriting the Hamiltonian (2.2)

describing the external drive:

$$\begin{aligned}\hat{H}_{\text{drive}}(t) &= -\mu_1 \cos(\omega t)\hat{c}_0^\dagger \hat{c}_0 - \mu_2 \cos(\omega t + \phi)\hat{c}_l^\dagger \hat{c}_l \\ &= -\frac{\mu_1}{2}\left(e^{i\omega t} + e^{-i\omega t}\right)\hat{c}_0^+ \hat{c}_0 - \frac{\mu_2}{2}\left(e^{i\omega t + i\phi} + e^{-i\omega t - i\phi}\right)\hat{c}_l \hat{c}_l \\ &= e^{-i\omega t}\underbrace{\left(-\frac{\mu_1}{2}\hat{c}_0\hat{c}_0 - \frac{\mu_2}{2}e^{-i\phi}\hat{c}_l\hat{c}_l\right)}_{\hat{H}_{-1}} + e^{i\omega t}\underbrace{\left(-\frac{\mu_1}{2}\hat{c}_0 + \hat{c}_0 - \frac{\mu_2}{2}e^{i\phi}\hat{c}_l\hat{c}_l\right)}_{\hat{H}_1} \\ &= e^{-i\omega t}\hat{H}_{-1} + e^{i\omega t}\hat{H}_1.\end{aligned} \tag{4.2}$$

The system's quasienergy operator is then constructed using equation (3.13) and the Floquet equation (3.10) reads

$$\begin{pmatrix} \ddots & & & & & & & \\ \hat{H}_{-1} & \hat{H}_0 - 2\hbar\omega\mathbb{I} & \hat{H}_1 & & & & & \\ & \hat{H}_{-1} & \hat{H}_0 - \hbar\omega\mathbb{I} & \hat{H}_1 & & & & \\ & & \hat{H}_{-1} & \hat{H}_0 & \hat{H}_1 & & & \\ & & & \hat{H}_{-1} & \hat{H}_0 + \hbar\omega\mathbb{I} & \hat{H}_1 & & \\ & & & & \hat{H}_{-1} & \hat{H}_0 + 2\hbar\omega\mathbb{I} & \hat{H}_1 & \\ & & & & & & \ddots & \end{pmatrix} \begin{pmatrix} \vdots \\ u_{\alpha,-2} \\ u_{\alpha,-1} \\ u_{\alpha,0} \\ u_{\alpha,1} \\ u_{\alpha,2} \\ \vdots \end{pmatrix} = \varepsilon_\alpha \begin{pmatrix} \vdots \\ u_{\alpha,-2} \\ u_{\alpha,-1} \\ u_{\alpha,0} \\ u_{\alpha,1} \\ u_{\alpha,2} \\ \vdots \end{pmatrix}. \tag{4.3}$$

This way of representing the Floquet equation for the system at hand nicely illustrates the abstract concept of the extended Floquet Hilbert space $\mathcal{F}$ introduced in section 3.2. Each block of $\bar{Q}$ acts on a physical state of the quantum mechanical system in $\mathcal{H}$. The time periodicity of $\hat{H}(t)$ is the reason why it can be represented in terms of multiple Fourier modes. They lead to the coupling of multiple $\mathcal{H}$-operators and extend the original Hilbert space to the Floquet Hilbert space $\mathcal{F} = \mathcal{H} \otimes \mathcal{L}_T$.

This quasienergy operator is equivalent to the Hamiltonian of multiple tight binding chains that due to the off-diagonal block matrices $\hat{H}_{\pm 1}$ couple to each other at the impurity sites 0 and l (figure 4.1). According to equation (4.2), the coupling constant at impurity i is given by $\mu_i/2$. This picture illustrates how time-periodicity enables Floquet theory to treat time as a coordinate. In this way, it is possible to apply concepts and intuition from analogous time-independent systems. In sections 6.2 and 6.3, we will discuss how this picture helps in understanding the system's transport properties.

To determine the time evolution of a physical system, there are two ways to proceed from here: First, as discussed in section 3.4, $\bar{Q}$ can be block diagonalized by means of a unitary transformation $\hat{U}_F$ (equation (3.16)). According to equation (3.17), the so-called effective Hamiltonian can be obtained from $\hat{U}_F$. It was shown that the effective Hamiltonian is equivalent to the Floquet Hamiltonian which governs the time evolution on long time scales. An approximation to this effective Hamiltonian is calculated in the limit of large driving frequencies in section 5.1.1.

Secondly, according to equation (3.5), the system's wavefunction at any time t can be constructed from the quasienergies $\varepsilon_{\alpha n} = \varepsilon_\alpha + n\hbar\omega$ and Floquet modes $|u_{\alpha n}\rangle$. These can be obtained by diagonalizing the quasienergy operator $\bar{Q}$ of the left-hand side of the Floquet equation (4.3). The results of this procedure are discussed in appendix A. Here, by considering an incoming wave packet

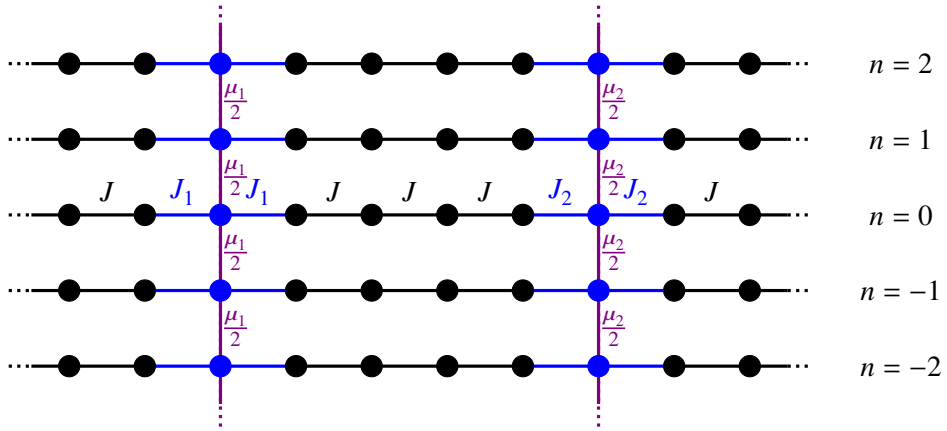

Figure 4.1: The quasienergy operator of equation (4.3) is equivalent to a Hamiltonian describing multiple tight binding chains labeled by a Fourier index n with impurities at two sites at a distance $l = 5$. At these impurities the chains are coupled to each other.

impinging on the two impurities, the chain's transport properties can be analyzed for various system and driving parameters. This however, comes with the cost of diagonalizing the large quasienergy operator and with a limited momentum resolution. Since we are rather interested in transport characteristics than in the system's time evolution, a more sophisticated approach to calculate particle transmission is presented in the next section.

4.2 Particle transport

In the previous section, the quasienergy operator of a system with two AC driven impurities was calculated and interpreted to describe a set of coupled tight binding chains. In this section, we will use this interpretation to derive the system's transport properties in a more elegant way inspired by reference [26].

The goal of this derivation is considering an incoming wave from the left with energy ε to find a steady state solution to the Floquet equation (4.3). Since we are interested in the solution for a specific energy, the index α can be dropped in the following calculations. Let us first find a general solution to the Floquet equation before making an ansatz for the wavefunction. For this, we express the Floquet mode with Fourier index n in terms of single site amplitudes $\phi_{j,n}$,

$$\left|u_n\right\rangle = \sum_j \phi_{j,n} \hat{c}_j^\dagger \left|0\right\rangle , \tag{4.4}$$

where $|0\rangle$ is the vacuum state denoting an empty tight binding chain. Inserting this into the Floquet equation (4.3), one finds

$$H_0 \sum_j \phi_{j,n} \hat{c}_j^\dagger \left|0\right\rangle + H_1 \sum_j \phi_{j,n+1} \hat{c}_j^\dagger \left|0\right\rangle + H_{-1} \sum_j \phi_{j,n-1} \hat{c}_j^\dagger \left|0\right\rangle = (\varepsilon + n\hbar\omega) \sum_j \phi_{j,n} \hat{c}_j^\dagger \left|0\right\rangle \tag{4.5}$$

with the Fourier components of the original Hamiltonian from equations (4.1) and (4.2).

In equation (4.5), the following combinations of creation an annihilation operators appear:

$$(\hat{c}_i^\dagger \hat{c}_{i+1} + \hat{c}_{i+1}^\dagger \hat{c}_i)\hat{c}_j^\dagger \quad , \qquad \hat{c}_0^\dagger \hat{c}_0 \hat{c}_j^\dagger \qquad \text{and} \qquad \hat{c}_l^\dagger \hat{c}_l \hat{c}_j^\dagger .$$

The the first term stems from the Hamiltonian H_0 where the site index j has been renamed to i.

Using either the bosonic or fermionic commutation relations and the fact that $\hat{c}_j |0\rangle = 0$, equation (4.5) can be simplified with the following calculations:

$$\begin{aligned}\sum_j \phi_{j,n} \left(\hat{c}_i^\dagger \hat{c}_{i+1} + \hat{c}_{i+1}^\dagger \hat{c}_i\right) \hat{c}_j^\dagger |0\rangle &= \sum_j \phi_{j,n} \left(\hat{c}_i^\dagger \delta_{i+1,j} + \hat{c}_{i+1}^\dagger \delta_{i,j}\right) |0\rangle \\ &= \left(\phi_{i+1,n} \hat{c}_i^\dagger + \phi_{i,n} \hat{c}_{i+1}^\dagger\right) |0\rangle \end{aligned} \tag{4.6}$$

and

$$\begin{aligned}\sum_j \phi_{j,n+1} \hat{c}_i^\dagger \hat{c}_i \hat{c}_j^\dagger |0\rangle &= \sum_j \phi_{j,n+1} \hat{c}_i^\dagger \delta_{i,j} |0\rangle \\ &= \phi_{i,n+1} \hat{c}_i^\dagger |0\rangle .\end{aligned}$$

Inserting these relations into equation (4.5), shifting indices and collecting all terms that act on the same site of the tight binding chain, yields the following recurrence relations for the single site wavefunctions:

$$-J_1 \left(\phi_{1,n} + \phi_{-1,n}\right) - \frac{\mu_1}{2} \left(\phi_{0,n+1} + \phi_{0,n-1}\right) = (\varepsilon + n\hbar\omega)\phi_{0,n} \qquad j = 0 \tag{4.7}$$

$$-J\phi_{\pm 2,n} - J_1 \phi_{0,n} = (\varepsilon + n\hbar\omega)\phi_{\pm 1,n} \qquad j = \pm 1 \tag{4.8}$$

$$-J_2 \left(\phi_{l+1,n} + \phi_{l-1,n}\right) - \frac{\mu_2}{2} \left(\phi_{l,n+1} e^{i\phi} + \phi_{l,n-1} e^{-i\phi}\right) = (\varepsilon + n\hbar\omega)\phi_{l,n} \qquad j = l \tag{4.9}$$

$$-J\phi_{l\pm 2,n} - J_2 \phi_{l,n} = (\varepsilon + n\hbar\omega)\phi_{l\pm 1,n} \qquad j = l \pm 1 \tag{4.10}$$

$$-J\phi_{j+1,n} - J\phi_{j-1,n} = (\varepsilon + n\hbar\omega)\phi_{j,n} \qquad \text{else} \tag{4.11}$$

In order to solve this set of coupled recurrence relations, let us first rescale all parameters in terms of the system's internal energy scale J:

$$J_i' \equiv \frac{J_i}{J} \qquad \mu_i' \equiv \frac{\mu_i}{J} \qquad \varepsilon' \equiv \frac{\varepsilon}{J} \qquad \omega' \equiv \frac{\hbar\omega}{J}. \tag{4.12}$$

To determine the tight binding chain's transport properties, we now consider an incoming plane wave from the left $\exp(ik_0 j)$ in Floquet channel $n = 0$ with amplitude 1. At the first impurity on site $j = 0$, this incoming wave is partly reflected to multiple chains with respective amplitudes r_n or transmitted with amplitudes t_n'. On the second impurity, this transmitted wave is again either reflected with amplitudes r_n' or transmitted with amplitudes t_n. The general ansatz (4.4) therefore becomes

$$\begin{aligned}|u_n\rangle = &\sum_{j<0} \left(\delta_{n,0} e^{ik_0 j} + r_n e^{-ik_n j}\right) \hat{c}_j^\dagger |0\rangle + \phi_{0,n} \hat{c}_0^\dagger |0\rangle + \sum_{0<j<l} \left(t_n' e^{ik_n j} + r_n' e^{-ik_n j}\right) \hat{c}_j^\dagger |0\rangle \\ &+ \phi_{l,n} \hat{c}_l^\dagger |0\rangle + \sum_{j>l} t_n e^{ik_n j} \hat{c}_j^\dagger |0\rangle \end{aligned} \tag{4.13}$$

Before determining the single site amplitudes $\phi_{j,n}$, let us relate the momenta k_n to the incoming wave's energy ε. Inserting the ansatz (4.13) into the bulk recurrence relation (4.11) leads to the dispersion relation

$$\varepsilon' + n\omega' = -2\cos(k_n). \tag{4.14}$$

For the central chain $n = 0$, this yields the dispersion relation of a homogeneous tight binding chain $\varepsilon' = -2\cos(k_0)$ with $|\varepsilon'| < 2$. Since the corresponding wavefunction solution is delocalized over the entire chain, it is referred to as an unbound channel [26]. The same holds for any chain with $|\varepsilon' + n\omega'| < 2$.

For chains with $|\varepsilon' + n\omega'| > 2$ however, the dispersion relation (4.14) leads to a complex momentum $k_n = i\kappa_n$ for negative energy and $k_n = i\kappa_n + \pi$ for positive energy. The dispersion relation then becomes

$$\varepsilon' + n\omega' = \mp 2\arccos(k_n) \tag{4.15}$$

where the negative sign refers to negative energies.

From here on we can work our way through the recurrence relations (4.7) to (4.10). One can start with equations (4.8) and (4.10) which contain only terms with the same Fourier index n and therefore describe single chains processes without coupling between chains. Inserting (4.13) into relation (4.8) yields

$$E_n = \left(\delta_{n,0} + r_n\right) = \left(t'_n + r'_n\right) \qquad \text{with} \qquad E_n \equiv J'_1\phi_{0,n}. \tag{4.16}$$

Similarly, equation (4.10) gives

$$\begin{aligned} & J'_2 e^{-ik_n l}\phi_{l,n} = t_n = t'_n + r'_n e^{-i2k_n l} \\ \Rightarrow \quad & t_n = E_n - 2ir'_n e^{-ik_n l}\sin\left(k_n l\right). \end{aligned} \tag{4.17}$$

In this way, all coefficients can be expressed in terms of E_n and r'_n.

Now, we can turn towards the recurrence relations (4.7) and (4.9). They describe couplings between different chains and therefore contain the system's time dependence. Inserting these coefficients and the ansatz (4.13) into equation (4.7) gives r'_n in terms of E_n:

$$ir'_n = \frac{1}{\sin\left(k_n\right)}\left\{E_n\left[e^{ik_n} - \frac{1}{\left(J'_1\right)^2}\cos\left(k_n\right)\right] + \frac{\mu'_1}{4}\frac{1}{\left(J'_1\right)^2}\left[E_{n+1} + E_{n-1}\right] - i\delta_{n,0}\sin\left(k_0\right)\right\} \tag{4.18}$$

Finally, inserting relations (4.16) to (4.18) into equation (4.10) gives a recurrence relation for E_n:

$$\beta_n = \sum_{k=-2}^{2}\alpha_k^{(n)}E_{n+k} \tag{4.19}$$

with

$$
\begin{aligned}
\beta_0 =& -2i \sin\left(k_0\right) \sin\left(k_{-1}\right) \sin\left(k_1\right) \left[-\sin\left(k_0(l-1)\right) - e^{ik_0} \sin\left(k_0 l\right) + 2\frac{1}{\left(J_2'\right)^2} \cos\left(k_0\right) \sin\left(k_0 l\right) \right] \\
\beta_{\pm_1} =& 2i \frac{\mu_2'}{2\left(J_2'\right)^2} e^{\mp i\phi} \sin\left(k_0\right) \sin\left(k_{\pm 1}\right) \sin\left(k_{\pm 2}\right) \sin\left(k_0 l\right) \\
\beta_n =& 0 \quad \text{else} \\
\alpha_0^{(n)} =& 2 \sin\left(k_{n+1}\right) \sin\left(k_{n-1}\right) \Big[-e^{ik_n l} \cos\left(k_n\right) \sin\left(k_n\right) + e^{ik_n} \left(\sin\left(k_n(l-1)\right) + e^{ik_n} \sin\left(k_n l\right) \right) \\
& \qquad - \frac{1}{\left(J_1'\right)^2} \cos\left(k_n\right) \left(\sin\left(k_n(l-1)\right) + e^{ik_n} \sin\left(k_n l\right) \right) \\
& \qquad + \frac{1}{\left(J_2'\right)^2} \cos\left(k_n\right) \left(e^{ik_n l} \sin\left(k_n\right) - 2e^{ik_n} \sin\left(k_n l\right) \right) \Big] \\
& + 4 \sin\left(k_{n+1}\right) \sin\left(k_{n-1}\right) \frac{1}{\left(J_1'\right)^2} \frac{1}{\left(J_2'\right)^2} \cos^2\left(k_n\right) \sin\left(k_n l\right) \\
& + \frac{\mu_1'}{2\left(J_1'\right)^2} \frac{\mu_2'}{2\left(J_2'\right)^2} \sin\left(k_n\right) \left[e^{-i\phi} \sin\left(k_{n+1}\right) \sin\left(k_{n-1} l\right) + e^{i\phi} \sin\left(k_{n-1}\right) \sin\left(k_{n+1} l\right) \right] \\
\alpha_{\pm 1}^{(n)} =& \sin\left(k_{n\mp 1}\right) \Big[\frac{\mu_1'}{2\left(J_1'\right)^2} \sin\left(k_{n\pm 1}\right) \left(\sin\left(k_n(l-1)\right) + e^{ik_n} \sin\left(k_n l\right) \right) \\
& \qquad + \frac{\mu_2'}{2\left(J_2'\right)^2} e^{\pm i\phi} \sin\left(k_n\right) \left(-\sin\left(k_{n\pm_1}\right) e^{ik_{n\pm 1} l} + 2\sin\left(k_{n\pm 1} l\right) e^{ik_{n\pm 1}} \right) \Big] \\
& - 2 \sin\left(k_{n\mp 1}\right) \Big[\frac{\mu_1'}{2\left(J_1'\right)^2} \frac{1}{\left(J_2'\right)^2} \sin\left(k_{n\pm 1}\right) \cos\left(k_n\right) \sin\left(k_n l\right) \\
& \qquad + \frac{\mu_2'}{2\left(J_2'\right)^2} \frac{1}{\left(J_1'\right)^2} e^{\pm i\phi} \sin\left(k_n\right) \cos\left(k_{n\pm 1}\right) \sin\left(k_{n\pm 1} l\right) \Big] \\
\alpha_{\pm 2}^{(n)} =& \frac{\mu_1'}{2\left(J_1'\right)^2} \frac{\mu_2'}{2\left(J_2'\right)^2} e^{\pm i\phi} \sin\left(k_n\right) \sin\left(k_{n\mp 1}\right) \sin\left(k_{n\pm 1} l\right)
\end{aligned}
\tag{4.20}
$$

Equation (4.19) can equally be written as

$$
\underbrace{\begin{pmatrix}
 & \ddots & & & & & \\
\alpha_{-2}^{(-1)} & \alpha_{-1}^{(-1)} & \alpha_{0}^{(-1)} & \alpha_{1}^{(-1)} & \alpha_{2}^{(-1)} & & \\
 & \alpha_{-2}^{(0)} & \alpha_{-1}^{(0)} & \alpha_{0}^{(0)} & \alpha_{1}^{(0)} & \alpha_{2}^{(0)} & \\
 & & \alpha_{-2}^{(1)} & \alpha_{-1}^{(1)} & \alpha_{0}^{(1)} & \alpha_{1}^{(1)} & \alpha_{2}^{(1)} \\
 & & & & & \ddots &
\end{pmatrix}}_{A}
\underbrace{\begin{pmatrix} \vdots \\ E_{-1} \\ E_0 \\ E_1 \\ \vdots \end{pmatrix}}_{\vec{E}}
=
\underbrace{\begin{pmatrix} \vdots \\ \beta_{-1} \\ \beta_0 \\ \beta_1 \\ \vdots \end{pmatrix}}_{\vec{\beta}}
$$

with the infinite-dimensional matrix A and vectors $\vec{E}$ and $\vec{\beta}$. Note that only the coefficients β_i with

$i \in \{1, 0, 1\}$ do not vanish.

The wavefunction amplitudes can now be determined by cutting A, $\vec{E}$ and $\vec{\beta}$ at some cutoff indices $\pm n_{\max}$ and then inverting A numerically. The coefficients E_n are then calculated as

$$\vec{E} = A^{-1}\vec{\beta}. \tag{4.21}$$

Using equations (4.16) to (4.18), the other scattering amplitudes from the ansatz (4.13) are then calculated one after the other to obtain the full wavefunction on all tight binding chains.

Having found a scattering solution to the Floquet equation, it remains open to determine its transport properties. The transmission probability is defined as the ratio of transmitted and incoming current. To calculate transmission, one can therefore consider the two site current operator defined by [26]

$$\hat{j}_m \equiv -iJ\left(c_m^\dagger c_{m+1} - c_{m+1}^\dagger c_m\right). \tag{4.22}$$

The total current on the left hand side of the impurities is then given by

$$J_- = \sum_{m<0} \left\langle \phi_- \middle| \hat{j}_m \middle| \phi_- \right\rangle = \underbrace{-2JN_- \sin\left(k_0\right)}_{\text{incoming}} + \underbrace{2JN_- \sum_n \left|r_n\right|^2 \sin\left(k_n\right)}_{\text{reflected}} \tag{4.23}$$

where the incoming and the reflected currents have been identified. Equally, the total current and on the right hand side of the impurity reads

$$J_+ = \sum_{m>l} \left\langle \phi_+ \middle| \hat{j}_m \middle| \phi_+ \right\rangle = -2JN_+ \sum_n \left|t_n\right|^2 \sin\left(k_n\right). \tag{4.24}$$

Here, the numbers of sites left and right of the impurities $N_- = \sum_{j<0} 1$ and $N_+ = \sum_{j>l} 1$ have been introduced which are infinite in the general model but will cancel out later. Furthermore, shorthand notations for the extended wavefunctions at each side of the impurities have been introduced:

$$\begin{aligned}
\left|\phi_-\right\rangle &= \sum_{j<0}\sum_n \phi_{j,n} c_j^+ \left|0\right\rangle = \sum_{j<0}\sum_n \left(e^{ik_0 j} + v_n e^{-ik_n J}\right) c_j^+ \left|0\right\rangle \\
\left|\phi_+\right\rangle &= \sum_{j>l}\sum_n \phi_{j,n} c_j^+ \left|0\right\rangle = \sum_{j>l}\sum_n t_n e^{ik_{nj}} c_j^+ \left|0\right\rangle
\end{aligned}$$

where the sums over n only run over unbound channels with $|\varepsilon + n\omega| < 2J$. As explained above in this section, only the wavefunctions on those channels extend over the entire chain and therefore influence its transport properties. Therefore, according to equation (4.19), only components of the matrix A and vectors $\vec{E}$ and $\vec{\beta}$ with indices

$$n \leq \left| \left\lfloor \frac{2J + |\varepsilon|}{\omega} \right\rfloor + 2 \right|$$

are required to calculate the transmission. It becomes clear that for small driving frequencies ω/J, the number of unbound channels and therefore the computational cost is large. The cutoff index $n_{\max}$ however needs to be chosen higher for the numerical inversion of A to yield acceptable results.

Next, all currents are normalized such that the incoming current from equation (4.23) is 1 and the transmission probability is finally computed as the ratio of transmitted and incoming current:

$$\begin{aligned} J_{\text{in}} &= \frac{1}{v}\left(-2JN_{-}\sin\left(k_0\right)\right) \stackrel{!}{=} 1 \qquad \Rightarrow \qquad v = -2JN_{-}\sin\left(k_0\right) \\ T &= \frac{\frac{1}{v}J_{+}}{J_{\text{in}}} = \sum_n \left|t_n\right|^2 \frac{\sin\left(k_n\right)}{\sin\left(k_0\right)}. \end{aligned} \tag{4.25}$$

Here $N_{-} = N_{+}$ was used which is satisfied for an infinite chain and also holds for a finite chain when the impurities sit in their center. We have arrived at an expression for the transmission probability stating that the total transmission probability is obtained by the summing over transmission probabilities of all propagating channels, weighted by the particle velocities in the respective channels.

The computation of transmission can be further simplified by imposing current conservation $J_{+} = J_{-}$ [26]. Equating equation (4.23) with equation (4.24) and eliminating r'_n by means of equation (4.16) gives the transmission probabiliy

$$T = 2\,\text{Re}\left(E_0\right) - \sum_n \left|E_n\right|^2 \frac{\sin\left(k_n\right)}{\sin\left(k_0\right)}. \tag{4.26}$$

Compared to equation (4.25), this expression has the advantage that only the coefficients E_n need to be computed using relation (4.21) to determine the transport probability. Due to current conservation, the reflection probability is then simply given by $R = 1 - T$.

With this derivation, we are now able to determine transport through a tight binding chain with two AC driven impurities. Regarding, that this is a time-dependent model with a large set of tunable parameters it is quite impressive to have arrived at a compact expression to determine transport properties for any set of system parameters. Before discussing the results of this general derivation in chapter 6, we will consider the special case of large driving frequencies in the following chapter 5 in order to gain a first insight into the system's transport characteristics.

CHAPTER 5

High frequency limit

In the previous sections 2 and 4, the model of a tight binding chain with two AC driven impurities was introduced and a general method to calculate its transport properties and the wavefunction's time evolution using the Floquet formalism (section 3) were presented. Transmission through the two impurities can now be determined for any given set of system and drive parameters. However, so far, all equations yield numerical results that cannot be calculated in a closed form and are thus hard to interpret.

In order to gain physical understanding of the system's transport properties, in this chapter, the high frequency limit $\hbar\omega \gg J$ is considered where the time scale of the external drive ω^{-1} is much shorter than the system's internal time scale $\hbar J^{-1}$. In this regime, one expects the driving oscillations to average out and to obtain an effective time-independent model. After deriving this effective model in section 5.1, a continuous analogue system is constructed in section 5.2 to understand characteristic features of transport. After relating the discrete and the continuous model to each other in section 5.2.3, the transport features will be explained in section 5.3 by taking into account the system's wavefunctions and by identifying confined modes and bound states. The chapter will be closed by analyzing how the transport properties changes in systems with asymmetric impurities in section 5.4.

5.1 Discrete high frequency effective model

In this section, we will learn that a Floquet system where the energy scale of the external driving frequency exceeds the system's internal energy scale can be described by an effective time-independent model. In the first subsection 5.1.1, this result will be applied to the tight binding chain with driven impurities (section 2) which was analyzed by means of Floquet theory (sections 3 and 4). In the following subsection 5.1.2, transmission through this high frequency effective model will be computed.

5.1.1 Derivation of the high frequency effective model

As explained in section 3.4, the unitary gauge transformation $\hat{U}_F$ that block diagonalizes the quasienergy operator is equivalent to the transformation that transforms the Hamiltonian $H(t)$ to an effective, time-independent Hamiltonian $\hat{H}_F$ that is equivalent to the Floquet Hamiltonian introduced in section 3.3. The goal of this section is to find this effective Hamiltonian in the limit of large driving frequencies compared to the internal energy scale given by the hopping amplitude: $\omega \gg J$. For this, first, relate the effective Hamiltonian to the Fourier components of the Hamiltonian. Then, transform the original Hamiltonian such that a meaningful high frequency limit can be determined.

Following reference [28], first, consider the time evolution operator of a system with T-periodically time-dependent Hamiltonian $\hat{H}(\tau)$ with the dimensionless time $\tau = \omega t$:

$$U(t) = \exp\left(-\frac{i}{\hbar}\int_0^t \mathrm{d}t'\,\hat{H}\left(\omega t'\right)\right) \qquad \Rightarrow \qquad \hat{U}(\tau) = \exp\left(-\frac{i}{\hbar\omega}\int_0^\tau \mathrm{d}\tau'\,\hat{H}\left(\tau'\right)\right)$$

In the high frequency limit, this time evolution operator can be expanded in terms of $1/\omega$ to find

$$\begin{aligned} \hat{U}(\tau) &= 1 - \frac{i}{\hbar\omega}\int_0^\tau \mathrm{d}\tau'\,\hat{H}\left(\tau'\right) + O\left(\frac{1}{\omega}\right)^2 \\ \Rightarrow \quad \hat{U}(2\pi) &= 1 - \frac{i}{\hbar\omega}\int_0^{2\pi} \mathrm{d}\tau'\,\hat{H}\left(\tau'\right) + O\left(\frac{1}{\omega}\right)^2 \end{aligned} \tag{5.1}$$

Now, Fourier expand the Hamiltonian to find

$$\Rightarrow \quad \int_0^{2\pi} \mathrm{d}\tau'\,\hat{H}\left(\tau'\right) = \int_0^{2\pi} \mathrm{d}\tau' \sum_n \hat{H}_n e^{in\tau'} = \sum_n \hat{H}_n \underbrace{\int_0^{2\pi} \mathrm{d}\tau'\, e^{in\tau'}}_{2\pi\delta_n} = 2\pi\hat{H}_0$$

$$\Rightarrow \quad \hat{U}(2\pi) = 1 - i\frac{2\pi}{\hbar\omega}\hat{H}_0 + O\left(\frac{1}{\omega}\right)^2 \tag{5.2}$$

According to the definition (3.14), the time evolution after a full period $\tau = 2\pi$ is governed by the Floquet Hamiltonian:

$$\hat{U}(2\pi) = \exp\left(-\frac{i}{\hbar}\frac{2\pi}{\omega}\hat{H}_F\right) = 1 - i\frac{2\pi}{\hbar\omega}\hat{H}_F + O\left(\frac{1}{\omega}\right)^2. \tag{5.3}$$

By comparing equations (5.2) and (5.3), one obtains the first order high frequency approximation to

the Floquet Hamiltonian

$$\hat{H}_F = \hat{H}_0 + O\left(\frac{1}{\omega}\right)^2. \tag{5.4}$$

Higher order terms can be found in reference [29].

To first order, the Floquet Hamiltonian is therefore given by Hamiltonian's zeroth Fourier component which is equivalent to its average over one driving period. It is easy to see that the original Hamiltonian (2.3) does not lead to a meaningful result here, because the time-dependent driving term averages out and the time-independent part does not contain the driving at all. The reason for this is the fact, that the expansion of the time evolution operator in equation (5.1) is only justified for the original Hamiltonian if $\omega \gg \mu_i$ and $\omega \gg J$. Since we are interested in an approximation for arbitrary driving amplitudes, one needs to transform the original Hamiltonian such that only the internal energy scale J appears as a factor.

We are therefore required to gauge transform $\hat{H}(t)$ in a way, analogue to the one discussed in section 3.4. To find an appropriate gauge transformation, insert the Hamiltonian (2.3) into the equation for the gauge transformed Hamiltonian (3.17):

$$\hat{H}_G = \hat{U}_G^\dagger(t)\left(\hat{H}_{\text{tb}} + \hat{H}_{\text{drive}}(t)\right)\hat{U}_G(t) - \mathrm{i}\hbar\hat{U}_G^\dagger(t)\mathrm{d}_t\hat{U}_G(t)$$

The factors μ_i appearing in $\hat{H}_{\text{drive}}(t)$ can be canceled by choosing the gauge transformation $\hat{U}_G$ such that it removes the driving Hamiltonian:

$$\begin{aligned} 0 &= \hat{U}_G^\dagger(t)\hat{H}_{\text{drive}}(t)\hat{U}_G(t) - \mathrm{i}\hbar\hat{U}_G^\dagger(t)\mathrm{d}_t\hat{U}_G(t) \\ \Rightarrow \quad \mathrm{i}\hbar\mathrm{d}_t\hat{U}_G(t) &= \hat{H}_{\text{drive}}(t)\hat{U}_G(t). \end{aligned}$$

One solution to this differential equation is given by the gauge transformation

$$\hat{U}_G(t) = \exp\left(\frac{i}{\hbar}\left[\frac{\mu_1'}{\omega'}\sin(\omega t)\hat{c}_0^\dagger\hat{c}_0 + \frac{\mu_2}{\omega}\sin\left(\omega t + \phi\right)\hat{c}_l^\dagger\hat{c}_l\right]\right).$$

In this gauge, the gauge transformed Hamiltonian is given by

$$\hat{H}_G = \hat{U}_G^\dagger(t)\hat{H}_{\text{tb}}\hat{U}_G(t) \tag{5.5}$$

To calculate this gauge transformed Hamiltonian, one needs to determine how the annihilation operator $\hat{c}_j$ transforms. Following reference [28] this can be done in a few steps. For this, first, introduce the dimensionless time $\tau \equiv \omega t$ and use the rescaled driving parameters of equation (4.12) to rewrite

$$\begin{aligned} a &\equiv \frac{\mu_1'}{\omega'}\sin(\tau) \quad \text{and} \quad b \equiv \frac{\mu_2'}{\mu_1'}\frac{\sin\left(\tau + \phi\right)}{\sin(\tau)} \\ \Rightarrow \quad \hat{U}_G(\tau) &= \exp\left(ia\hat{V}\right) \quad \text{with} \quad \hat{V} = \hat{c}_0^\dagger\hat{c}_0 + b\hat{c}_l^\dagger\hat{c}_l \end{aligned}$$

The gauge transformed annihilation operator then reads

$$\begin{aligned}\hat{c}_j(a) &\equiv \hat{U}_G^\dagger(\tau)\hat{c}_j\hat{U}_G(\tau)\\ &= e^{-ia\hat{V}}\hat{c}_j e^{ia\hat{V}}.\end{aligned}$$

This operator can be determined by differentiating it with respect to a:

$$\begin{aligned}i\mathrm{d}_a\hat{c}_j(a) &= i\left(-ie^{-ia\hat{V}}\hat{V}\hat{c}_j e^{ia\hat{V}} + ie^{-ia\hat{V}}\hat{c}_j\hat{V}e^{ia\hat{V}}\right)\\ &= e^{ia\hat{V}}\left[\hat{V},\hat{c}_j\right]e^{ia\hat{V}}\end{aligned}$$

Even though the commutation relations of fermionic and bosonic creation and annihilation operators differ, it is easy to show that in both cases

$$\left[\hat{V},\hat{c}_j\right] = -(\delta_{j,0}+b\delta_{j,l})\hat{c}_j.$$

For fermionic operators, one might use $[\hat{A}\hat{B},\hat{C}] = A\{\hat{B},\hat{C}\} - \{\hat{B},\hat{C}\}B$ to proof this. The resulting differential equation

$$i\mathrm{d}_a\hat{c}_j(a) = -(\delta_{j,0}+b\delta_{j,l})\hat{c}_j(a)$$

with the initial condition $\hat{c}_j(0) = \hat{c}_j$ is solved by

$$\hat{c}_j(a) = \begin{cases} e^{ia}\hat{c}_0 & j=0\\ e^{iab}\hat{c}_l & j=l\\ \hat{c}_j & \text{else}\end{cases}.$$

Having calculated how the annihilation operator transforms under the gauge transformation $\hat{U}_G(\tau)$, the gauge transformed Hamiltonian (5.5) is given by

$$\begin{aligned}\hat{H}_G =& e^{-ia\hat{V}}\Bigg[-J\sum_{j\neq -1,0,l-1,l}(\hat{c}_j^\dagger\hat{c}_{j+1}+\hat{c}_{j+1}^\dagger\hat{c}_j)\\ &- J_1\sum_{j=-1,0}(\hat{c}_j^\dagger\hat{c}_{j+1}+\hat{c}_{j+1}^\dagger\hat{c}_j) - J_2\sum_{j=l-1,l}(\hat{c}_j^\dagger\hat{c}_{j+1}+\hat{c}_{j+1}^\dagger\hat{c}_j)\Bigg]e^{-ia\hat{V}}\\ =& -J\sum_{j\neq -1,0,l-1,l}(\hat{c}_j^\dagger\hat{c}_{j+1}+\hat{c}_{j+1}^\dagger\hat{c}_j)\\ &- J_1\left[e^{ia}\hat{c}_{-1}^\dagger\hat{c}_0 + e^{-ia}\hat{c}_0^\dagger\hat{c}_{-1} + e^{-ia}\hat{c}_0^\dagger\hat{c}_1 + e^{ia}\hat{c}_1^\dagger\hat{c}_0\right]\\ &- J_2\left[e^{iab}\hat{c}_{l-1}^\dagger\hat{c}_l + e^{-iab}\hat{c}_l^\dagger\hat{c}_{l-1} + e^{-iab} + \hat{c}_l^\dagger\hat{c}_{l+1} + e^{iab}\hat{c}_{l+1}^\dagger\hat{c}_l\right]\\ =& -\sum_j J_j\left[g_j(\tau)\hat{c}_j^\dagger\hat{c}_{j+1} + g_j^*(\tau)\hat{c}_{j+1}^\dagger\hat{c}_j\right]\end{aligned} \tag{5.6}$$

where the site-dependent hopping amplitudes J_j and the prefactors $g_j(\tau)$ are defined as

$$J_j = \begin{cases} J_1 & j \in \{-1, 0\} \\ J_2 & j = \{l-1, l\} \\ J & \text{else} \end{cases} \qquad \text{and} \qquad g_j = \begin{cases} e^{i\frac{\mu_1'}{\omega'}\sin(\tau)} & j = -1 \\ e^{-i\frac{\mu_1'}{\omega'}\sin(\tau)} & j = 0 \\ e^{i\frac{\mu_2'}{\omega'}\sin(\tau+\phi)} & j = l-1 \\ e^{-i\frac{\mu_2'}{\omega'}\sin(\tau+\phi)} & j = l \\ 1 & \text{else} \end{cases}.$$

The prefactors $g_j(\tau)$ can be rewritten by means of the Jacobi Anger expansion [30]

$$e^{iz\sin\theta} = \sum_{n=-\infty}^{\infty} \mathcal{J}_n(z) e^{in\theta}$$

with $z, \theta \in \mathbb{C}$ and $\mathcal{J}_n$ being the n-th Bessel function of the first kind. Fourier expanding $g_j(\tau)$ and using the Bessel function's property $\mathcal{J}_n(-z) = (-1)^n \mathcal{J}_n(-z)$, one finds

$$g_i(\tau) = \sum_n g_{jn} e^{in\tau} \qquad \text{with} \qquad g_{jn} = \begin{cases} \mathcal{J}_n\left(\frac{\mu_1'}{\omega'}\right) & j = -1 \\ (-1)^n \mathcal{J}_n\left(\frac{\mu_1'}{\omega'}\right) & j = 0 \\ \left(e^{i\phi}\right)^n \mathcal{J}_n\left(\frac{\mu_2'}{\omega'}\right) & j = l-1 \\ (-1)^n \left(e^{i\phi}\right)^n \mathcal{J}_n\left(\frac{\mu_2'}{\omega'}\right) & j = l \\ \delta_{n,0} & \text{else} \end{cases}.$$

With this, the gauge transformed Hamiltonian (5.6) can be expressed in terms of Fourier modes:

$$\hat{H}_G = \sum_n \hat{H}_n^G e^{in\tau} \qquad \text{with} \qquad \hat{H}_n^G = -\sum_j J_j \left[g_{jn} \hat{c}_j^\dagger \hat{c}_{j+1} + g_{j,-n}^* \hat{c}_{j+1}^\dagger \hat{c}_j \right].$$

It is apparent that as argued above, the gauge transformation $\hat{U}_G$ merged the time-independent and the driven part of the original Hamiltonian (2.3) into a single term that contains all internal and external energy scales. Before deriving the high frequency Floquet Hamiltonian from this gauge transformed Hamiltonian, let us discuss its physical meaning.

In section 4.1, it was argued that the quasienergy operator constructed from $\hat{H}(\mathrm{t})$ describes multiple tight binding chains that are each coupled to two other chains at the impurity sites $j \in \{0, l\}$. Using equation (3.13), the gauge transformed Hamiltonian leads to a quasienergy operator that appears way more complex: Here, at the impurity sites, each tight binding chain with Fourier index n' couples to each other chain of Fourier index n'' with an amplitude $g_{j,n'-n''} \sim \mathcal{J}_{n'-n''}(\mu_i/\omega)$. However, the situation simplifies drastically when deriving the high frequency approximation to the Floquet Hamiltonian

$$\hat{H}_{\text{eff}} \equiv \lim_{\omega\to\infty} \hat{H}_F$$

from $\hat{H}_G$. According to equation (5.4), $\hat{H}_{\text{eff}}$ is given by the zeroth Fourier component of $\hat{H}_G$

$$\hat{H}_{\text{eff}} = -J \sum_{j\neq -1,0,l-1,l} (\hat{c}_j^\dagger \hat{c}_{j+1} + \hat{c}_{j+1}^\dagger \hat{c}_j) - J_{1,\text{eff}} \sum_{j=-1,0} (\hat{c}_j^\dagger \hat{c}_{j+1} + \hat{c}_{j+1}^\dagger \hat{c}_j) - J_{2,\text{eff}} \sum_{j=l-1,l} (\hat{c}_j^\dagger \hat{c}_{j+1} + \hat{c}_{j+1}^\dagger \hat{c}_j) \tag{5.7}$$

with effective hopping amplitudes to the impurities

$$J_{i,\text{eff}} = J_i \mathcal{J}_0(\lambda_i) \quad \text{with} \quad \lambda_i = \frac{\mu_i'}{\omega'} = \frac{\mu_i}{\omega}, \quad i \in \{1,2\}. \tag{5.8}$$

Here, $\mathcal{J}_0(x)$ is the zeroth Bessel function of the first kind which is plotted in figure 5.1. It is impressive to see, that in the high frequency limit, the time-dependent Hamiltonian (2.3) breaks down to a time-independent effective one that describes a single homogeneous tight binding chain with modified hopping amplitudes to the two impurities $J_{i,\text{eff}}$ (figure 5.2). To describe this effective model, we will use the shorthand notation M_{HFD}. Here, the index HFD stands for 'high frequency discrete' model, do distinguish it from an analogue continuous model that will be derived in section 5.2. In the following section a method to compute transport through this high frequency model is presented.

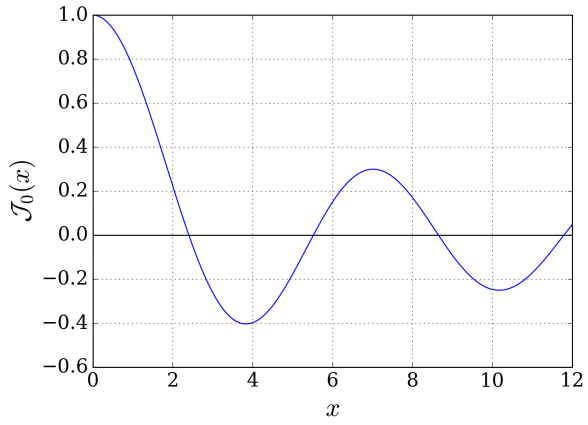

Figure 5.1: Zeroth Bessel function of the first kind which in the high frequency limit modulates the original hopping amplitudes to the impurities (equation (5.8))

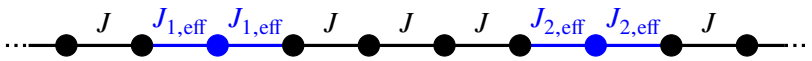

Figure 5.2: In the high frequency limit, the time-dependent tight binding chain described in section 2 behaves like a time-independent tight binding chain with modified hopping amplitudes to the two impurities. This is illustrated for a distance of $l = 5$ sites in between the two impurities.

5.1.2 Particle transport in the high frequency effective model

In the previous section 5.1.1, we found that the tight binding chain with two driven impurities can, for high driving frequencies, be described as a tight binding chain with effective hopping amplitudes to the

impurities but without any time-dependence. In this section, the transport properties of this effective model M_{HFD}, described by the Hamiltonian (5.7), are computed in a way that is partly analogue to the calculation of transport in the driven chain (section 4.2).

When computing transport of the driven tight binding chain in section 4.2, we started from the Floquet equation which is an eigenvalue equation for time-periodic systems. The Hamiltonian (5.7) whose transport properties we want to determine now, does not feature any time dependence. Therefore, to find the system's wavefunction $|\phi\rangle$, we simply start from the time independent Schrödinger equation

$$\hat{H}_{\mathrm{eff}} |\phi\rangle = \epsilon |\phi\rangle \tag{5.9}$$

and insert a general ansatz by writing the wavefunction in terms of single site amplitudes ϕ_j

$$|\phi\rangle = \sum_j \phi_j \hat{c}_j^\dagger |0\rangle$$

where, as in 4.2, $|0\rangle$ is the vacuum state of an empty tight binding chain.

The only combination of creation and annihilation operators appearing in the Schrödinger equation (5.9) is $(\hat{c}_k^\dagger \hat{c}_{k+1} + \hat{c}_{k+1}^\dagger \hat{c}_k)\hat{c}_j^\dagger$ which can be simplified as in equation (4.6). Collecting terms in equation (5.9) that act on the same site, yields the following recurrence relations for the single site wavefunction amplitudes:

$$-J_{1,\mathrm{eff}} \left(\phi_1 + \phi_{-1}\right) = \epsilon\phi_0 \tag{5.10}$$

$$-J\phi_{\pm 2} - J_1\phi_0 = \epsilon\phi_{\pm 1} \tag{5.11}$$

$$-J_{2,\mathrm{eff}} \left(\phi_{l+1} + \phi_{l-1}\right) = \epsilon\phi_l \tag{5.12}$$

$$-J\phi_{l\pm 2} - J_2\phi_l = \epsilon\phi_{l\pm 1} \tag{5.13}$$

$$-J\left(\phi_{j+1} + \phi_{j-1}\right) = \epsilon\phi_j \qquad \text{for} \quad j \notin \{-1, 0, 1, l-1, l, l+1\} \tag{5.14}$$

To find a solution to the Schrödinger equation which allows to determine the system's transport characteristics, one can make an analogue ansatz to equation (4.13) with an incoming wave from the left that is either reflected or transmitted at each impurity:

$$|\phi\rangle = \sum_{j<0} \left(e^{ikj} + re^{-ikj}\right) \hat{c}_j^\dagger |0\rangle + \phi_0 \hat{c}_0^\dagger |0\rangle + \sum_{0<j<l} \left(t'e^{ikj} + r'e^{-ikj}\right) \hat{c}_j^\dagger |0\rangle + \phi_l \hat{c}_l^\dagger |0\rangle + \sum_{j>l} te^{ikj} \hat{c}_j^\dagger |0\rangle \tag{5.15}$$

The only difference to the ansatz (4.13) to the time-dependent Floquet system lies in the fact that this system consists of multiple tight binding chains labeled by the Fourier index n. In contrast the high frequency effective Hamiltonian describes a single chain which simplifies the following calculations.

Before determining the scattering amplitudes of ansatz (5.15), note that inserting plane wave solutions e^{ikj} to the bulk recurrence relation (5.14) yields the dispersion relation of a homogeneous tight binding chain

$$\epsilon' \equiv \frac{\epsilon}{J} = -2\cos(k). \tag{5.16}$$

with the dimensionless energy ϵ'. From here on, analogously to equation (4.12), we use the rescaled

effective hopping amplitudes

$$J'_{i,\text{eff}} \equiv J_{i,\text{eff}}/J. \tag{5.17}$$

The scattering amplitudes are now computed by stepwise inserting the ansatz (5.15) into the recurrence relations . First, relation (5.11) gives

$$E = (1+r) = \left(t' + r'\right) \qquad \text{with} \qquad E \equiv J'_{1,\text{eff}}\phi_0. \tag{5.18}$$

Similarly, relation (5.13) yields

$$J'_{2,\text{eff}} e^{-ikl}\phi_l = t = t' + r' e^{-i2kl} \tag{5.19}$$

$$\Rightarrow \quad t = E - 2ir' e^{-ikl} \sin(kl)\,. \tag{5.20}$$

Note that the recurrence relations (4.8) and (4.10) that were derived for the Floquet system, describe single chain processes without coupling between chains and therefore yield equivalent results (4.16) and (4.17) as for the time-independent system. In contrast, equations (5.10) to (5.12) differ from equations (4.7) and (4.9) which do contain coupling terms.

Inserting the ansatz (5.15) into recurrence relation (5.10) yields

$$ir' = \frac{1}{\sin(k)}\left[e^{ik} - \frac{1}{\left(J'_{1,\text{eff}}\right)^2}\cos(k)\right]E - i \tag{5.21}$$

Combining the expressions (5.18) to (5.21) connecting the wavefunction amplitudes with relation (5.12) gives an equation for the coefficient E which is proportional to the wavefunction at site 0 (see equation (5.18)):

$$\begin{aligned} E = i\Bigg(& \sin\big(k(l-1)\big) + \left[e^{ik} - 2\frac{1}{\left(J'_{2,\text{eff}}\right)^2}\cos(k)\right]\sin(kl)\Bigg) \\ & \cdot\Bigg(- e^{ikl}\cos(k)\left[1 - \frac{1}{\left(J'_{2,\text{eff}}\right)^2}\right] \\ & \quad + \frac{1}{\sin(k)}\left[e^{ik} - \frac{1}{\left(J'_{1,\text{eff}}\right)^2}\cos(k)\right]\left[\sin\big(k(l-1)\big) + \left(e^{ik} - 2\frac{1}{\left(J'_{2,\text{eff}}\right)^2}\cos(k)\right)\sin(kl)\right]\Bigg)^{-1} \end{aligned} \tag{5.22}$$

Having found a closed expression for E, all wavefunction amplitudes can be computed from equations (5.18) to (5.21). For any incoming momentum k, we thus find one solution to the Schrödinger equation, that is a solution that solves the recurrence relations (5.10) to (5.14). We can therefore deduce that

we have found all possible solutions for the given situation and can proceed by determining the transmission probability as a function of the incoming momentum

$$
\begin{aligned}
T = |t|^2 =& 8(J'_{1,\mathrm{eff}})^4 (J'_{2,\mathrm{eff}})^4 \sin^4(k) \\
&\cdot \Big(\big[6 - 12\left((J'_{1,\mathrm{eff}})^2 + (J'_{2,\mathrm{eff}})^2\right) + 7\left((J'_{1,\mathrm{eff}})^4 + (J'_{2,\mathrm{eff}})^4\right) + 24(J'_{1,\mathrm{eff}})^2 (J'_{2,\mathrm{eff}})^2 \\
&\quad - 14\left((J'_{1,\mathrm{eff}})^4 (J'_{2,\mathrm{eff}})^2 + (J'_{2,\mathrm{eff}})^4 (J'_{1,\mathrm{eff}})^2\right) + 11(J'_{1,\mathrm{eff}})^4 (J'_{2,\mathrm{eff}})^4\big] \\
&+ 4\cos(2k)\big[2 - 4\left((J'_{1,\mathrm{eff}})^2 + (J'_{2,\mathrm{eff}})^2\right) + 2\left((J'_{1,\mathrm{eff}})^4 + (J'_{2,\mathrm{eff}})^4\right) + 8(J'_{1,\mathrm{eff}})^2 (J'_{2,\mathrm{eff}})^2 \\
&\quad - 4\left((J'_{1,\mathrm{eff}})^4 (J'_{2,\mathrm{eff}})^2 + (J'_{2,\mathrm{eff}})^4 (J'_{1,\mathrm{eff}})^2\right) + (J'_{1,\mathrm{eff}})^4 (J'_{2,\mathrm{eff}})^4\big] \\
&+ \cos(4k)\big[2 - 4\left((J'_{1,\mathrm{eff}})^2 + (J'_{2,\mathrm{eff}})^2\right) + \left((J'_{1,\mathrm{eff}})^4 + (J'_{2,\mathrm{eff}})^4\right) + 8(J'_{1,\mathrm{eff}})^2 (J'_{2,\mathrm{eff}})^2 \\
&\quad - 2\left((J'_{1,\mathrm{eff}})^4 (J'_{2,\mathrm{eff}})^2 + (J'_{2,\mathrm{eff}})^4 (J'_{1,\mathrm{eff}})^2\right) + (J'_{1,\mathrm{eff}})^4 (J'_{2,\mathrm{eff}})^4\big] \\
&- \cos\big(2k(l-2)\big)\big[1 - 3\left((J'_{1,\mathrm{eff}})^2 + (J'_{2,\mathrm{eff}})^2\right) + 2\left((J'_{1,\mathrm{eff}})^4 + (J'_{2,\mathrm{eff}})^4\right) + 9(J'_{1,\mathrm{eff}})^2 (J'_{2,\mathrm{eff}})^2 \\
&\quad - 6\left((J'_{1,\mathrm{eff}})^4 (J'_{2,\mathrm{eff}})^2 + (J'_{2,\mathrm{eff}})^4 (J'_{1,\mathrm{eff}})^2\right) + 4(J'_{1,\mathrm{eff}})^4 (J'_{2,\mathrm{eff}})^4\big] \\
&- \cos\big(2k(l-1)\big)\big[4 - 10\left((J'_{1,\mathrm{eff}})^2 + (J'_{2,\mathrm{eff}})^2\right) + 6\left((J'_{1,\mathrm{eff}})^4 + (J'_{2,\mathrm{eff}})^4\right) + 24(J'_{1,\mathrm{eff}})^2 (J'_{2,\mathrm{eff}})^2 \\
&\quad - 14\left((J'_{1,\mathrm{eff}})^4 (J'_{2,\mathrm{eff}})^2 + (J'_{2,\mathrm{eff}})^4 (J'_{1,\mathrm{eff}})^2\right) + 8(J'_{1,\mathrm{eff}})^4 (J'_{2,\mathrm{eff}})^4\big] \\
&- \cos(2kl)\big[6 - 12\left((J'_{1,\mathrm{eff}})^2 + (J'_{2,\mathrm{eff}})^2\right) + 6\left((J'_{1,\mathrm{eff}})^4 + (J'_{2,\mathrm{eff}})^4\right) + 22(J'_{1,\mathrm{eff}})^2 (J'_{2,\mathrm{eff}})^2 \\
&\quad - 10\left((J'_{1,\mathrm{eff}})^4 (J'_{2,\mathrm{eff}})^2 (J'_{2,\mathrm{eff}})^4 + (J'_{1,\mathrm{eff}})^2\right) + 4(J'_{1,\mathrm{eff}})^4 (J'_{2,\mathrm{eff}})^4\big] \\
&- \cos\big(2k(l+1)\big)\big[4 - 6\left((J'_{1,\mathrm{eff}})^2 + (J'_{2,\mathrm{eff}})^2\right) + 2\left((J'_{1,\mathrm{eff}})^4 + (J'_{2,\mathrm{eff}})^4\right) + 8(J'_{1,\mathrm{eff}})^2 (J'_{2,\mathrm{eff}})^2 \\
&\quad - 2\left((J'_{1,\mathrm{eff}})^4 (J'_{2,\mathrm{eff}})^2 + (J'_{2,\mathrm{eff}})^4 (J'_{1,\mathrm{eff}})^2\right)\big] \\
&- \cos\big(2k(l+2)\big)\big[1 - (J'_{1,\mathrm{eff}})^2 - (J'_{2,\mathrm{eff}})^2 + (J'_{1,\mathrm{eff}})^2 (J'_{2,\mathrm{eff}})^2\big]\Big)^{-1}. \qquad (5.23)
\end{aligned}
$$

A different way to write the same expression is given in appendix B.1 (equation (B.1)). The following sections aim to analyze this long expression by first considering different limiting cases for the hopping amplitudes and then relating the underlying effective model M_{HFD} to an analogue continuous model. Before turning to this analysis let us briefly discuss the effect of the hopping amplitudes' sign.

According to section 5.1.1 and as explicitly stated by equation (5.8), in M_{HFD}, the hopping amplitudes are modified by the zeroth Bessel function $\mathcal{J}_0(x)$. Since this function is negative for some values of x, the effective hopping can be negative as well. Equation (5.23), however, states that the transmission through the two impurities does not depend on the sign of $J'_{i,\mathrm{eff}}$ since they only appear in powers of 2 and 4. The reason for this is that, according to the dispersion relation (5.16), the absolute value of the particle's energy is symmetric with respect to the sign of the hopping amplitude. In fact the mapping $J \mapsto -J$ is equivalent to mirroring the momentum around $\pi/2$: $k = \pi/2 + k' \mapsto \pi/2 - k'$ where the transmission probability is equally symmetric, as will be discussed in section 5.3.1.

The physical reason behind these symmetries is the effective Hamiltonian's particle hole symmetry:

For non-interacting Hamiltonians like the effective Hamiltonian (5.7), application of particle hole conjugation (charge conjugation) $\hat{C}$ simply leads to a negative sign: $\hat{C}\hat{H}_{\text{eff}}\hat{C}^{-1} = -\hat{H}_{\text{eff}}$ [31]. Therefore, changing the sign of the hopping amplitude is equivalent to considering the transport properties of a hole instead of a particle, which in the case of single particle transport does not alter any equation.

In order to gain insight into transport properties of M_{HFD}, an illustrative way to understand the long expression for the transmission probability (5.23) is required. For this, in the following section 5.2, a system with continuous instead of a discrete position parameter is derived. We will learn that scattering and transport in this analogue model are described by more concise expressions which reproduce the low momentum limit of the discrete model.

5.2 High frequency analogue continuous model

In the previous section 5.1, the high frequency effective model to the tight binding chain with two AC driven impurities M_{HFD} was derived and transport in this model was computed. In order to later understand this effective model's transport characteristics, in this section an analogous one-dimensional system M_{HFC} with a continuous position parameter is constructed and, as for M_{HFD}, transport is calculated.

The effective discrete Hamiltonian (5.7) features no potential but the effective hopping amplitudes around sites 0 and l have a kinetic effect by leading to a change in momentum of an incident particle. To find a continuous model M_{HFC} with similar characteristics, we need to introduce the lattice spacing a into M_{HFD} and then relate the tight binding dispersion relation in the limit of small a to the dispersion relation in a continuous system. For this, rewrite the dimensionless momentum which was used up to here, as the product of a dimensioned momentum k_{dim} and the lattice spacing

$$k = k_{\mathrm{dim}} a. \tag{5.24}$$

Next, define a shifted energy $\epsilon_{\mathrm{shifted}}$ such that propagating particles with real momentum have positive energy [26]:

$$\epsilon_{\mathrm{shifted}} = \epsilon + 2J \overset{((5.16))}{=} 2J(1 - \cos(k_{\mathrm{dim}} a)). \tag{5.25}$$

Expanding the dispersion relation in the limit of small lattice spacing and equating with the continuum kinetic energy yields a relation between the hopping amplitude of a tight binding chain and an effective mass of a continuous system:

$$\epsilon_{\mathrm{shifted}} \to J a^2 k_{\mathrm{dim}}^2 \overset{!}{=} \frac{\hbar^2 k_{\mathrm{dim}}^2}{2m(x)} \qquad \Rightarrow \qquad J a^2 = \frac{\hbar^2}{2m(x)}. \tag{5.26}$$

Note that for $\frac{\hbar^2}{2m(x)}$ to stay finite, the continuum limit corresponds to simultaneously taking the limits $a \to 0$ and $J \to \infty$.

When working with dimensionless momentum k in units of the inverse lattice spacing as before, according to equation (5.24), the continuum limit corresponds to $k \to 0$. We therefore expect an analogue continuous model M_{HFC} to reproduce the low momentum results of the discrete model M_{HFD}.

Furthermore, equation (5.26) gives a prescription on rescaling physical quantities in an analogue continuous system: As all energetic quantities in the discrete system were rescaled by J^{-1} (equations (4.12) and (5.17)), the analogue quantities in M_{HFC} can be written in terms of $\frac{\hbar^2}{2m}$ to be comparable to the discrete system.

The impurities of M_{HFD} with Hamiltonian (5.7) are described by a local change in the hopping amplitude J. Equation (5.26) determines how such a change in the hopping amplitude can be represented in the continuous system in terms of an effective position-dependent mass $m(x)$. One finds the following relation between M_{HFD} and M_{HFC}:

$$J'_{i,\mathrm{eff}} \approx 0 \quad \leftrightarrow \quad m(x_i) \to \infty \qquad \text{and} \qquad J'_{i,\mathrm{eff}} \approx 1 \quad \leftrightarrow \quad m(x_i) \approx m_0 \tag{5.27}$$

with the bulk effective mass m_0 and the impurity positions $x_1 = 0$ and $x_2 = l$.

In the following section 5.2.1, such a continuous system is constructed which possesses two impurities that are characterized by local changes in the effective mass. We will find that such a system can be related to a system with two Dirac delta peaks by translating the position-dependent mass to an effective potential.

5.2.1 Effective position-dependent mass

As argued above, the continuous representation of the position-dependent hopping amplitude of M_{HFD} is given by an effective position-dependent mass function $m(x)$. However, the standard procedure to calculate transport in one-dimensional continuous systems can deal with potentials but not with position-dependent mass. Luckily, it is possible to translate a position-dependent mass to a system with a new position parameter y, a potential $\tilde{V}(y)$ and a constant mass by means of a so-called point-canonical transformation [32]. One starts from the Schrödinger equation for a particle with constant mass m:

$$\left\{\frac{\mathrm{d}^2}{\mathrm{d}y^2} - [\tilde{V}'(y) - E']\right\}\psi(y) = 0 \tag{5.28}$$

where according to the prescription induced by equation (5.26) the dimensionless potential and eigenenergy were introduced as

$$\tilde{V}'(y) = \frac{2m}{\hbar^2}\tilde{V}(y) \qquad \text{and} \qquad E' = \frac{2m}{\hbar^2}E.$$

Inserting the point-canonical transformation

$$y = q(x), \quad \psi(y) = g(x)\Phi(x)$$

into the Schrödinger equation (5.28) yields [32]

$$\left\{\frac{d^2}{dx^2} + \left(2\frac{g'}{g} - \frac{q''}{q'}\right)\frac{d}{dx} + \left(\frac{g''}{g} - \frac{q''}{q'}\frac{g'}{g}\right) - (q')^2\left[\tilde{V}'(q(x)) - E'\right]\right\}\Phi(x) = 0. \tag{5.29}$$

In turn, the Schrödinger equation with position-dependent mass $m(x)$ is given by [32]

$$\left\{\frac{\mathrm{d}^2}{\mathrm{d}x^2} - \frac{M'}{M}\frac{\mathrm{d}}{\mathrm{d}x} - M[V'(x) - E']\right\}\Phi(x) = 0.$$

where potential and mass were rescaled according to

$$V'(x) = \frac{2m_0}{\hbar^2}V(x) \qquad \text{and} \qquad M(x) = \frac{m(x)}{m_0}. \tag{5.30}$$

One finds that this position-dependent mass Schrödinger equation can be related to the point-canonically

transformed Schrödinger equation (5.29) by demanding

$$q(x) = \int_{-\infty}^{x} \sqrt{M(x')}\mathrm{d}x' \tag{5.31}$$

$$V'(x) = \tilde{V}'(q(x)) + \frac{1}{4M}\left[\frac{M''}{M} - \frac{7}{4}\left(\frac{M'}{M}\right)^2\right]. \tag{5.32}$$

To be able to transform the position-dependent mass $M(x)$ into a potential $V'(x) \neq 0$, according to equations (5.31) and (5.32), $\sqrt{M(x)}$ needs to be integrable and the first derivative of the mass function should not vanish: $M'(x) \neq 0$. Additionally, the requirements (5.27) need to be met for the position-dependent mass to resemble the tight binding chain with two impurities. One could be tempted to describe the impurities in $M(x)$ by means of the Dirac delta distribution with terms $\mathrm{const}_1 \cdot \delta(x)$ and $\mathrm{const}_2 \cdot \delta(x-l)$. Considering that the derivative of the delta distribution is determined by [33]

$$f(x) \cdot \delta'(x) = -f'(x) \cdot \delta(x) \tag{5.33}$$

such terms would produce $M'(x) = 0$ and would therefore not lead to a non-vanishing potential $V(x)$ (see equation (5.32)).

Another possibility to construct a one-dimensional system with a (rescaled) position-dependent mass $M(x)$ that only differs from 1 around $x \in \{0, l\}$ is the function

$$M(x) = 1 - \nu_1 \exp\left(-\frac{|x|}{\sigma}\right) - \nu_2 \exp\left(-\frac{|x-l|}{\sigma}\right). \tag{5.34}$$

Here, the strength of the impurities is described by parameters ν_i. $\nu_i = 0$ corresponds to no impurity, whereas $\nu_i > 0$ describes a decrease in kinetic energy analogously to $J' < 1$ in the discrete case and $\nu_i < 0$ increases the kinetic energy like $J' > 1$. The parameter σ describes the peak width, so the smaller σ, the more localized are the impurities. In figure 5.3, $M(x)$ is plotted for different values of $\nu_1 = \nu_2 = \nu$.

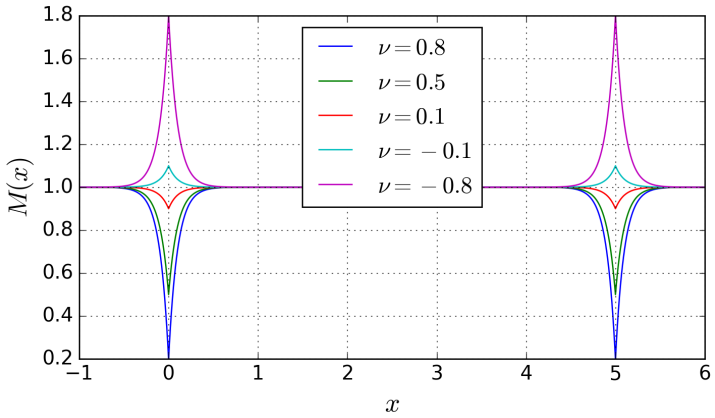

Figure 5.3: Position-dependent mass of equation (5.34) for different values of ν with $l = 5$, $\sigma = 0.1$.

Let us apply the point canonical transformation introduced above, that is equations (5.31) and (5.32), to the analogue continuous system described by the position-dependent mass (5.34). Unfortunately, there is no way to analytically solve the integral in equation (5.31) to perform the coordinate transformation $y = q(x)$. However, by construction one finds $M(x) \approx 1$ except for small regions around the impurities. Especially when σ is chosen to be small, it is thus legitimate to neglect the coordinate shift introduced by equation (5.31) and replace $y \mapsto x$.

Furthermore, in our system $V'(x) = 0$ since there is no potential in the Hamiltonian (5.7) of M_{HFD}. By inserting this and equation (5.34) into equation (5.32), one thus obtains the effective potential

$$\tilde{V}'(x) = \frac{1}{4M^2(x)}\frac{1}{\sigma^2}\left[\frac{7}{4}\frac{1}{M(x)}\left(\operatorname{sign}(x)\nu_1 \exp\left(-\frac{|x|}{\sigma}\right) + \operatorname{sign}(x-l)\nu_2 \exp\left(-\frac{|x-l|}{\sigma}\right)\right)^2 + \left(\nu_1 \exp\left(-\frac{|x|}{\sigma}\right) + \nu_2 \exp\left(-\frac{|x-l|}{\sigma}\right)\right)\right]. \tag{5.35}$$

Unfortunately, there is no analytical way to calculate transport through this potential. One could therefore either proceed by determining the transmission probability numerically, e. g. using the method described in reference [34]. Such a numerical calculation is performed in appendix B.2. It is however hard to gain a deeper physical understanding from these results. Instead, one can proceed by regarding the shape of the effective potential (5.35) plotted in figure 5.4 for the values of ν from figure 5.3.

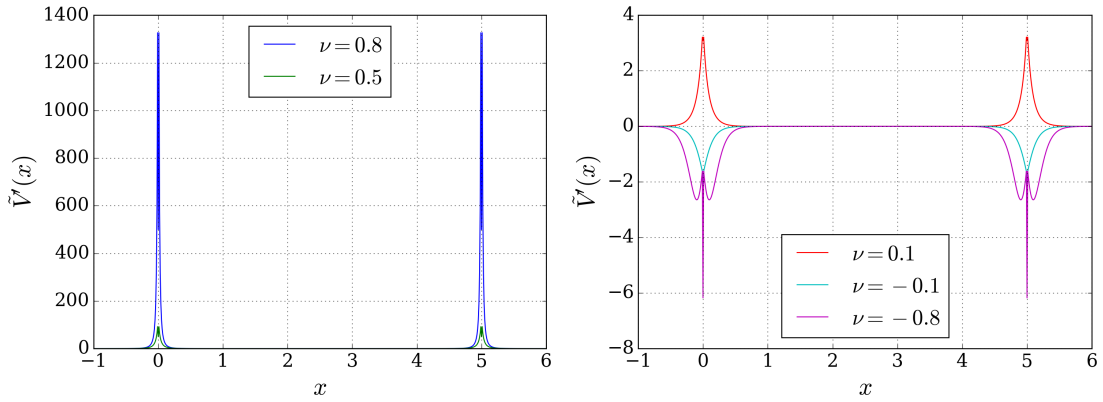

Figure 5.4: Effective potential obtained from the position-dependent mass (5.34) with the values of ν from figure 5.3 using equation (5.32). Parameters: $l = 5$, $\sigma = 0.1$.

From figure 5.3, it is apparent that, at least for $\nu \gtrsim -0.1$ and in the limit $\sigma \to 0$, each peak of the effective potential approaches a Dirac delta function. In this limit, the potential seems to be described by a double delta potential of the form

$$V'_{\text{double delta pot.}}(x) = V'_1\delta(x) + V'_2\delta(x-l). \tag{5.36}$$

with $V'_i \lesseqgtr 0$ for $\nu_i \lesseqgtr 0$. Note that the according physical potential $V_{\text{double delta pot.}}(x)$ has dimension energy, whereas the V_i have dimension energy × length. Nevertheless, since we are working with dimensionless momentum k and thus dimensionless length, both parameters are rescaled according to the same equation (5.30). In order to obtain dimensional quantities to compare to M_{HFD}, one is therefore

required to multiply with the according powers of the discrete lattice spacing a (equation (5.24)).

In order to find a relation between $\tilde{V}'(x)$ and the double delta potential, it is instructive to split $\tilde{V}'(x)$ into the two peaks and determine the integral over one of the peaks:

$$\begin{aligned}
&\tilde{V}'(x) \approx \tilde{V}'^{\nu_1}_{\text{peak}}(x) + \tilde{V}'^{\nu_2}_{\text{peak}}(x-l) \\
\text{with}\quad &\tilde{V}'^{\nu}_{\text{peak}}(x) = \frac{\nu \exp\left(-\frac{|x|}{\sigma}\right)}{4\left(1-\nu\exp\left(-\frac{|x|}{\sigma}\right)\right)^2}\frac{1}{\sigma^2}\left[\frac{7}{4}\frac{\nu\exp\left(-\frac{|x|}{\sigma}\right)}{\left(1-\nu\exp\left(-\frac{|x|}{\sigma}\right)\right)}+1\right] \\
\Rightarrow\quad &\int_{-\infty}^{\infty} \mathrm{d}x \tilde{V}'^{\nu}_{\text{peak}}(x) = \frac{(8-\nu)\nu}{16(1-\nu)^2\sigma} \qquad \text{if} \qquad 0 \le \nu \le 1. \qquad (5.37)
\end{aligned}$$

This can be related to the double delta potential (5.36), by considering

$$V'_{\text{double delta pot.}}(x) = V'_1\delta(x) + V'_2\delta(x-l) \qquad \text{and} \qquad \int_{-\infty}^{\infty}\mathrm{d}x V'_i\delta(x) = V'_i$$

Therefore, for $0 \le \nu \le 1$, the effective potential of equation (5.35) that results from the position-dependent mass (5.34) can be related to the double delta potential by setting

$$V'_i = \frac{(8-\nu_i)\nu_i}{16(1-\nu_i)^2\sigma} \qquad \Leftrightarrow \qquad \nu_i = \frac{4(1+4\sigma V'_i - \sqrt{1+7\sigma V'_i})}{1+16\sigma V'_i}. \qquad (5.38)$$

We have thus found that for $0 \le \nu_i \le 1$ and for narrow impurities $\sigma \to 0$, the continuous position-dependent mass system (5.34) that we constructed to understand M_{HFD}, behaves like a system with two delta peak potentials. And whilst transmission through the effective potential $\tilde{V}'(x)$ can only be calculated numerically, transport through one or multiple Dirac delta peaks can be computed analytically. Therefore, we arrived at a simple description of scattering off two impurities in a one-dimensional system where we can hope to understand features that we observe similarly inM_{HFD}.

We will proceed by deriving the scattering wavefunction in the system with two Dirac delta peaks in the following section 5.2.2. In appendix B.2, the resulting transmission will be compared to the numerically determined transmission through the effective potential (5.35) using relation (5.38). Here, also the case of $\nu > 1$ is regarded, where the relations (5.37) and (5.38) do not hold.

5.2.2 Double delta potential

In the previous section 5.2.1, a continuous model was found, that relates a tight binding chain with two impurities to a system with position-dependent mass and then to an effective potential. For impurities with small spacial extent this effective potential approaches a double Dirac delta potential. From now we will refer to this model as M_{HFC}. To gain understanding of the previous models, it is instructive to analyze transport through the double delta potential of equation (5.36):

$$V'_{\text{double delta pot.}}(x) = V'_1\delta(x) + V'_2\delta(x-l).$$

Transport through such a system has been studied extensively by means of different methods of scattering analysis [35–38]. In this section, we reproduce the findings of these papers using the standard

approach of solving the Schrödinger equation analogously to the discrete computation performed for the M_{HFD} in section 5.1.2. We again start with an incoming plane wave from the left that has different scattering amplitudes on the left, in between and on the right of the two potential peaks:

$$\psi(x) = \begin{cases} e^{ikx} + re^{-ikx} & x \leq 0 \\ t'e^{ikx} + r'e^{-ikx} & 0 < x \leq l \\ te^{ikx} & l < x \end{cases}. \tag{5.39}$$

By demanding continuity of the wavefunction and integrating over the Schrödinger equation to calculate the discontinuities in the first derivative of the wavefunction, a system of four equations is obtained. The solution is given by:

$$\begin{aligned} t &= \frac{1}{D} 4k^2 \\ r = -\frac{1}{D}\left[2ik\left(V_1' + e^{2ikl}V_2'\right) + \left(e^{2ikl} - 1\right)V_1'V_2'\right] &= -\frac{\left(2ik\left(V_1' + e^{2ikl}V_2'\right) + \left(e^{2ikl} - 1\right)V_1'V_2'\right)}{4k^2} \cdot t \\ r' = -\frac{1}{D} 2ie^{2ikl}kV_2' &= -\frac{ie^{2ikl}V_2'}{2k} \cdot t \\ t' = \frac{1}{D} 2k\left(2k + iV_2'\right) &= \frac{2k + iV_2'}{2k} \cdot t \end{aligned} \tag{5.40}$$

with the denominator

$$D = \left(2k + iV_1'\right)\left(2k + iV_2'\right) + e^{2ikl}V_1'V_2'.$$

From this, the transmission is calculated to

$$T = |t|^2 = \frac{16k^4}{\left[4k^2 - V_1'V_2'(1 - \cos(2kl))\right]^2 + \left[2k\left(V_1' + V_2'\right) + V_1'V_2'\sin(2kl)\right]^2}. \tag{5.41}$$

In appendix B.2, this analytical transport probability through the double delta potential is compared to the numerical transport probability for the position-dependent mass system derived in section 5.2.1. The results in this appendix illustrate that, indeed, the same transmission spectrum is retrieved.

In contrast to the effective potential (5.35) determined in section 5.2.1, we are thus able to determine transport through the double delta potential analytically which permits to well analyze the characteristics of transport. This is especially important since the expression for transport through the double delta potential is way more concise than the expression (5.23) which we found for M_{HFD} in section 5.1.2. After quantitatively relating M_{HFD} to M_{HFC} in the next subsection 5.2.3, we will therefore use the continuous transmission probability (5.41) to explain features of transport in M_{HFD} in the next section 5.3.

5.2.3 Relation between discrete and continuous model

After having determined the transmission probability through a set of two Dirac delta potential peaks it is time to relate this continuous model M_{HFC} to the high frequency discrete one that it is supposed to resemble. This relation will then be used in the following section 5.3 to thoroughly compare their transport characteristics.

As argued in section 5.2.2, M_{HFC} can be seen as the low momentum limit of M_{HFD}. For this reason, it is sensible to relate the two models to each other at small momenta. Therefore, we consider the low momentum Taylor expansion of the transmission probability in M_{HFD} (5.23) and in M_{HFC} given by equation (5.41):

$$\text{discrete model:} \quad T_{k\to 0} = \frac{(J'_{1,\mathrm{eff}})^4 (J'_{2,\mathrm{eff}})^4 k^2}{\left(2l - (2l-1)\left((J'_{1,\mathrm{eff}})^2 + (J'_{2,\mathrm{eff}})^2\right) + 2(l-1)(J'_{1,\mathrm{eff}})^2 (J'_{2,\mathrm{eff}})^2\right)^2} + O(k)^4$$

$$\text{and continuous model:} \quad T_{k\to 0} = \frac{4k^2}{(lV'_1V'_2 + V'_1 + V'_2)^2} + O(k)^4.$$

By equating these two expressions, one finds that for low momenta, M_{HFD} and M_{HFC} can be translated to each other by relating the impurity strengths as

$$V'_i = -2\left(\frac{J'^2_{i,\mathrm{eff}} - 1}{J'^2_{i,\mathrm{eff}}}\right) = 2\left(\frac{1}{J'^2_{i,\mathrm{eff}}} - 1\right) \qquad \Leftrightarrow \qquad J'_{i,\mathrm{eff}} = \frac{1}{\sqrt{V'_i/2 + 1}}. \tag{5.42}$$

Here, only the case of positive hopping amplitudes was considered, since, as argued in section 5.1.2, for single particles the sign of the hopping amplitude does not affect transport. This relation (5.42) is plotted for symmetric impurities with $J'_{1,\mathrm{eff}} = J'_{2,\mathrm{eff}} \equiv J'$ and $V'_1 = V'_2 \equiv V'$ in figure 5.5, which illustrates the divergent delta potential height V' for small impurity hopping amplitudes J'. Furthermore, it is interesting to note that, according to relation (5.42), positive hopping amplitudes $J' > 0$ map to peak heights $-2 < V'$ and smaller V' do not have a counterpart in M_{HFD}.

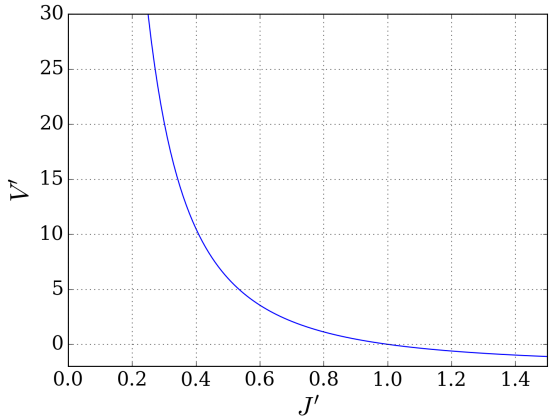

Figure 5.5: Relation between the discrete system of section5.1.2 and the continuous one of section 5.2.2 by plotting V' as a function of J' using relation (5.42).

With this, the discussion of M_{HFC} can be closed. In this section, we have explained how the impurities with effective hopping amplitudes in M_{HFD} can be represented in terms of a position-dependent mass in a continuous model M_{HFC}. It was shown that such a position-dependent mass can readily be translated into a potential consisting of two distinct peaks and how this potential can be described in terms of Dirac delta distributions. Finally, the transmission probability through such a set of two delta peaks was computed as a function of the impurity strength. This impurity strength was then quantitatively related to the effective impurity hopping amplitude of M_{HFD} derived in section 5.1.1. This relation will be used in the following section 5.3 to discuss the high frequency model's transport spectrum and to explain characteristic features of transport.

5.3 Explanation of transport characteristics

In section 5.1.1, it was shown that a tight binding chain with two AC driven impurities reduces, in the limit of high frequency, to a time-independent model M_{HFD} with effective hopping amplitudes to the two impurity sites. Transport characteristics were computed for M_{HFD} in section 5.1.2. To gain physical insight into these features, in section 5.2, an analogue continuous model M_{HFC} was developed leading to a system with two delta potentials at the positions of the impurities. A quantitative relation between M_{HFD} and M_{HFC} was found by using the fact that M_{HFC} describes particularly well the low momentum region of the transmission spectrum in the discrete model M_{HFD}.

We begin this section by briefly summarizing the transport properties of the high frequency models with a single impurity in section 5.3.1. In section 5.3.2, we discuss examples of the transmission spectra of M_{HFD} and M_{HFC} with two impurities for varying impurity strengths J' and V'. Several interesting transport characteristics are found and explained in the consecutive sections. In section 5.3.3, the sharp transmission peaks that are observed for strong impurities $J' \to 0$ are explained by identifying confined wavefunction modes. A change in the impurity strength leads to a shift in the momentum of maximal transmission, which is explained in section 5.3.4 by means of M_{HFC}. Finally, for the case of increased effective hopping $J' > 1$ a value of J' is identified where transmission is maximal at zero momentum. This feature of the transmission spectrum is explained in section 5.3.5 by relating it to the number of bound states that are present for $J' > 1$.

5.3.1 Transport through a single impurity in the limit of high frequency

Before considering the full high frequency models with two impurities in the following chapters, let us first summarize transport through a single static impurity. Transport through the resulting discrete model has been analyzed thoroughly in references [21, 26, 27]. Setting $J_{2,\mathrm{eff}} = J$ in equation (5.23) removes the second impurity, and one obtains the transmission probability [21]

$$T_{J'_{2,\mathrm{eff}}=1} = \frac{\sin^2(k)}{\sin^2(k) + \left(1/\left(J'_{1,\mathrm{eff}}\right)^2 - 1\right)^2 \cos^2(k)}. \tag{5.43}$$

Transmission through a single delta potential, obtained as the analogue continuous model M_{HFC} in the high frequency limit, has been analyzed in standard text books such as [39]. The transmission probabiliy through this potential is obtained from equation (5.41) by setting $V'_2 = 0$ [39]:

$$T_{V'_2=0} = \frac{k^2}{k^2 + \left(V'_1/2\right)^2}. \tag{5.44}$$

As found in section 5.2.3, the two equations (5.43) and (5.44) for transmission through a single impurity in the high frequency limit coincide in the limit $k \to 0$ when using relation (5.42) between J_i and V'_i. This is illustrated in figure 5.6, where the transmission spectra M_{HFD} and M_{HFC} are compared for different values of $J'_{1,\mathrm{eff}}$ and the corresponding peak heights V'_1.

From figure 5.6 and equation (5.43), it is apparent that transmission in both models increases monotonically in the range $k \in (0, \pi/2)$. Due to the symmetry of the terms $\sin^2(k)$ and $\cos^2(k)$ around $k = \pi/2$, the transmission in M_{HFD} is perfect at $k = \pi/2$ and decreases for $k > \pi/2$ mirrored

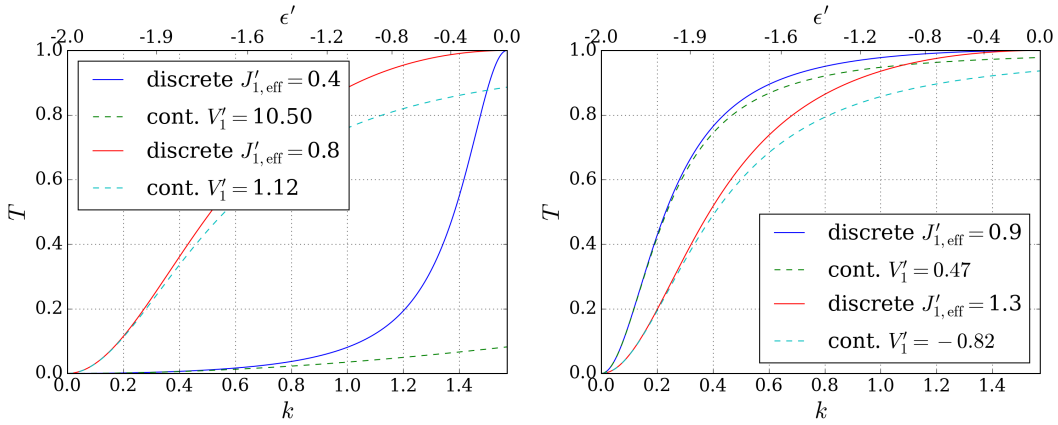

Figure 5.6: Comparison of the transmission spectra of M_{HFD} and M_{HFC} with different strengths V'_1 and $J'_{1,\mathrm{eff}}$ of a single impurity. The parameters V'_1 and $J'_{1,\mathrm{eff}}$ are related by equation (5.42). The case of $J'_{1,\mathrm{eff}} = 1$ is not shown, since it corresponds to no impurity at all and thus leads to perfect transmission over the entire spectrum.

to the increase at $k < \pi/2$. This behavior stems from the symmetry of the tight binding dispersion relation (5.16) around $k = \pi/2$ where the particle energy is $\epsilon = 0$ independently of the hopping amplitude. Therefore, at this specific energy, the impurity does not have any effect on the incoming particle which is hence fully transmitted.

At any other momentum, the dispersion relations away from the impurity and at the impurity differ more, the more $J'_{1,\mathrm{eff}}$ deviates from 1, leading to lower transmission. Note however that the factor

$$\left(1/\left(J'_{1,\mathrm{eff}}\right)^2 - 1\right)^2$$

which appears in the transmission probability (5.43) through a single impurity is not symmetric around $J' = 1$. This is why transmission at $J' > 1$ does not decrease in the same manner as for $J' < 1$.

The transmission spectrum of M_{HFC} coincides with the one of M_{HFD} at low momenta where the approximations $\sin(k) \approx k$ and $\cos(k) \approx 1$ hold. At larger momenta, the transmission spectra of M_{HFC} lie below the ones of M_{HFD}. Since the continuous dispersion relation (5.25) does not have any symmetry around $k = \pi/2$, the continuous transmission spectra do not show any feature at this momentum. In contrast to the discrete spectra, the continuous transmission keeps increasing monotonically for $k > \pi/2$, approaching $T = 1$ in the limit $k \to \infty$ where the delta potential height is negligible compared to the particle energy. It is finally worth noting that the continuous single impurity transmission depends on $\left(V'_1\right)^2$ and is thus independent of the potential's sign. With this, we can close the discussion of transport through a single static impurity and turn towards the transmission spectra of the high frequency model with two impurities.

5.3.2 Transmission spectra and perfect transmission

In the previous chapter, we found that transmission through a single impurity in the high frequency limit increases monotonously for momenta of an incoming particle in the range $k \in (0, \pi/2)$ with $T = 1$ at $k = \pi/2$. Above this momentum, the transmission spectrum is mirrored. Furthermore, the

transmission decreases the further $J'_{1,\text{eff}}$ is from 1. In this section, we 'switch on' the second impurity and compare the resulting transmission spectra to the ones of a single impurity. In figure 5.7, the transmission spectrum of M_{HFD} is plotted for different symmetric impurity strengths, meaning that the hopping amplitudes to the first and the second impurity are identical: $J'_{1,\text{eff}} = J'_{1,\text{eff}} \equiv J'$. These hopping amplitudes are translated into an impurity strength V' of M_{HFC} using relation (5.42) and the corresponding transmission spectra are compared to those of M_{HFD}.

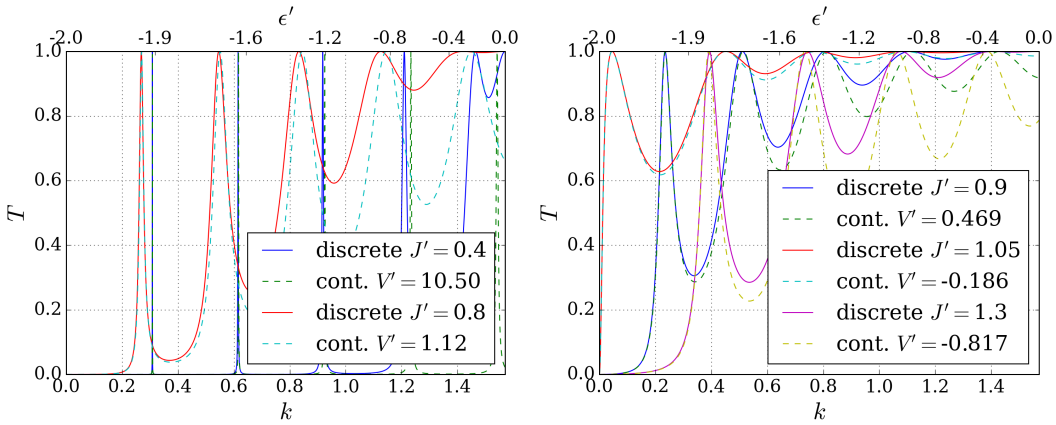

Figure 5.7: Comparison of the transmission spectra of M_{HFD} and M_{HFC} with $l = 10$ for different impurity strengths. V' and J' are related by equation (5.42). This figure can be compared to figure 5.6 where transmission through a single impurity of the same strengths is plotted.

The spectra of figure 5.7 give us a first insight into various transmission properties of the high frequency model with two impurities. At each symmetric impurity strength, besides $k = \pi/2$, perfect transmission is observed for various incoming momenta. The transmission spectra seem to oscillate around the single impurity spectra of figure 5.6. While the transmission peaks are sharp at small J', they broaden for increasing J' and the momenta of perfect transmission shift towards lower values. These two effects are explained thoroughly in sections 5.3.3 and 5.3.4. Furthermore, there is a hopping amplitude $J' > 1.05$ for which the first transmission maximum occurs at zero momentum. This effect is named threshold anomaly [36, 38] and is related to the appearance of bound states as discussed in section 5.3.5.

Let us first quantify the effect of perfect transmission which is observed in figure 5.7 and which will guide us to a deeper understanding of the two systems in the following sections. First of all, as for the single impurity case described in section 5.3.1, one finds that the transmission spectrum is symmetric around the incoming momentum of $k = \pi/2$ and always features perfect transmission at this momentum independently of the effective hopping amplitudes. This can again be explained by the fact that according to the dispersion relation (5.16), the particle's energy on the tight binding chain at $k = \pi/2$ is independent of the hopping amplitude and therefore does not 'see' any impurity.

The momenta of perfect transmission are given by the roots of the reflection amplitudes. The reflection amplitude in M_{HFD} is found from equations (5.18) to (5.22) and its roots for symmetric

impurities are given by the equation

$$\begin{aligned} 0 &= \left(J'^2 - 1\right)\left(-1 + e^{2ikl}\right)\cos(k) - 2iJ'^2\left(1 + e^{2ikl}\right)\sin(k) \\ \Rightarrow \quad \frac{J'^2 - 1}{J'^2} &= \frac{\tan(k)}{\tan(kl)}. \end{aligned} \tag{5.45}$$

The reflection amplitude of M_{HFC} is given by equation (5.40) and for symmetric impurities its roots are given by

$$\begin{aligned} 0 &= 2ik\left(1 + e^{2ikl}\right) + \left(1 - e^{2ikl}\right)V' \\ \Rightarrow \quad \frac{V'}{2} &= -\frac{k}{\tan(kl)}. \end{aligned} \tag{5.46}$$

This condition for perfect transmission through a symmetric double delta potential has been found before in [36].

As argued before, we expect the analogue continuous limit to reproduce the low momentum results of M_{HFD}. Comparing the transcendent equations (5.45) and (5.46) in the limit of small momenta where $\tan(k) \approx k$, we retrieve the analytic relation (5.42) between V' and J'.

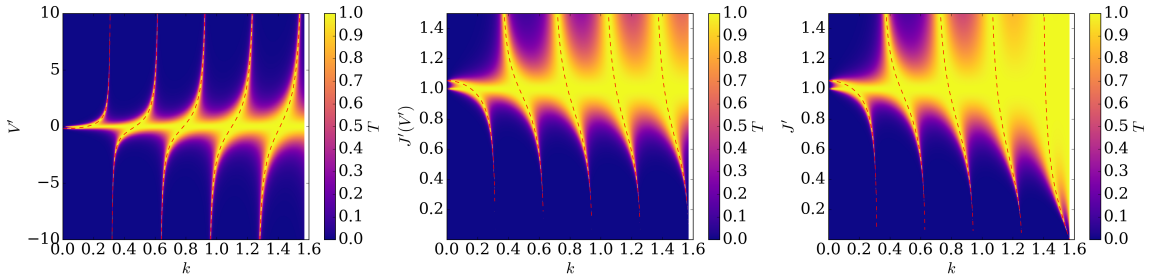

Figure 5.8: Transmission as a function of momentum and impurity strength with the curves of perfect transmission highlighted according to equations (5.46) (M_{HFC}) and (5.45) (M_{HFD}). Left: Transmission for M_{HFC} calculated from equation (5.41). Center: Transmission for M_{HFC} calculated from equation (5.41) where the peak height V' is translated into a hopping amplitude J' according to relation (5.42). This relation mirrors the the transmission spectrum of the left figure on the x-axis and then stretches it along the y-axis. Right: Transmission for M_{HFD} given by equation (5.23).

Figure 5.8 illustrates the curves of perfect transmission on top of transmission heat maps for M_{HFD} and M_{HFC}. In the following sections, we discuss how perfect transmission appears in different limits of the impurity strengths J' and V'. We will begin with strong impurities ($J' \to 0$, $V' \to \pm\infty$) where very sharp transmission peaks are found (see figures 5.7 and 5.8).

5.3.3 Resonances and confined modes at strong impurities

In section 5.3.2, we observed that for M_{HFD}, sharp transmission peaks appear for strong impurities with $J' \to 0$. In figure 5.9, this is illustrated for $J' = 0.4$. Using the relation $J' \leftrightarrow V'$ of equation (5.42), one finds that this effective hopping amplitude corresponds to an impurity strength in M_{HFC} of $V' = 10.5$. The corresponding spectrum for M_{HFC} is also plotted in figure 5.9.

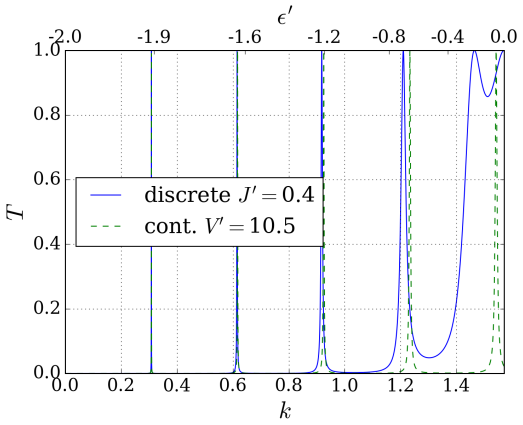

Figure 5.9: Comparison of the transmission spectra of M_{HFD} and M_{HFC} with $l = 10$ and strong impurities with $J' = 0.4$ and $V' = 10.5$.

In section 5.2, we explained that M_{HFC} describes the low momentum limit of M_{HFD} which is why the two models were related to each other in this limit with equation (5.42). Thus, the spectra of discrete and continuous model plotted in figure 5.9 match best for small momenta. This can be seen quantitatively from the Taylor series of the transmission probabilities (equations (5.23) and (5.41)) for a strong impurity:

$$\begin{aligned} \text{discrete model:} \quad T_{J'\to 0} &= \frac{\tan^4(k)}{4\sin^2(kl)} J'^8 + O(J')^{10}, \\ \text{continuous model:} \quad T_{V'\to\pm\infty} &= \frac{k^4}{4\sin^2(kl)} \left(\frac{2}{V'}\right)^4 + O\left(\frac{1}{V'}\right)^5. \end{aligned} \tag{5.47}$$

Recognizing that in the limit of strong impurities $J' \to 0$, the relation (5.42) between J' and V' becomes $V' = 2/J'^2$, the continuous transmission corresponds to the low frequency limit $\tan(k) \approx k$ of the discrete transmission. The fact that the strong impurity limit equation holds up to order $O(J')^9$ justifies to consider $J' = 0.4$ which is plotted in figure 5.9 as a strong impurity.

The transmission spectra of figure 5.9 can be well understood by means of the strong impurity transmission amplitudes (5.47): In the strong impurity limit with $J' \to 0$ and $V' \to \pm\infty$, the two impurities form large barriers making it unlikely for an incoming particle to tunnel through. Here the terms J'^8 and $(V')^{-4}$ create a background with nearly vanishing transmission amplitude. The sharp transmission peaks that are observed for a few momenta in the transmission spectra of figure 5.9, in turn, stem from a vanishing denominator in equation (5.47) with

$$\sin(kl) = 0 \qquad \Rightarrow \qquad k = n\frac{\pi}{l}.$$

Interestingly, this relation is also known to describe modes of an optical resonator [40]. As in a resonator, the transmission peaks are an effect of constructive interference: A wave that tunnels through the first impurity and is reflected on the second one has picked up a phase of $k \cdot 2l$ when arriving back at the first impurity. Constructive interference with a wave from a previous reflection

takes place if the phase difference is an integer multiple of 2π yielding momenta of constructive interference

$$k \cdot 2l = n \cdot 2\pi \qquad \Rightarrow \qquad k = n\frac{\pi}{l}.$$

To check whether it is legitimate to identify the transmission peaks of M_{HFD} and M_{HFC} as resonances, let us determine the poles of the transmission amplitude in both models [41]. For symmetric impurities, the continuous transmission amplitude (5.40) has poles at

$$0 = (2k + iV')^2 + e^{2ikl}\left(V'\right)^2 \qquad \Rightarrow \qquad V' = \frac{2ik}{1 \pm e^{ikl}} \tag{5.48}$$

where the '+' ('−') solutions yield symmetric (antisymmetric) wavefunctions. This resonance condition was found in reference [38] where it was emphasized that, interestingly, the resonance condition is different from the condition for perfect transmission (5.46). As discussed in reference [42], this effect is also observed for other standard potentials like the rectangular potential well/barrier and is due to the fact that other background resonances contribute to the transmission probability and shift the transmission maximum away from the pole. As discussed in references [38, 43], in the limit of strong impurities $|V'| \gg k$, the resonance condition (5.48) and the perfect transmission condition (5.46) simplify to the same condition $k = n\pi/l$. This is why in this limit, it is legitimate to identify the transmission maxima as resonant modes of the system.

Equally, the resonances of M_{HFD} are given by the poles of the transmission amplitude which is determined from equations (5.18) to (5.22). One obtains poles at

$$\begin{aligned} 0 =& J'^4 e^{ik}\left(\sin\big(k(l-1)\big) + e^{ik}\sin(kl)\right) \\ &- J'^2\cos(k)\left(\left(J'^2-1\right)e^{ikl}\sin(k) + \sin\big(k(l-1)\big) + 3e^{ik}\sin(kl)\right) \\ &+ 2\cos^2(k)\sin(kl) \end{aligned} \tag{5.49}$$

which, as for M_{HFC}, differs from the condition for perfect transmission (5.45). In the strong impurity limit $J' \to 0$ where terms of order J'^2 can be neglected the resonance condition becomes

$$0 = \cos^2(k)\sin(kl) + O\left(J'\right)^2$$

which corresponds to the same limit of the perfect transmission equation (5.45). We can thus conclude that the analogy to optical cavities only holds in the limit of strong impurities where perfect transmission and the resonance pole coincide. Staying in this limit, we may take this analogy further by considering the wavefunction of an incoming particle at resonance.

We know that the light field in an optical resonator builds up as incoming light is in resonance with the resonance frequency which is also called cavity mode [40]. Let us check whether the same effect is observed for the wavefunction of an incoming particle in M_{HFD} and M_{HFC}. The wavefunction of a particle in M_{HFD} is calculated using the running wave ansatz (5.15) with its coefficients being determined using equations (5.18) to (5.22). For M_{HFC} an analogue ansatz (5.39) with coefficients (5.40) has been derived.

The complex resonance momenta can be determined by inserting $k = \mathrm{Re}(k) + i\,\mathrm{Im}(k)$ into the

resonance condition (5.48) to obtain a non-linear system of two equations

$$\begin{aligned} 0 &= V'\left(1 \pm e^{-\operatorname{Im}(k)l}\cos\big(\operatorname{Re}(k)l\big)\right) + 2\operatorname{Im}(k) \\ 0 &= \pm V' e^{-\operatorname{Im}(k)l}\sin\big(\operatorname{Re}(k)l\big) - 2\operatorname{Re}(k) \end{aligned} \tag{5.50}$$

which can be solved numerically. Note that the imaginary part of the momentum gives the resonance width [41].

In order to give an example to compare perfect transmission momenta and resonances in M_{HFD} and M_{HFC}, let us choose an impurity strength of $V' = 10.5$ corresponding to $J' = 0.4$ where according to figure 5.9 the transmission spectrum shows very sharp peaks of perfect transmission. At this impurity strength, the system of equations (5.50) for M_{HFC} is solved by

$$\begin{aligned} k &= 0.3082936 - i0.0001689 \quad \text{(first resonance)} \\ \text{and} \quad k &= 0.616625 - i0.000672 \quad \text{(second resonance).} \end{aligned}$$

the first and second resonance. These momenta barely differ from the momenta of perfect transmission

$$\begin{aligned} k &= 0.3082937 \quad \text{(first transmission peak)} \\ \text{and} \quad k &= 0.616627 \quad \text{(second transmission peak).} \end{aligned}$$

and their small imaginary parts demonstrate the narrow width of the resonances.

As for M_{HFC}, one obtains a system of long equations for $\operatorname{Re}(k)$ and $\operatorname{Im}(k)$ from the resonance condition of M_{HFD} (5.49). Numerical solutions for $J' = 0.4$ are given by

$$\begin{aligned} k &= 0.3081047 - i0.0001796 \quad \text{(first resonance)} \\ \text{and} \quad k &= 0.614942 - i0.000872 \quad \text{(second resonance).} \end{aligned}$$

Comparing with the momenta of perfect transmission from equation (5.45)

$$\begin{aligned} k &= 0.308105 \quad \text{(first transmission peak)} \\ \text{and} \quad k &= 0.614945 \quad \text{(second transmission peak).} \end{aligned}$$

shows again how perfect transmission appears close to resonance in the limit of strong impurities. Since M_{HFD} is the model of interest, we pick its momenta of resonance and compare the probability densities at those two momenta with those of M_{HFC} in the left figure 5.10.

Just as for an optical cavity, for resonant momenta, we observe a strongly enhanced particle density in between the impurities. We can call this a confined mode. The wavefunctions are normalized to an incoming amplitude 1 which, due to interference with the reflected wave, leads to a maximal probability density of 4 on the left of the impurities. The density on the right of the impurities only stems from the transmitted wave and is therefore 1 for perfect transmission and between 0 and 1 otherwise. As apparent from the figure, for an impurity hopping amplitude of $J' = 0.4$, the probability density of the first confined mode is enhanced by a factor 1000. Due to a slight mismatch of resonant momenta in M_{HFD} and M_{HFC}, the enhancement in M_{HFC} is less pronounced but still features a probability density of 600 and a transmission probability of about 0.5.

The probability densities of the second resonance mode are less enhanced than the ones of the first

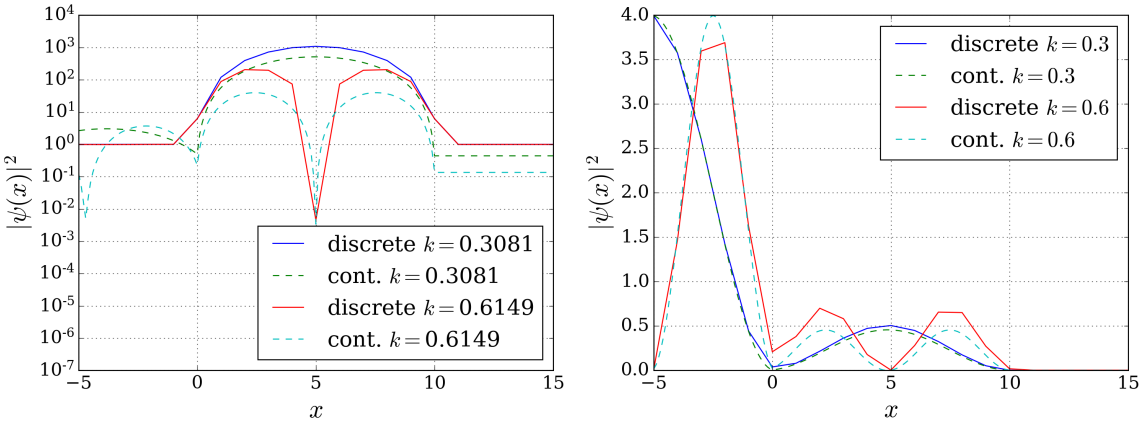

Figure 5.10: Probability densities of an incoming particle from the left for M_{HFD} with $J' = 0.4$ and M_{HFC} with $V' = 10.5$. In both models, the impurities are at a distance of $l = 10$. Left: The incoming particle's momenta are at resonance with the system's length scale. To illustrate the strong density enhancement, it is plotted in a semi-logarithmic scale. Right: Slightly off-resonant momenta with linear scale for the probability density. The normalization of all wavefunctions is chosen such that the incoming wave from the left has an amplitude of 1. In the right figure the reflection amplitude does not vanish which leads to interference at $x < 0$. The result is an oscillating pattern in the probability density of which only the first oscillation is visible in the plot.

resonances. This is not observed for optical resonators where the internal light field does not depend on the order of the mode [40]. The reduction of the enhancement is due to the finite effective hopping amplitude $J' = 0.4$ and vanishes for $J' \to 0$. Furthermore, the probability densities of the second resonance mode in M_{HFD} and M_{HFC} differ more than those of the first mode. This is again due to the fact that the continuous and discrete model match best for small momenta.

The right figure 5.10 illustrates the probability densities of particles with slightly off-resonant momenta, just outside the sharp resonance peaks of figure 5.9, scattering off the two impurities. At the given distance between the impurities, particles with these momenta do not interfere constructively anymore, yielding a reduced instead of an enhanced density in between the impurities. Therefore and due to the strong impurities, the particle transmission tends to zero.

We have thus learned that the sharp transmission peaks appearing for strong impurities in M_{HFD} and M_{HFC} are accompanied by a strong enhancement of the wavefunction between the impurities. This can be explained by the fact that in the limit of strong impurities, the momenta of perfect transmission are equal to the momenta of resonance, which is why the systems behave analogously to optical resonators.

A second approach to further substantiate this observation is the analysis of the discrete model's eigensystem. To check whether the system's eigenvalue spectrum and its eigenstates hint towards confined modes, which are observed with a running wave ansatz, we need to diagonalize the high frequency effective Hamiltonian (5.7). This can be achieved numerically by choosing a finite system size $N \gg l$, with the two impurities positioned symmetrically around the center, and by representing

the Hamiltonian as a matrix:

$$\hat{H}_{\text{eff}} = \begin{pmatrix}
\ddots & J & & & & & & & & & & & \\
J & 0 & J & & & & & & & & & & \\
 & J & 0 & J_{1,\text{eff}} & & & & & & & & & \\
 & & J_{1,\text{eff}} & 0 & J_{1,\text{eff}} & & & & & & & & \\
 & & & J_{1,\text{eff}} & 0 & J & & & & & & & \\
 & & & & J & 0 & J & & & & & & \\
 & & & & & \ddots & \ddots & \ddots & & & & & \\
 & & & & & & J & 0 & J & & & & \\
 & & & & & & & J & 0 & J_{2,\text{eff}} & & & \\
 & & & & & & & & J_{2,\text{eff}} & 0 & J_{2,\text{eff}} & & \\
 & & & & & & & & & J_{2,\text{eff}} & 0 & J & \\
 & & & & & & & & & & J & 0 & J \\
 & & & & & & & & & & & J & \ddots
\end{pmatrix} \begin{matrix} \\ \\ \\ \\ \\ \\ \\ \\ \\ \\ \\ \\ \\ \end{matrix} \begin{matrix} \\ \\ \\ \\ j = 0 \\ \\ \\ \\ \\ j = l \\ \\ \\ \\ \end{matrix} \tag{5.51}$$

For a finite system size, this matrix can be diagonalized numerically to determine its eigensystem. An example with $N = 61$ is given in figure 5.11, where N is odd such that for even $l = 10$ the impurities sit symmetrically around the chain's center.

The lower right plot in figure 5.11 demonstrates that most eigenstates are degenerate since they feature a symmetric and an anti-symmetric solution. Therefore, their probability distribution is equal and only one of the two degenerate eigenstates is visible in the probability density plots. There are some non-degenerate exceptions, such as eigenvalues 5, 10, 12, 17, 24. Comparing eigenvalues and eigenfunctions, it becomes clear, that these non-degenerate eigenvalues correspond to confined eigenfunctions that show an increased density in between the impurities. The fact that these confined eigenfunctions are non-degenerate assures that they are unique to the system and appear independently of the choice of basis states. In figure 5.12, the first ten eigenfunctions are plotted whose eigenvalues are non-degenerate and which feature a confined density.

Comparing the eigenenergies of these confined eigenfunctions to the system's transmission spectrum in figure 5.9, one easily sees that these states with non-degenerate eigenenergies appear exactly at the energies of perfect transmission and equally (in the limit of strong impurities) at the resonant modes. To complete the comparison of eigenstates and resonant modes, in appendix B.3, the wavefunctions in the different models (M_{HFD}, M_{HFC}, position-dependent mass system) are compared at resonance. This appendix again shows that especially for small momenta M_{HFC} provides a very good description of M_{HFD}.

We have thus learned that the transmission peaks appearing at strong impurities correspond to resonances of the system analogous to the resonance modes of an optical resonator. The confined wavefunctions at these resonances are observed for running waves in infinite systems and appear as confined eigenstates in finite systems. However, we already learned that the correspondence of perfect transmission and resonance does not hold when leaving the limit of strong impurities (compare e. g. equations (5.46) and (5.48)). The next section is therefore dedicated to explaining how resonances, perfect transmission peaks and confined modes change when decreasing the impurity strength.

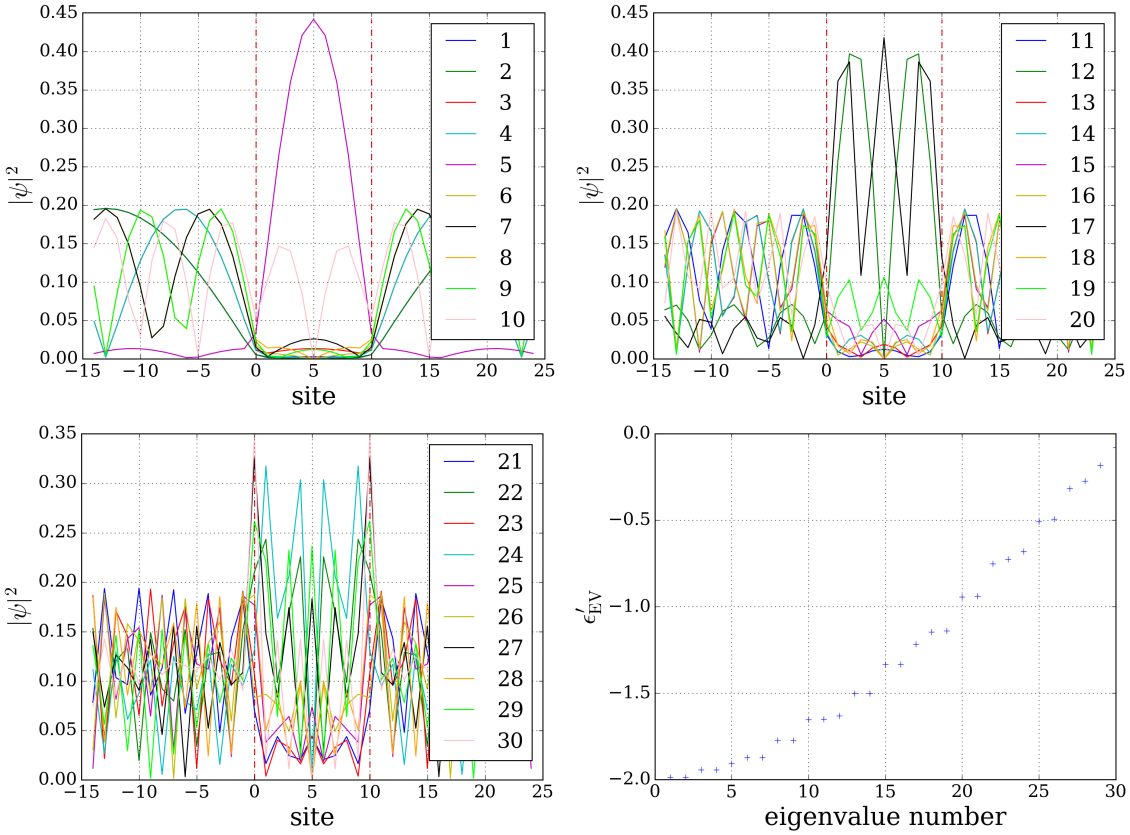

Figure 5.11: Upper left, upper right and lower left: Probability density of the first 30 eigenfunctions of the Hamiltonian (5.7) with $J' = 0.4$, $l = 10$ and a finite system size of $N = 61$ sites. The dashed lines indicate the impurities. Lower right: The corresponding energy eigenvalues ϵ'_{EV}.

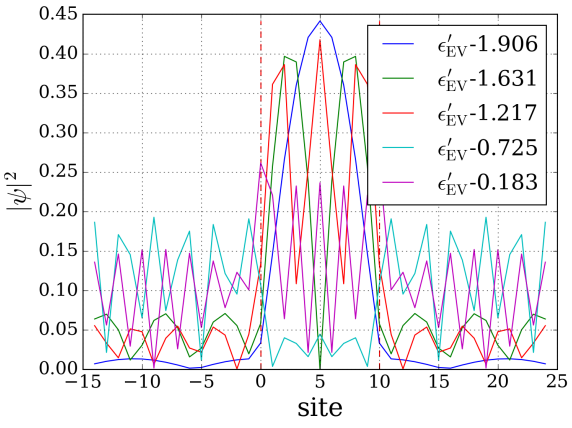

Figure 5.12: Confined eigenfunctions with their corresponding eigenvalues for M_{HFD} with $J' = 0.5$, $l = 10$ and a finite system size of $N = 61$.

5.3.4 Change in transmission spectra for weaker impurities

In the previous section 5.3.3, we learned that the sharp transmission peaks at strong impurities correspond to resonances analogue to the modes of an optical resonator at $k = n\frac{\pi}{l}$. Just as in an optical cavity, these resonances are accompanied by a strong wavefunction enhancement in between impurities. However, we also found that the analogy to optical resonators does not hold any more at weaker impurities where the transmission maxima do not occur at resonance any more (compare the perfect transmission conditions (5.46) and (5.45) to the resonance conditions (5.48) and (5.49)). In this section, let us discuss why the transmission peaks shift when the impurity strength decreases and how this affects the confined wavefunction modes observed at strong impurities.

According to figure 5.7, the transmission peaks get broader and shift towards lower momenta as the impurity strength decreases (that is, as J' shifts from 0 towards 1). The overall transmission probability increases which fits the intuitive picture that the impurities represent smaller barriers which are more likely to be tunneled through. This is again illustrated in figure 5.13 where the transmission spectra of M_{HFD} and M_{HFC} are plotted for a few small impurity strengths.

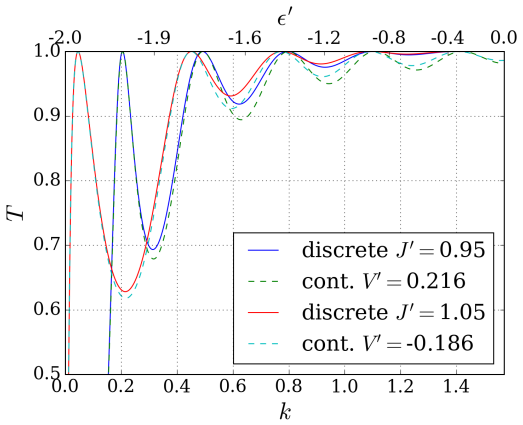

Figure 5.13: Comparison of the transmission spectra of M_{HFD} and M_{HFC} with $l = 10$ and weak impurities with $J' = 0.95$ ($V' = 0.216$) and $J' = 1.05$ ($V' = -0.186$). Note that in contrast to previous transmission spectra, in order to better observe differences in the spectra, the T-axis ranges only from 0.5 to 1 .

Taylor-expanding the transmission probabilities (5.23) and (5.41) in this limit of small impurity strength ($J' \to 1$, $V' \to 0$) yields:

$$\begin{aligned} \text{discrete model:} \quad & T_{J'\to 1} = 1 - \frac{16\cos^2(kl)}{\tan^2(k)}(J'-1)^2 + O(J'-1)^3 \\ \text{and continuous model:} \quad & T_{V'\to 0} = 1 - \frac{\cos^2(kl)}{k^2}\left(V'\right)^2 + O\left(V'\right)^3. \end{aligned} \tag{5.52}$$

One finds these two expressions to match in the low momentum limit when $\tan(k) \approx k$ for $V' = \pm 4(J'-1)$. Writing $J' = 1+\delta$ and neglecting terms $O(\delta)^2$, one can show that this fits to the weak

impurity limit of relation (5.42):

$$V' = -2\left(\frac{J'^2-1}{J'^2}\right) = -\frac{2+4\delta-2+O(\delta)^2}{1+O(\delta)} \approx -4\delta = -4(J'-1).$$

In this approximation, the transmission spectrum is dominated by two contributions: The term $1/\tan^2(k)$, and $1/k^2$ in M_{HFC} correspondingly, generally prohibits a finite transmission probability for $k \to 0$ but vanishes rapidly for finite momenta. The term $\cos^2(kl)$, in turn, produces oscillations in the transmission spectrum with perfect transmission at $k = (n+\frac{1}{2})\frac{\pi}{l}$ and minimal transmission for $k = \frac{n\pi}{l}$. Comparing the weak impurity transmission of equations (5.52) to the strong impurity transmission (5.47), one observes a shift in the perfect transmission momenta by $\frac{\pi}{2l}$. This shift is equally observed in the transmission heat maps of figure 5.16 and in the perfect transmission conditions (5.46) and (5.45).

In section 5.3.3, we found that in the limit of strong impurities, perfect transmission occurs at resonance. Let us determine how the shift in perfect transmission for weaker impurities is related to such resonances. For this, due to its simplicity, let us first consider M_{HFC} introduced in section 5.2.2 which was found to reproduce the low momentum results of M_{HFD}. In the left figure 5.14, the momenta of perfect transmission computed from equation (5.46) are compared to the real and imaginary part of the momenta of resonance given by equation (5.48) (or more explicitly the momenta solving the non-linear system of equations (5.50)) . The same comparison is drawn for M_{HFD} in the right figure 5.14. Here, perfect transmission has been determined from equation (5.45) whereas the complex momenta solving the discrete resonance condition (5.49) are determined numerically.

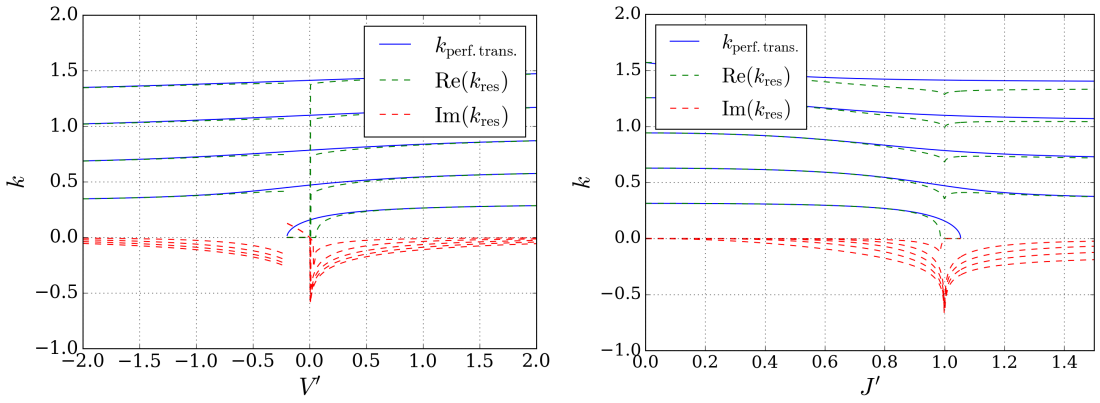

Figure 5.14: Momentum of perfect transmission and real and imaginary part of the numerically determined resonance momentum as a function of the impurity strength with impurities at a distance $l = 10$. For those cases where $k_{\mathrm{res}} = 0$ the numerical calculation failed. Left: M_{HFC}. Right: M_{HFD}.

Both figures demonstrate how the resonances shift further away from the momenta of perfect transmission, the weaker the impurity gets. At the same time, the imaginary parts of the resonant momenta increase creating broader resonances. For M_{HFC}, these two effects have already been quantified and discussed in [38]. The increasing imaginary parts, in turn, explain the difference between perfect transmission and resonance because the broader the resonances get, the more of them contribute to the transmission probability at a given momentum [42]. For very broad resonances,

as they occur at weak impurities, perfect transmission is present when the contributions of multiple neighboring resonances interfere constructively which generally is not equal to the pole momentum of the transmission amplitude. Figure (5.49) therefore suggests that the momenta of perfect transmission shift as result of two overlapping effects: Firstly, the resonant momenta shift when the impurity strength changes. Secondly, the resonances get broader, such that multiple ones contribute to a single peak of perfect transmission.

Regarding figure 5.14, one should note that for some weak impurity strengths a vanishing resonant momentum $k_{\text{res}} = 0$ is found. This result indicates a failure of the numerical computation due to a poor initial guess when the real part of the resonant momentum differs significantly from the momentum of perfect transmission.

Let us now analyze how the confined wavefunction modes that were observed at strong impurities (section 5.3.3) change when the impurity strength is decreased. It is especially interesting whether the wavefunction in between impurities is maximally enhanced at resonance or at perfect transmission. This question is answered in figure 5.15 where wavefunctions tunneling through weak impurities are plotted at (the real parts of) resonant momenta and at momenta of perfect transmission.

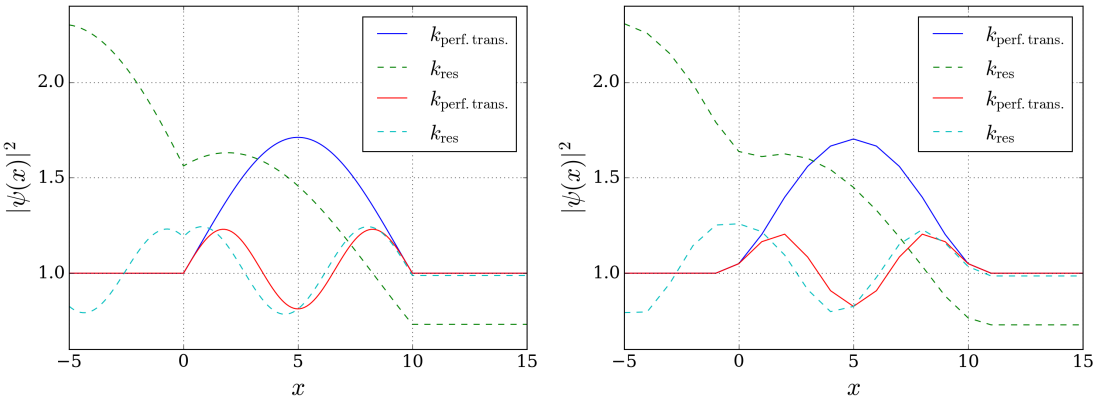

Figure 5.15: Wavefunctions incoming with momenta of perfect transmission or at resonance, scattered off two impurities at a distance of $l = 10$. Left: M_{HFC} with $V' = 0.05$. Right: M_{HFC} with $J' = 0.9759$ which according to relation (5.42) corresponds to $V' = 0.05$.

According to this figure, maximal wavefunction enhancement occurs at the momenta of perfect transmission instead of the resonant momenta. This suggests that outside of the limit of strong impurities is not justified to identify the confined wavefunction modes as resonances. In turn, each mode contains contributions of multiple broad resonances.

To measure the wavefunction enhancement for different impurity strengths, in figure 5.16, the mean probability density in between impurities is plotted as a function of incoming momentum and impurity strength. The red lines indicating momenta of perfect transmission support the observation of maximal enhancement at perfect transmission whereas the kinks delineated by the resonant momenta in figure 5.14 do not show in figure 5.16. Only for small momenta and weak impurities, maximal wavefunction enhancement appears at a different momentum than perfect transmission. This can be explained with the appearance of shallow bound states for $V' < 0$ and $J' > 1$ which boost transmission but not the confined scattering mode. This effect will be further explained in section 5.3.5.

Let us finalize the discussion of confined modes and perfect transmission by considering a finite

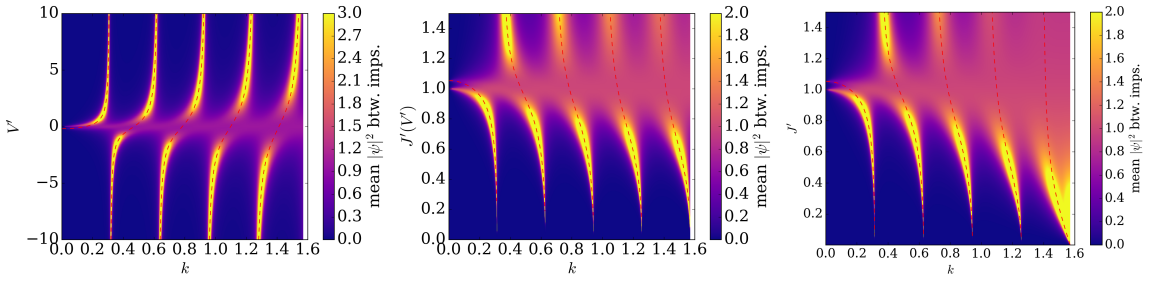

Figure 5.16: Mean probability density in between impurities as a function of incoming momentum and impurity strength. The red curve indicates momenta of perfect transmission. Left: M_{HFC}. Center: M_{HFC} where the peak height V' is translated into a hopping amplitude J' according to relation (5.42). Right: M_{HFD}.

system. In section 5.3.3, we found that finite systems with strong impurities show confined eigenstates whose eigenenergies are equal to the resonant energies of the infinite system and thus, in this limit, also equal to the energies of perfect transmission. The left figure 5.17 illustrates how these eigenenergies of the confined eigenstates change when decreasing the impurity strength. As for infinite systems we observe the confined eigenstates appearing at energies of perfect transmission and not at resonance.

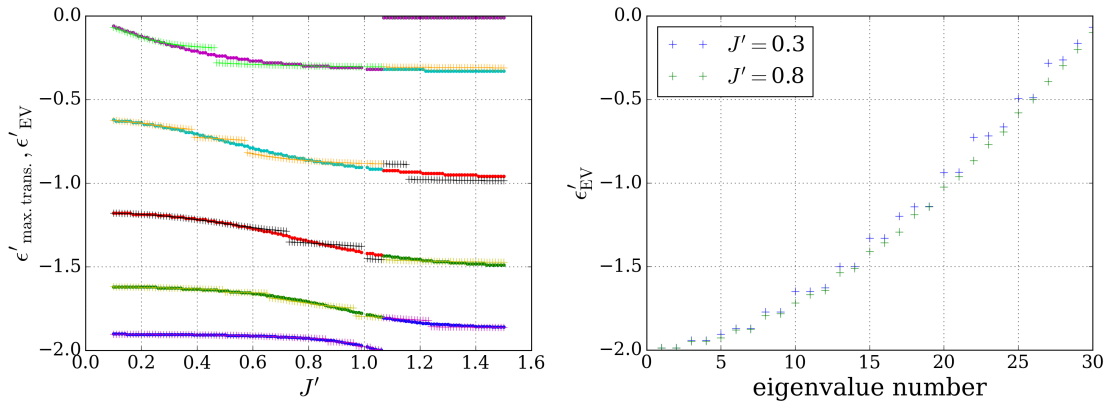

Figure 5.17: Left: Comparison of the energies of maximal transmission in an infinite system with $l = 10$ (solid) to the eigenenergies of confined eigenstates of the corresponding finite system with $N = 61$ (dotted) as a function of the impurity strength J'. Right: Comparison of eigenvalue spectra at two different impurity strengths. Since the transmission peaks get wider at weaker impurity strength, more non-degenerate eigenvalues contribute.

By taking a closer look at figure 5.17, a step-like structure in the eigenenergy plots can be identified which is not present in the plots of perfect transmission momenta. These steps are a finite size effect and can be explained by considering how the eigenvalue spectrum changes with decreasing impurity strength. Whereas the energies of perfect transmission shift with increasing J', the other eigenvalues do not shift. Instead, starting at high energies, they become non-degenerate which indicates that multiple eigenstates contribute to the same transmission peak (see right figure 5.17). If a perfect transmission eigenvalue approaches a background eigenvalue, instead of passing by, the two eigenstates hybridize and share the confined density. When further increasing J' the previous background eigenvalue becomes the one corresponding to the confined state and vice versa. By choosing larger system sizes, the entire eigenvalue spectrum becomes denser which is why more of these avoided crossings take

place. At the same time, the energy difference between neighboring eigenvalues decreases which is why the steps become less apparent and vanish for infinite systems where the spectrum becomes continuous.

In this section, we have learned how perfect transmission at weak impurities results from constructive interference of multiple broad resonances. Enhanced wavefunction modes at perfect transmission are observed for scattered running waves and as confined eigenstates of finite systems. According to figure 5.16, the only case where the correspondence between perfect transmission and enhanced wavefunction does not hold, is the combination of weak impurities and low momenta. In the following section, this effect is explained by the appearance of bound states which can furthermore create the unique feature of perfect transmission at zero momentum.

5.3.5 Bound states and threshold anomaly

In the previous sections, we analyzed the resonance spectra of M_{HFD} and M_{HFC}. We showed how these resonances create confined wavefunctions and perfect transmission in the limit of strong impurities (section 5.3.3) and for weaker impurities (section 5.3.4). After investigating the systems' resonances, it is a natural next step to determine their bound state spectrum. As promised before, with our findings we will be able to explain the effect of perfect transmission at zero momentum.

Let us begin with computing the bound state spectrum of M_{HFC} of section 5.2.2 and then proceed analogously with M_{HFD} derived in section 5.1.1. Without any previous knowledge, bound states could be determined by making an ansatz similar to the plane wave ansatz (5.39) but without the incoming plane wave and with replacing the plane wave terms $e^{\pm ikx}$ by exponentially decaying terms $e^{\mp\kappa x}$ characteristic for bound states. This corresponds to the replacement $k \mapsto i\kappa$ After solving the Schrödinger equation by demanding continuity of the wavefunction and determining the jump in its first derivative, we would expect to obtain a condition for one or multiple discrete bound states.

As we have already solved the scattering wave ansatz (5.39) without specifying whether k is real or complex, we can use the fact that, for any system, bound states correspond to resonances with purely imaginary momentum [41]. This fact was used in reference [38] to derive bound states of the double delta potential and we will, in the following, summarize their findings. Inserting $k = i\kappa$, $\kappa \in \mathbb{R}$ into the transmission amplitude (5.40), one finds poles at

$$V_1' V_2' e^{-2\kappa l} = \left(2\kappa + V_1'\right)\left(2\kappa + V_2'\right). \tag{5.53}$$

Using the findings of [38], let us comment on this transcendent equation, which can only be solved numerically or graphically, before turning to the case of symmetric impurities. For this, consider equation (5.53) in the following three cases:

1. $V_1', V_2' \geq 0$: For any combination of potential heights, one finds $LHS > RHS$ which is why equation (5.53) does not have any solutions. There are no bound states present.

2. $V_1' > 0, V_2' < 0$ or vice versa: A single bound state exists if

$$\frac{\mathrm{d}}{\mathrm{d}\kappa} LHS\Big|_{\kappa=0} > \frac{\mathrm{d}}{\mathrm{d}\kappa} RHS\Big|_{\kappa=0} \qquad \Rightarrow \qquad l > \frac{-(V_1' + V_2')}{V_1' V_2'}.$$

   Otherwise there is no bound state present.

3. $V_1', V_2' < 0$: *LHS* and *RHS* always intersect once, so there is always at least a single bound state present. The second one appears when $l > \frac{-(V_1'+V_2')}{V_1'V_2'}$ which is calculated as in the previous case.

For symmetric impurities $V_1' = V_2' \equiv V'$, the bound state condition (5.53) reduces to

$$\pm V' e^{-\kappa l} = 2\kappa + V' \tag{5.54}$$

which features either two bound states if

$$V' < -2/l. \tag{5.55}$$

or a single bound state if $-2/l < V' < 0$.

Before analyzing the bound states' influence on the transport characteristics of M_{HFC}, let us derive the bound state criterion for M_{HFD} in an analogous fashion. For this, consider again the poles of the transmission amplitude calculated from equations (5.18) to (5.22) for purely imaginary momentum $k = i\kappa$. One obtains the bound state condition

$$\frac{\left(e^{2\kappa}-1\right)\left(J'_{1,\mathrm{eff}}\right)^2}{1+e^{2\kappa}-2\left(J'_{1,\mathrm{eff}}\right)^2} = \frac{-1+e^{2\kappa(l+1)}+\left(J'_{2,\mathrm{eff}}\right)^2+e^{2\kappa l}\left(1-2\left(J'_{2,\mathrm{eff}}\right)^2\right)+e^{2\kappa}\left(-1+\left(J'_{2,\mathrm{eff}}\right)^2\right)}{\left(1+e^{2\kappa}\right)\left(-1+\left(J'_{2,\mathrm{eff}}\right)^2\right)}$$

which can be rewritten as

$$\begin{aligned} 0 =& x^{l+2} - x^{l+1} 2\left(\left(J'_{1,\mathrm{eff}}\right)^2+\left(J'_{2,\mathrm{eff}}\right)^2-1\right)+x^l\left(2\left(J'_{1,\mathrm{eff}}\right)^2-1\right)\left(2\left(J'_{2,\mathrm{eff}}\right)^2-1\right) \\ & -\left(\left(J'_{1,\mathrm{eff}}\right)^2-1\right)\left(\left(J'_{2,\mathrm{eff}}\right)^2-1\right)\left(x^2+x+1\right) \\ \text{with} \quad x =& e^{2\kappa} \end{aligned} \tag{5.56}$$

Similarly to M_{HFC}, the number of bound states solving this condition depends on the sign of the impurity strengths $J'_{i,\mathrm{eff}}$: For $J'_{1,\mathrm{eff}}, J'_{2,\mathrm{eff}} \leq 1$ the system does not exhibit any bound state. In case one of the effective hopping amplitudes exceeds 1, a single bound state appears if the condition

$$2l > \frac{\left(J'_{1,\mathrm{eff}}\right)^2}{\left(J'_{1,\mathrm{eff}}\right)^2-1} + \frac{\left(J'_{2,\mathrm{eff}}\right)^2}{\left(J'_{2,\mathrm{eff}}\right)^2-1} \tag{5.57}$$

is fulfilled. And if both effective hopping amplitudes exceed 1, one bound state is always present and the second one exists if the same condition (5.57) is satisfied. For symmetric impurities with $J' > 1$ the bound state condition (5.56) becomes

$$\begin{aligned} 0 =& J'^4\left(-2e^{2\kappa l}+e^{2\kappa}+1\right) \\ & + J'^2 e^{\kappa}\cosh(\kappa)\left(\left(J'^2-2\right)e^{2\kappa}-J'^2+4e^{2\kappa l}-2\right) \\ & - 4e^{\kappa(l+2)}\cosh^2(\kappa)\sinh(\kappa l) \end{aligned} \tag{5.58}$$

which always features a single bound state for $J' > 1$ and the second one appears if

$$J' > \sqrt{\frac{l}{l-1}}. \tag{5.59}$$

It is reassuring to note that this condition for a second bound in M_{HFD} can be transformed into to the corresponding condition for M_{HFC} (5.55) by means of the previously found relation (5.42) between the two models.

It is known that the shallower a bound states lies (the closer to free energies) the more it affects low momentum scattering[1]. Before relating the presence of bound states for $V' < 0$ and $J' > 1$ to the transmission characteristics of these models, it is therefore interesting to determine their energy as a function of impurity strength. For this, the imaginary parts of the bound state momenta κ are determined by solving relations (5.54) and (5.58) and plotted in figure 5.18. One nicely sees how the first bound states appear as soon as $V' < 0$ and $J' > 1$. According to equations (5.55) and (5.59), for impurities at a distance of $l = 10$, the second bound states then appear at impurity strengths of $V' = -0.2$ and $J' = \sqrt{10/9} \approx 1.054$ which fits to the appearance of the upper bound states in figure 5.18.

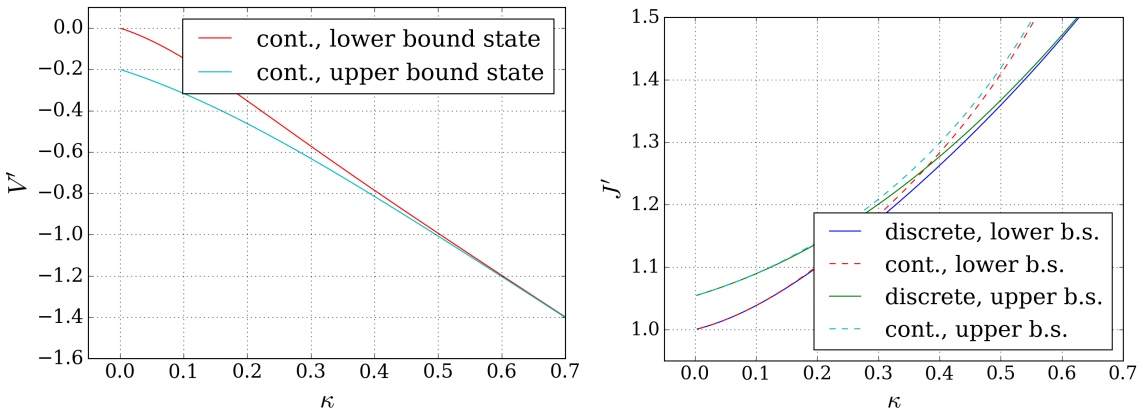

Figure 5.18: Imaginary parts κ of bound states for systems with impurities at a distance of $l = 10$. Left: M_{HFC}. Right: Comparison between M_{HFD} and M_{HFC} where the peak height V' is converted into an effective hopping amplitude J' according to relation (5.42).

Figure 5.19 relates the presence of bound states to the systems' transmission spectrum. Here, the bound states' energies are calculated from the momenta's imaginary parts according to

$$\text{discrete model:} \quad \epsilon'_{\mathrm{bs}} = \frac{\epsilon_{\mathrm{bs}}}{J} = -2\cos(k) = -2\cosh(\kappa)$$
$$\text{and continuous model:} \quad \epsilon'_{\mathrm{bs}} = \frac{2m}{\hbar^2}\epsilon_{\mathrm{bs}} = k^2 = -\kappa^2.$$

Figure 5.19 demonstrates that shallow bound states increase transmission at low momenta since they influence scattering like a nearby resonance. According to equations (5.46) and (5.45), this effect can even lead to perfect transmission at zero momentum occurring exactly when the second bound state

[1] For a thorough discussion of how shallow bound states affect scattering see [44].

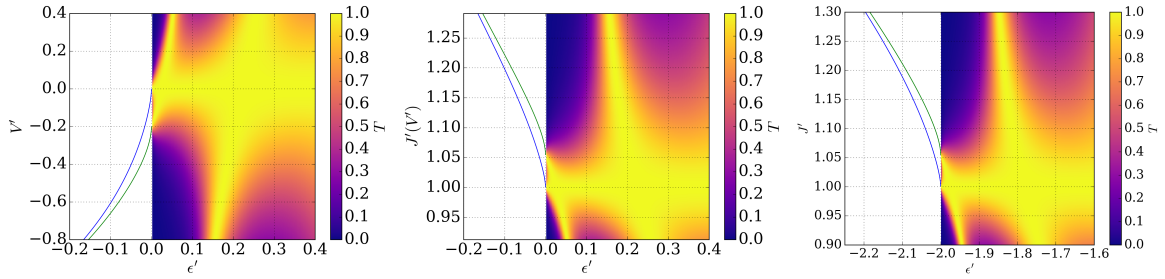

Figure 5.19: Transmission probability for energies of propagating particles in the continuum and bound state energies for systems with impurities at a distance of $l = 10$. Left: M_{HFC}. Center: M_{HFC} where the peak height V' is translated into a hopping amplitude J' according to relation (5.42). Right: M_{HFD}.

appears. This effect, which has been named 'threshold anomaly' [36] and is thoroughly discussed in reference [37], is a critical phenomenon as illustrated in figure 5.20.

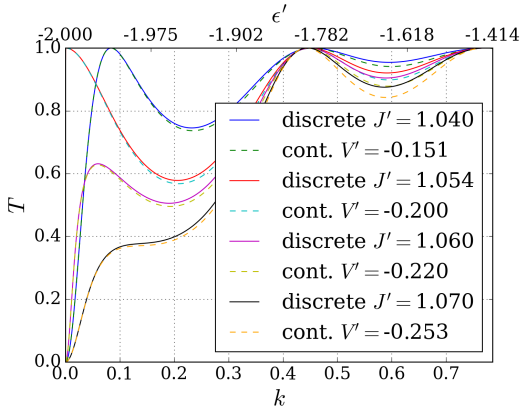

Figure 5.20: Transmission spectrum of M_{HFD} and M_{HFC} around $J' = \sqrt{10/9}$ (corresponding to $V' = -0.2$) where, according to equation (5.55), for $l = 10$ the second bound state appears.

It is apparent that transmission at $k = 0$ is perfect at exactly $V' = -\frac{2}{l}$ but completely vanishes otherwise. Physically, this phenomenon can be interpreted by considering a wave packet with no average kinetic energy placed on one side of the impurities. The very low momentum components are then nearly perfectly transmitted through the impurities and scattering on the impurities simply appears as wave packet spreading [38].

Let us close this section by verifying whether bound states that are found for infinite systems are present in finite systems as well. For this, proceed as in the previous sections 5.3.3 and 5.3.4 by diagonalizing the Hamiltonian of a finite system that could feature bound states. In figure 5.21, the lowest eigenstates of such a system are plotted for different impurity strengths.

Indeed, the bound states that were identified in infinite systems are retrieved for finite discrete systems. In this context, figure 5.21 nicely illustrates the appearance of a second bound state around the effective hopping amplitude given by condition (5.59). When increasing this hopping amplitude from $J' = 1.06$ to 1.07, the curvature of the second lowest eigenstates changes and the delocalized state turns into a localized one. The finite system size only shifts the appearance of this second bound state

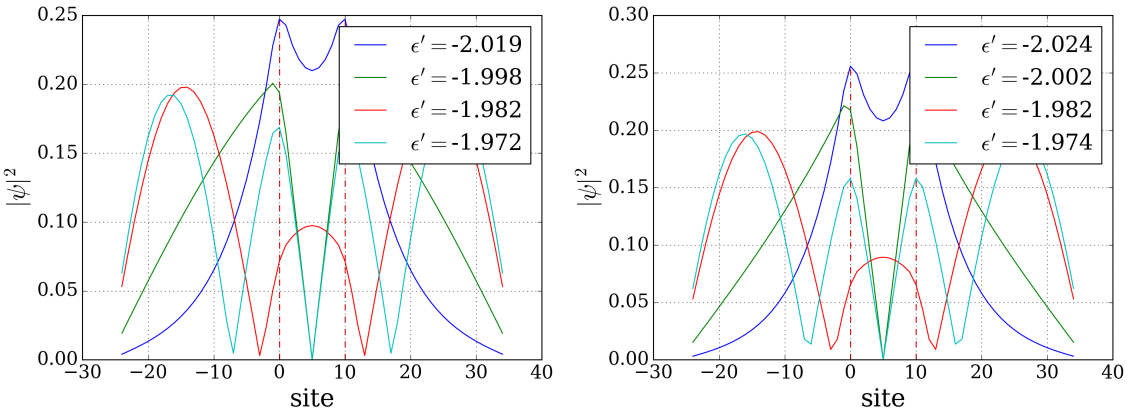

Figure 5.21: Probability densities and eigenenergies of the lowest eigenstates of a finite system with $N = 61$ and $l = 10$ for $J' = 1.06$ (left) and $J' = 1.07$ (right) where a second bound state appears. In a corresponding infinite system, the second bound state would appear at $J' = 1.054$ (equation (5.59))
`2_driven_sites_high_freq_eigvals_eigvecs`

to slightly larger J' compared to infinite systems. We can deduce that for some value $1.06 < J' < 1.07$ there exists a state with $\epsilon' = -2$ which is then responsible for perfect transmission at zero momentum.

A quantitative relation between bound states in finite and infinite systems can be drawn by fitting the function

$$|\phi\rangle = \sum_j \phi_j c_j^+ |0\rangle \qquad \text{with} \qquad \phi_j = A_1 e^{-\kappa|j|} + A_2 e^{-\kappa|j-l|} \tag{5.60}$$

to the decaying parts of finite systems bound states. Note that this ansatz is only valid to describe the wavefunction outside of the impurities. To describe the full wavefunction, analogously to the running wave ansatz (5.15), one would require five terms. The resulting decay parameters κ_{fit} can then be compared to the theoretical values from the dispersion relation (5.16)

$$\epsilon' = 2\cos(k) = 2\cosh(\kappa) \qquad \Rightarrow \qquad \kappa_{\text{theo}} = \operatorname{arcosh}\left(\frac{|\epsilon'|}{2}\right).$$

This comparison is drawn in figure 5.22. It is also checked for asymmetric impurites $J_1 \neq J_2$ in section 5.4 (figure 5.28). For the symmetric case, we observe a good match between fitted and theoretical decay constant. The slight deviations, than can also be identified in the plots, can be ascribed to the limited fitting region due to the finite system size of 61 sites.

With these considerations, we can close the discussion of how bound states affect transmission in M_{HFD} and M_{HFC}. We found that shallow bound states lead to an increase in the transmission probability at small momenta since bound states, just as nearby resonances, enhance the wavefunction in between impurities.

Thus, all characteristic transmission features appearing in systems with symmetric impurities could be explained by means of the continuous analogue system M_{HFC} derived in section 5.2. We found that for strong impurities the high frequency effective model M_{HFD} behaves analogous to an optical resonator: Perfect transmission appears at resonance when confined wavefunction modes show up. As

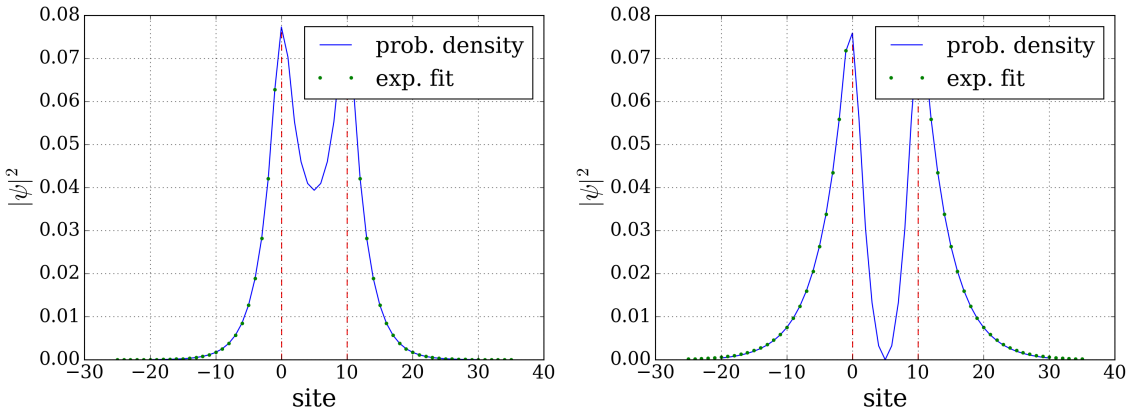

Figure 5.22: Probability density of the two bound states of a finite system with $N = 61$ and $l = 10$ for $J' = 1.1$ and bound state ansatz (5.60) fitted to the wavefunction. Left: $\epsilon' = -2.04$, $\kappa_{\text{theo.}} = 0.199715$ with fit parameters $\kappa_{\text{fit}} = 0.199778(15)$, $A_1 = A_2 = 0.269355(14)$. Right: $\epsilon' = -2.015$, $\kappa_{\text{theo.}} = 0.12363$ with fit parameters $\kappa_{\text{fit}} = 0.12537(25)$, $A_1 = -A_2 = -0.42515(28)$.

the impurity strength decreases, the resonances become broader and resonant momenta shift. As a consequence, each peak of perfect transmission becomes wider and shows contributions of multiple resonances. As soon as the effective hopping amplitudes at the impurities exceed the value of the bulk hopping amplitude, bound states emerge which enhance low momentum transmission. At the transition from a delocalized state to a second bound state, perfect transmission at zero momentum arises as a threshold anomaly. After having discussed mainly systems with symmetric impurities, the following section analyzes how these transport characteristics change for systems with asymmetric impurities. This will finalize the discussion of the high frequency limit.

5.4 Asymmetric impurities

In the previous sections, the high frequency model of a tight binding chain with two AC driven impurities M_{HFD} was derived and its transport characteristics were explained by means of an analogue continuous model M_{HFC}. Even though all calculations were performed for arbitrary impurities, all results were presented for symmetric impurities to limit the number of free parameters and thus find a physical explanation of characteristic transport and wavefunction features. In this section, we will review how these features that were discussed in detail in section 5.3 change when impurities become asymmetric. To this end, we will keep the structure of the previous section to first discuss resonances appearing at strong impurities, then turn towards the changes in spectrum for weaker impurities and finally discuss the effects of bound states.

In section 5.3.3, we found that for strong impurities, very sharp resonances at momenta $k = n\frac{\pi}{l}$ lead to perfect transmission and strongly confined wavefunction modes. To analyze how these properties change for asymmetric impurities, in figure 5.23 the transmission spectra of M_{HFD} are plotted for $J_{1,\mathrm{eff}} = 0.5$ and different values of $J_{2,\mathrm{eff}}$.

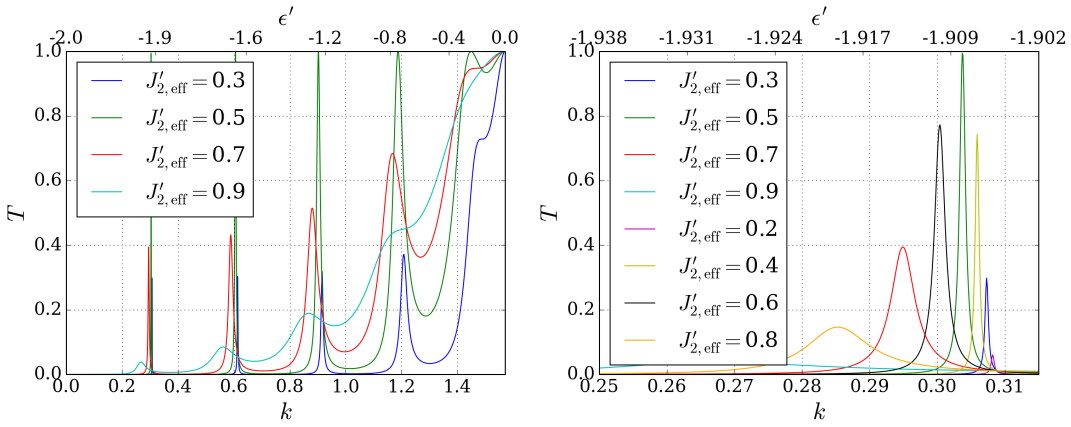

Figure 5.23: Transmission spectra of M_{HFD} for asymmetric impurities at a distance of $l = 10$ and with $J_{1,\mathrm{eff}} = 0.5$. The right panel is a zoom into the first transmission maximum of the left panel.

First of all, it seems like perfect transmission is only observed for the case of symmetric impurities. This observation can be tested by means of M_{HFC}. Here, perfect transmission occurs as a root of the reflection amplitude (5.40) which is determined from the transcendent equation

$$2k\left(1+\frac{V_2'}{V_1'}e^{2ikl}\right)+iV_2'\left(1-e^{2ikl}\right)=0. \tag{5.61}$$

For symmetric impurities, this turns into equation (5.46) where the complex terms form the tangent function permitting real momentum solutions. As was previously found in reference [38], the only real momentum solution to equation (5.61) with asymmetric impurities is given by the antisymmetric case $V_1' = -V_2'$ where the brackets vanish at momenta $k = n\frac{\pi}{l}$. Away from the case of symmetric or asymmetric impurities, the imaginary parts of the momenta solving the perfect transmission equation (5.61) increase for larger differences between the impurity strengths $\left|V_1' - |V_2'|\right|$.

Let us check whether perfect transmission for asymmetric impurities can likewise be observed in

M_{HFD}. One finds that, just as in M_{HFC}, the discrete system's reflection amplitude which is determined from equations (5.18) to (5.22) has roots at $k = n\frac{\pi}{l}$ if the effective hopping amplitudes fulfill the condition

$$J'^2_{1,\mathrm{eff}} + J'^2_{2,\mathrm{eff}} - 2J'^2_{1,\mathrm{eff}}J'^2_{2,\mathrm{eff}} = 0 \qquad \Rightarrow \qquad J'_{i,\mathrm{eff}} = \frac{J'_{j,\mathrm{eff}}}{\sqrt{2J'^2_{j,\mathrm{eff}} - 1}} \quad \text{with} \quad i \neq j. \tag{5.62}$$

which is plotted in the left figure 5.24.

In contrast to M_{HFC}, perfect transmission with asymmetric impurities cannot be achieved for any impurity strength on the first impurity. In fact, if one of the impurities has $J'_{i,\mathrm{eff}} \leq \frac{1}{\sqrt{2}}$, perfect transmission is only possible for symmetric impurities. This artifact can be understood by considering the mapping (5.42) for $V'_i \leftrightarrow J'_{i,\mathrm{eff}}$ which was found in section 5.2.3. According to this relation, hopping amplitudes $J'_{i,\mathrm{eff}} < \frac{1}{\sqrt{2}}$, where perfect transmission with asymmetric impurities is impossible, correspond to continuous impurity strengths $V'_i > 2$. For such impurity strengths, perfect transmission in M_{HFC} is observed for $V'_j = -V'_i < 0$ which, according to relation (5.42), do not have a discrete counterpart. Thus, the set $\{V'_1, V'_2\}$ cannot be mapped to a set of hopping amplitudes $\{J'_{1,\mathrm{eff}}, J'_{2,\mathrm{eff}}\}$.

Transmission spectra for selected combinations of asymmetric impurities with perfect transmission are compared in the right figure 5.24. Indeed, all plotted spectra show perfect transmission at the same momenta $k = n\frac{\pi}{l}$.

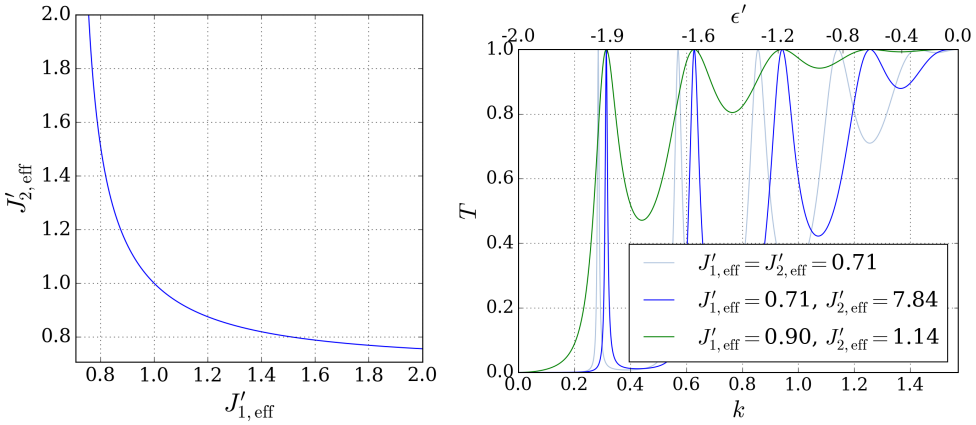

Figure 5.24: Left: Combinations of asymmetric effective hopping amplitudes where according to relation (5.62) the model M_{HFD} shows perfect transmission at momenta $k = n\frac{\pi}{l}$. Right: Transmission spectra for selected combinations of $J'_{1,\mathrm{eff}}$ and $J'_{2,\mathrm{eff}}$ that feature perfect transmission.

Considering again figure 5.23, one can furthermore observe that for the case of one strong and one weak impurity the envelope function is more pronounced compared to the single transmission peaks. To quantify this change in spectrum, let us Taylor-expand the transmission probability (5.23) for $J'_{1,\mathrm{eff}} \to 0$ and $J'_{2,\mathrm{eff}} \to 1$:

$$T_{J'_{1,\mathrm{eff}}\to 0, J'_{2,\mathrm{eff}}\to 1} = \left(1 - \frac{4\sin(2kl)}{\tan(k)}(1 - J'_{2,\mathrm{eff}})\right)\tan^2(k)(J'_{1,\mathrm{eff}})^4 + O\left(J'_{1,\mathrm{eff}}\right)^6 + O\left(J'_{2,\mathrm{eff}} - 1\right)^2. \tag{5.63}$$

This approximation is compared to the exact transmission in figure 5.25. It is interesting to note

that the fine structure of the spectrum is a result of the weak impurity $J'_{2,\text{eff}}$ and for vanishing $J'_{2,\text{eff}}$, one obtains the transmission through a single impurity without any fine structure. Furthermore, the transmission maxima lie at $k = \left(n + \frac{3}{4}\right)\frac{\pi}{l}$ which is right in between the two limiting cases of two weak impurities and two strong ones.

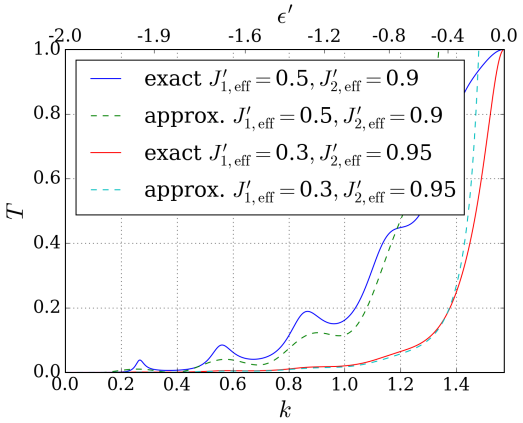

Figure 5.25: Transmission spectra of M_{HFD} with one weak and one strong impurity. The exact result calculated with equation (5.23) is compared to the Taylor expansion (5.63).

Let us now analyze the influence of asymmetric impurities on the wavefunction enhancement at perfect transmission by again considering the analogy to optical resonators which is valid for strong impurities: If the first mirror of an optical cavity is fixed, the internal mode intensity is maximized by choosing the second mirror's reflectivity as large as possible [40]. Note that this increases the mode field but decreases transmission. In turn, for a fixed second mirror, mode intensity is maximal when the first mirror is symmetric to the second one which also maximizes transmission.

The left figure 5.26 checks whether the analogy between the optical resonator modes and the wavefunction enhancement in M_{HFD} with small impurity hopping amplitudes holds for for asymmetric impurities. Here, either $J'_{1,\text{eff}} = 0.4$ or $J'_{2,\text{eff}} = 0.4$ is fixed and the averaged probability density in between impurities at the first momentum of maximal transmission is plotted as a function of the other effective hopping amplitude that is varied. Indeed, the analogy to optical resonators holds: When the first impurity strength is fixed, the wavefunction enhancement is maximal for maximal second impurity strength, whereas, for fixed second impurity strength, maximal wavefunction enhancement is observed for symmetric impurities. Note that in the case of fixed $J'_{1,\text{eff}}$, even though choosing $J'_{2,\text{eff}}$ as small as possible enhances the probability density in between impurities, maximal transmission is still achieved for the symmetric case of $J'_{1,\text{eff}} = J'_{2,\text{eff}}$.

The right figure 5.26 illustrates how the wavefunction enhancement for asymmetric hopping amplitudes changes when one of the impurities is fixed to a low impurity strength. The most important difference between strong and weak impurity regimes lies in the fact that for fixed first impurity strength, maximal mode enhancement does not occur at the strongest second impurity but reaches a plateau below some finite second impurity strength. In fact, this behavior corresponds to the observation made earlier when discussing the transmission spectrum in the limiting case of one strong and one weak impurity (equation (5.63)). We found that the weaker impurity creates the single transmission peaks and, therefore, in this limiting case dominates the wavefunction enhancement. Thus, when

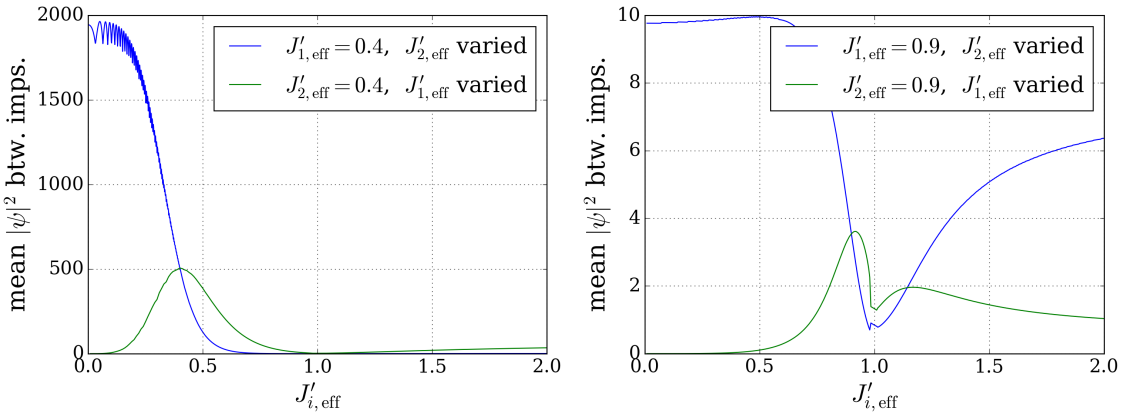

Figure 5.26: Mean probability density in between impurities at the lowest momenta of maximal transmission in the high frequency discrete system with $l = 10$. In each plot one of the effective hopping amplitudes $J'_{1,\mathrm{eff}}$ and $J_{2,\mathrm{eff}}$ is fixed while the other one is varied. Left: One strong impurity $J'_{j,\mathrm{eff}} = 0.4$. The oscillations at small $J'_{i,\mathrm{eff}}$ are of numerical nature. Right: One weak impurity $J'_{j,\mathrm{eff}} = 0.9$.

$J'_{1,\mathrm{eff}} \to 1$, variations in the strong impurity $J'_{2,\mathrm{eff}}$ barely influence wavefunction enhancement.

Secondly, it is worth noticing that the two plots of the right figure 5.26 intersect at those combinations of $J'_{1,\mathrm{eff}}$ and $J'_{2,\mathrm{eff}}$ where perfect transmission occurs. For symmetric impurities, this intersection is trivial and observed for any impurity strength (see left figure 5.26). The only non-trivial case where wavefunction enhancement does not change when interchanging $J'_{1,\mathrm{eff}}$ and $J'_{2,\mathrm{eff}}$ is therefore given by the perfect transmission condition for asymmetric impurities (5.62).

Let us finally check whether the threshold anomaly discussed in section 5.3.5 survives for asymmetric impurities by regarding figure 5.27. In the left panel, equation (5.56) is used to find combinations of $J'_{1,\mathrm{eff}}$ and $J'_{2,\mathrm{eff}}$ where a second bound state is just appearing which again leads to the threshold anomaly of finite transmission probability at zero momentum. However, in contrast to symmetric systems, perfect transmission is not reached. Instead one finds that the zero momentum transmission is lower, the more the impurity strengths differ. The same effect was already observed for other transmission maxima (see figure 5.23) .

The right panel of figure 5.27 illustrates that as for symmetric impurities, the threshold anomaly stays a critical phenomenon for asymmetric impurities. To show this, $J_{1,\mathrm{eff}} = 1.09$ is fixed where according to equation (5.57) a second bound state appears at $\epsilon'_{\mathrm{bs}} = -2$ for $J'_{2,\mathrm{eff}} = 1.039$. The figure illustrates that only at this critical value of $J'_{2,\mathrm{eff}}$ the transmission probability at zero momentum does not vanish.

As a last comment on bound states, it is interesting to note that, as soon as the impurities differ significantly from each other, each bound state is localized to one of the two impurities. In this case, the energetically lower state is the one which is localized to the stronger impurity. This effect even shows for the bound states at slightly differing impurities of $J'_1 = 1.1$ and $J'_2 = 1.11$ depicted in figure 5.28. Here, similarly to figure 5.22, fitted decay constants are compared to the theoretical values demonstrating good agreement between the results computed for finite and infinite systems.

With this, we can close the discussion of asymmetric impurities and of the high frequency limit. In this section, we found that all transport characteristics that were discussed for symmetric impurities in section 5.3 are retrieved for systems with asymmetric impurities. Even though perfect transmission

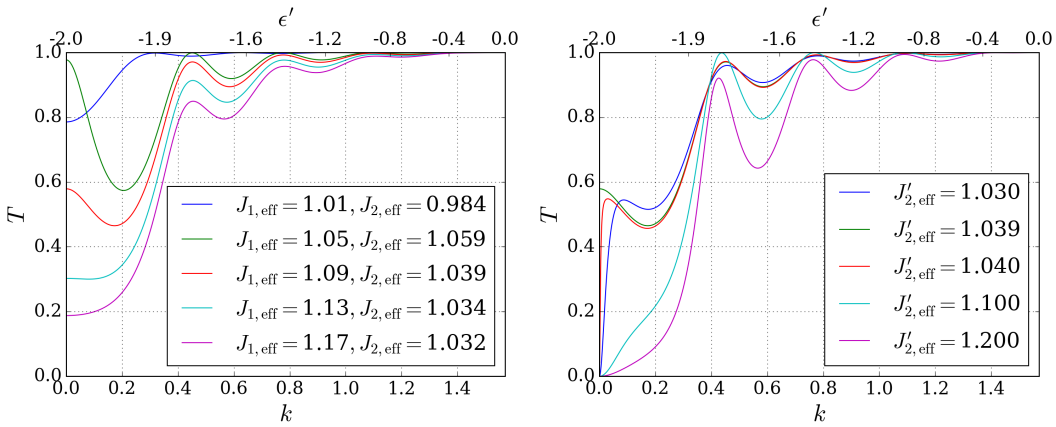

Figure 5.27: Transmission spectra of M_{HFD} for asymmetric impurities at a distance of $l = 10$. Left: Systems with combinations of $J'_{1,\mathrm{eff}}$ and $J'_{2,\mathrm{eff}}$ where according to equation (5.56) a bound state is present exactly at $\epsilon'_{\mathrm{bs}} = -2$. Right: $J'_{1,\mathrm{eff}} = 1.09$ is fixed and $J_{2,\mathrm{eff}}$ is varied which demonstrates the criticality of the threshold anomaly.

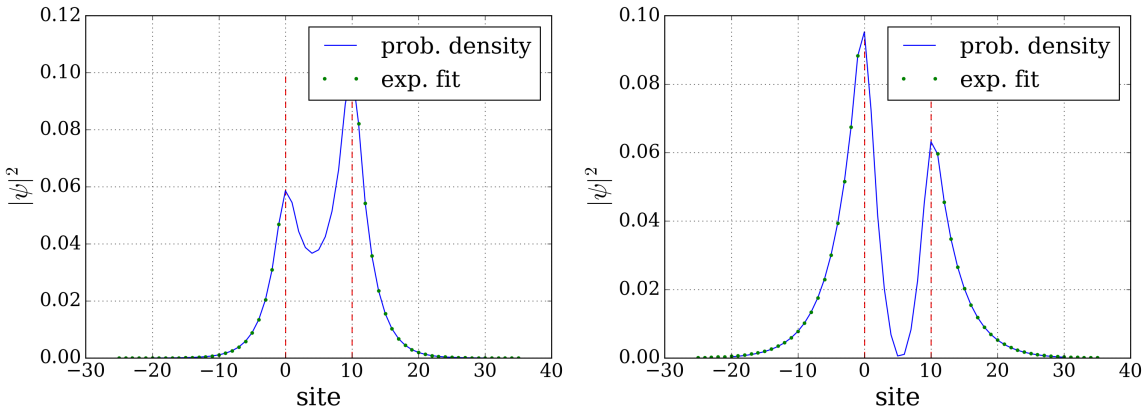

Figure 5.28: Probability density of the two bound states of a finite system with $N = 61$ and $l = 10$ for $J'_1 = 1.1$, $J'_2 = 1.11$ and bound state ansatz (5.60) fitted to the wavefunction. Left: $\epsilon' = -2.043$, $\kappa_{\mathrm{theo.}} = 0.207730$ with fit parameters $\kappa_{\mathrm{fit}} = 0.207774(11)$, $A_1 = 0.225780(11)$, $A_2 = 0.324463(10)$. Right: $\epsilon' = -2.018$, $\kappa_{\mathrm{theo.}} = 0.13350$ with fit parameters $\kappa_{\mathrm{fit}} = 0.13466(18)$, $A_1 = 0.44270(17)$, $A_2 = -0.39461(21)$.

only occurs in symmetric systems, sharp transmission resonances are still observed for slightly asymmetric impurities. The more the impurities differ, the weaker these transmission peaks get and the more the transmission spectrum is dominated by the strong impurity.

Furthermore, confined wavefunction modes are still observed at the momenta of maximal transmission. Just as in an optical cavity, the mode density is enhanced by maximizing the strength of the second impurity. And even though perfect transmission at zero momentum only occurs in symmetric systems, the threshold anomaly of non-vanishing transmission survives for asymmetric impurities.

After this thorough discussion of the time-independent high frequency limit of the tight binding chain with two driven impurities, it is time to consider lower frequencies. In the following section we will thus return to the original time-dependent model, which was introduced in section 2 and its treatment in Floquet theory discussed in section 4. We will analyze which of the transport characteristics that are found at high frequencies exist in the full Floquet picture and whether new properties emerge.

CHAPTER 6

Solution of the Floquet picture

In chapter 2, the model of a tight binding chain with two driven impurities was introduced. In the previous chapter 5, we derived that for large driving frequencies this model reduces to a time-independent effective model M_{HFD} with effective hopping amplitudes to the impurities. The transmission spectrum of this effective model was analyzed thoroughly by drawing comparisons to an analogue continuous high frequency model M_{HFC} with impurities represented by static delta potentials. Several interesting transmission characteristics like perfect transmission, resonances and threshold anomalies were discussed.

It is now time to leave the high frequency limit and return to the Floquet picture of the original model which was derived in section 4. To observe how the high frequency characteristics change at finite frequencies and which new features emerge, we will proceed as follows: In the first section 6.1, a time-dependent analogue continuous model will be derived by combining the ideas of sections 4 and 5.2. Then, to get a first insight into the multichannel transport problem, in section 6.2, previous results on single impurity systems with discrete and continuous position parameters are summarized. Finally, in section 6.3, transport in the Floquet picture wi two driven impurities is discussed.

6.1 Time-dependent continuous model

In chapter 5, we found that transmission through the static high frequency effective model M_{HFD} shows similar characteristics as an analogue continuous model M_{HFC} consisting of two delta potentials at the positions of the impurities. Due to more compact expressions (compare the transmission probabilities (5.23) and (5.41)), M_{HFC} was used to explain features of M_{HFD}. With the same motivation, it is, therefore, instructive to derive a continuous model that is analogue to the time-dependent discrete model described by the Hamiltonian (2.3). We will use the shorthand notations M_{TDD} for the time-dependent discrete model and M_{TDC} for its analogue continuous model. After the derivation of M_{TDC} in subsection 6.1.1, a method to determine transport in this model is calculated in subsection 6.1.2 and compared to the discrete model's method in subsection 6.1.3

6.1.1 Derivation of the time-dependent analogue continuous model

To derive a continuous model M_{TDC} for the discrete model's Hamiltonian (2.3), let us first only consider the static tight binding term (2.1):

$$\hat{H}_{\text{tb}} = -J \sum_{j\neq -1,0,l-1,l} (\hat{c}_j^\dagger \hat{c}_{j+1} + \hat{c}_{j+1}^\dagger \hat{c}_j) - J_1 \sum_{j=-1,0} (\hat{c}_j^\dagger \hat{c}_{j+1} + \hat{c}_{j+1}^\dagger \hat{c}_j) - J_2 \sum_{j=l-1,l} (\hat{c}_j^\dagger \hat{c}_{j+1} + \hat{c}_{j+1}^\dagger \hat{c}_j).$$

In section 5.1.1, we found that the high frequency effective Hamiltonian (5.7) has the same form as this tight binding Hamiltonian. Only the hopping amplitudes to the impurities were rescaled by the zeroth Bessel function leading to effective hopping amplitudes $J_i \to J_{i,\text{eff}}$ (equation (5.8)). In section 5.2, it was then argued that the continuous analogue model M_{HFC} to the high frequency effective model M_{HFD} is given by equation (5.36):

$$V'_{\text{double delta pot.}}(x) = V_1' \delta(x) + V_2' \delta(x-l)$$

where all physical quantities were rescaled according to equation (5.30). Equation (5.42) gives the relation between M_{HFC} and M_{HFD}

$$V_i' = 2\left(\frac{1}{J_{i,\text{eff}}'^2} - 1\right) \qquad \Leftrightarrow \qquad J'_{i,\text{eff}} = \frac{1}{\sqrt{V_i'/2+1}}$$

with the dimensionless effective hopping amplitudes $J'_{i,\text{eff}} = J_{i,\text{eff}}/J$ (equation (5.17)).

Due to the same form of the Hamiltonians (2.1) and (5.7), the continuous analogue potentials must have the same form as well. This results a potential that is analogue to the tight binding Hamiltonian (2.1)

$$V_{\text{tb, analogue}}(x) = v_1 \delta(x) + v_2 \delta(x-l) \tag{6.1}$$

with the relation to the tight binding Hamiltonian

$$v_i' = 2\left(\frac{1}{J_i'^2} - 1\right) \qquad \Leftrightarrow \qquad J_i' = \frac{1}{\sqrt{v_i'/2+1}}$$

where the hopping amplitudes J_i' are rescaled according to equation (4.12). v_i' describe the rescaled impurity strengths

$$v_i' \equiv \frac{2m}{\hbar^2} v_i.$$

where the v_i parameterize the impurity strengths of M_{TDC}.

Having found a continuous correspondence to the static part of the discrete Hamiltonian, let us now turn to the driving Hamiltonian of equation (2.2):

$$\hat{H}_{\mathrm{drive}}(t) = -\mu_1 \cos(\omega t)\hat{c}_0^\dagger \hat{c}_0 - \mu_2 \cos\big(\omega t + \phi\big)\hat{c}_l^\dagger \hat{c}_l.$$

In contrast to the tight binding Hamiltonian (2.1), this driving Hamiltonian does not contain any kinetic term $\hat{c}_j^\dagger \hat{c}_{j+1}$ and is therefore straight forward to translate into a continuous expression:

$$V_{\mathrm{drive,\ analogue}}(t) = \gamma_1 \cos(\omega t)\delta(x) + \gamma_2 \cos\big(\omega t + \phi\big)\delta(x - l). \tag{6.2}$$

Here, the γ_i represent the driving amplitudes and are, therefore, expected to be proportional to the chemical potentials of strengths μ_i in the discrete system. This proportionality will be quantified in the following section when deriving transport in M_{TDC}.

Containing the static potential (6.1) and the driven one (6.2), the total Hamiltonian of M_{TDC} is given by

$$\begin{aligned}\hat{H}_{\mathrm{cont.\ analogue}}(t) &= -\frac{\hbar^2}{2m}\frac{\partial^2}{\partial x^2} + V_{\mathrm{tb,\ analogue}}(x) + V_{\mathrm{drive,\ analogue}}(x) \\ &= -\frac{\hbar^2}{2m}\frac{\partial^2}{\partial x^2} + \big(v_1 + \gamma_1 \cos(\omega t)\big)\,\delta(x) + \Big(v_2 + \gamma_2 \cos\big(\omega t + \phi\big)\Big)\,\delta(x - l)\end{aligned} \tag{6.3}$$

where m is the mass of the particle considered. In the following section, transport through this system will be calculated using the Floquet formalism.

6.1.2 Particle transport in the time-dependent analogue continuous model

After having derived a Hamiltonian (6.3) with continuous position parameter which is analogous to the Hamiltonian (2.3) with discrete position, transmission through the analogue continuous model M_{TDC} can be calculated in a similar fashion as described for M_{TDD} in section 4.2. The following calculation is analogue to the one in reference [45], where transport through a continuous system with (a combination of a static and an oscillating) single barrier has been calculated.

In this case, we are first required to determine the Fourier modes of the Hamiltonian (6.3) H_n for the Fourier expansion

$$\hat{H}(t) = \sum_{n=-\infty}^{\infty} H_n e^{in\omega t}.$$

One finds that the zeroth mode is given by the time-independent terms

$$\hat{H}_0 = -\frac{\hbar^2}{2m}\frac{\partial^2}{\partial x^2} + V_{\text{tb, analogue}}(x) \tag{6.4}$$

and the time-dependent drive potential (6.2) can be rewritten in terms of Fourier modes:

$$\begin{aligned} V_{\text{drive, analogue}}(x) &= \gamma_1 \cos(\omega t)\delta(x) + \gamma_2 \cos\big(\omega t + \phi\big)\delta(x-l) \\ &= \frac{\gamma_1}{2}\left(e^{i\omega t} + e^{-i\omega t}\right)\delta(x) + \frac{\gamma_2}{2}\left(e^{i\omega t + i\phi} + e^{-i\omega t - i\phi}\right)\delta(x-l) \\ &= e^{-i\omega t}\underbrace{\left(\frac{\gamma_1}{2}\delta(x) + \frac{\gamma_2}{2}e^{-i\phi}\delta(x-l)\right)}_{\hat{H}_{-1}} + e^{i\omega t}\underbrace{\left(\frac{\gamma_1}{2}\delta(x) + \frac{\gamma_2}{2}e^{i\phi}\delta(x-l)\right)}_{\hat{H}_1} \\ &= e^{-i\omega t}\hat{H}_{-1} + e^{i\omega t}\hat{H}_1 . \end{aligned} \tag{6.5}$$

As discussed in section 3, inserting a time-periodic Hamiltonian into the Schrödinger equation leads to the Floquet equation (3.8) (and rewritten equation (3.10)). By means of the block structure of the quasienergy operator given in equation (3.13), the Floquet equation of M_{TDC} can be written in the same fashion as for the discrete system, given by equation (4.3)

$$H_0\left|u_n\right\rangle + H_1\left|u_{n+1}\right\rangle + H_{-1}\left|u_{n-1}\right\rangle = E_n\left|u_n\right\rangle \tag{6.6}$$

with the quasienergies $E + n\hbar\omega$. Here, $\left|u_n\right\rangle$ are the Floquet modes introduced in equation (3.2). Since both, M_{TDC} and M_{TDD}, are driven with a single frequency component, the quasienergy operators take the same tridiagonal block structure. The resulting quasienergy operator is equivalent to a Hamiltonian which describes multiple one-dimensional systems coupling to each other at the positions of the impurities (see figure 6.1 which is analogue to figure 4.1 for M_{TDD}). According to equation (6.5), the coupling strength between two systems is given by $\gamma_i/2$. In the following sections 6.2 and 6.3, we will discuss how this picture helps in understanding the system's transport properties. Inserting the Hamiltonian's Fourier components given by equations (6.4) and (6.5), the Floquet equation (6.6) becomes

$$\begin{aligned} -\frac{\hbar^2}{2m}\frac{\partial^2}{\partial x^2}\left|u_n\right\rangle + \left[v_1\left|u_n\right\rangle + \frac{\gamma_1}{2}\left(\left|u_{n+1}\right\rangle + \left|u_{n-1}\right\rangle\right)\right]\delta(x) \\ + \left[v_2\left|u_n\right\rangle + \frac{\gamma_2}{2}\left(e^{-i\phi}\left|u_{n+1}\right\rangle + e^{i\phi}\left|u_{n-1}\right\rangle\right)\right]\delta(x-l) = E_n\left|u_n\right\rangle . \end{aligned} \tag{6.7}$$

Having derived the Floquet equation governing the Floquet modes of M_{TDC}, transport through this system can be determined by making an analogue ansatz to the one in section 4.2. We consider an incoming plane wave with momentum k_0 from the left in the zeroth channel and scattered plane waves

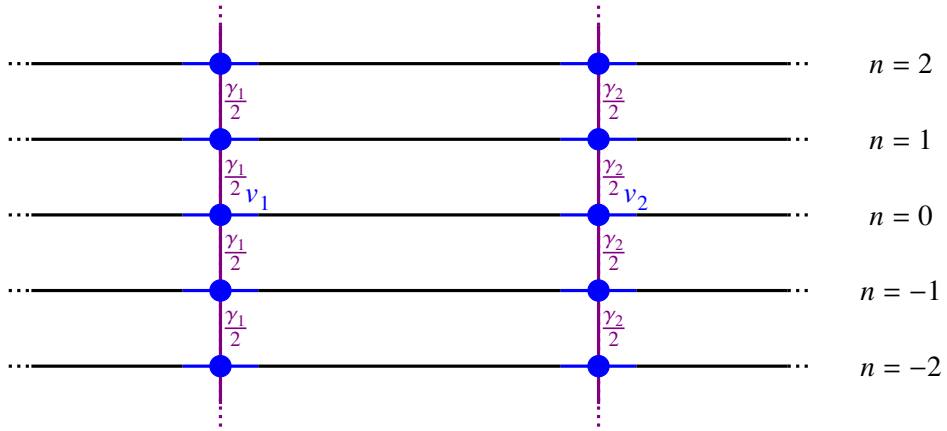

Figure 6.1: The quasienergy operator of M_{TDC}, which has the form of equation (4.3), is equivalent to a Hamiltonian describing multiple one-dimensional systems labeled by a Fourier index n with static potentials at two positions which we call impurities. At these impurities the chains are coupled to each other.

on all channels

$$\left|u_n\right\rangle = \begin{cases} \delta_{0,n} e^{ik_n x} + r_n e^{-ik_n x} & x \leq 0 \\ t'_n e^{ik_n x} + r'_n e^{-ik_n x} & 0 < x \leq l \\ t_n e^{ik_n x} & l < x \end{cases}. \tag{6.8}$$

The energy of the incoming wave is given by the non-relativistic dispersion relation

$$E = \frac{\hbar^2 k_0^2}{2m} \tag{6.9}$$

and according to equation (3.6) the quasienergy in channel n is given by

$$E_n = E + n\hbar\omega \equiv \frac{\hbar^2 k_n^2}{2m}. \tag{6.10}$$

Demanding continuity of the wavefunction at $x = 0$ and $x = l$, one obtains the relations

$$\eta_n \equiv \delta_{n,0} + r_n = t'_n + r'_n \qquad \text{and} \qquad t_n = t'_n + r'_n e^{-i2k_n l} \tag{6.11}$$

where η_n is the wavefunction at $x = 0$ in channel n. The analogue wavefunction at site 0 in the discrete system was called E_n (equation (4.16)) but is named differently here to prevent confusion with the energy in channel n. Two more relations between the wavefunction amplitudes are obtained by integrating the Floquet equation (6.7) over infinitesimally small regions around $x = 0$ and $x = l$ to

calculate the discontinuities of the wavefunctions' first derivatives:

$$\frac{i\hbar^2}{m}k_n\left[t_n' - r_n' - \delta_{n,0} + r_n\right] = \gamma_1\left(\eta_{n-1} + \eta_{n+1}\right) + 2v_1\eta_n \tag{6.12}$$

$$\text{and}\quad \frac{i\hbar^2}{m}k_n e^{ik_n l}\left[t_n - t_n' + r_n' e^{-i2k_n l}\right] = \gamma_2\left(t_{n-1}e^{ik_{n-1}l}e^{-i\phi} + t_{n+1}e^{ik_{n+1}l}e^{i\phi}\right) + 2v_2 t_n e^{ik_n l}. \tag{6.13}$$

Inserting relations (6.11) into equation (6.12) leads to

$$2ir_n' = 2i\left[\eta_n - \delta_{n,0}\right] - \frac{m}{\hbar^2 k_n}\left(\gamma_1\left[\eta_{n-1} + \eta_{n+1}\right] + 2v_1\eta_n\right). \tag{6.14}$$

Finally, inserting equations (6.11) and (6.14) into equation (6.13) gives a recurrence relation equivalent to equation (4.19) of the form

$$\beta_n = \sum_{k=-2}^{2}\alpha_k^{(n)}\eta_{n+k} \tag{6.15}$$

with coefficients

$$\begin{aligned}
\beta_0 =& -2ik_0k_1k_{-1}\left[k_0e^{-ik_0l} + v_2'\sin\left(k_0l\right)\right]\\
\beta_{\pm1} =& -i\gamma_2'e^{\mp i\phi}k_0k_{\pm1}k_{\pm2}\sin\left(k_0l\right)\\
\beta_n =& 0 \quad \text{else}\\
\alpha_0^{(n)} =& k_nk_{n+1}k_{n-1}e^{-ik_nl}\left[-2ik_n + v_1' + v_2'\right]\\
&+ k_{n+1}k_{n-1}v_1'v_2'\sin\left(k_nl\right)\\
&+ \frac{\gamma_1'\gamma_2'}{4}k_n\left[e^{-i\phi}k_{n+1}\sin\left(k_{n-1}l\right) + e^{i\phi}k_{n-1}\sin\left(k_{n+1}l\right)\right]\\
\alpha_{\pm1}^{(n)} =& k_nk_{n+1}k_{n-1}\left[\frac{\gamma_1'}{2}e^{-ik_nl} + \frac{\gamma_2'}{2}e^{\pm i\phi}e^{-ik_n\pm1l}\right]\\
&+ k_{n\mp1}\left[\frac{\gamma_1'}{2}v_2'k_{n\pm1}\sin\left(k_nl\right) + \frac{\gamma_2'}{2}v_1'e^{\pm i\phi}k_n\sin\left(k_{n\pm1}l\right)\right]\\
\alpha_{\pm2}^{(n)} =& \frac{\gamma_1'\gamma_2'}{4}e^{\pm i\phi}k_nk_{n\mp1}\sin\left(k_{n\pm1}l\right)
\end{aligned} \tag{6.16}$$

where the driving amplitudes were rescaled in the same manner as all quantities in continuous systems with dimension energy or energy × length:

$$\gamma_i' = \frac{2m}{\hbar^2}\gamma_i.$$

As discussed in section 5.2.1 below equation (5.36), since we work with momenta in units of the inverse discrete lattice spacing a (equation (5.24)), all lengths are scaled in untis of a. Therefore, quantities of dimension energy × length are scaled in the same fashion as quantities of dimension energy. In order to recover dimensional quantities, a multiplication with the according powers of a is

required.

The recurrence relation (6.15) can be written as a system of linear equations

$$\underbrace{\begin{pmatrix} & \ddots & & & & & \\ \alpha_{-2}^{(-1)} & \alpha_{-1}^{(-1)} & \alpha_{0}^{(-1)} & \alpha_{1}^{(-1)} & \alpha_{2}^{(-1)} & & \\ & \alpha_{-2}^{(0)} & \alpha_{-1}^{(0)} & \alpha_{0}^{(0)} & \alpha_{1}^{(0)} & \alpha_{2}^{(0)} & \\ & & \alpha_{-2}^{(1)} & \alpha_{-1}^{(1)} & \alpha_{0}^{(1)} & \alpha_{1}^{(1)} & \alpha_{2}^{(1)} \\ & & & & & \ddots & \end{pmatrix}}_{A} \underbrace{\begin{pmatrix} \vdots \\ \eta_{-1} \\ \eta_0 \\ \eta_1 \\ \vdots \end{pmatrix}}_{\vec{\eta}} = \underbrace{\begin{pmatrix} \vdots \\ \beta_{-1} \\ \beta_0 \\ \beta_1 \\ \vdots \end{pmatrix}}_{\vec{\beta}}. \tag{6.17}$$

As in equation (4.21), the wavefunction coefficients η_n can be determined by cutting A, $\vec{\eta}$ and $\vec{\beta}$ at some cutoff index $\pm n_{\max}$ and numerically inverting A:

$$\vec{E} = A^{-1}\vec{\beta}.$$

Having obtained the coefficients η_n, transmission is determined by demanding current conservation. For this, consider the general probability density current [46]

$$j(x) = \frac{\hbar}{2mi}\left[\psi^*\left(\frac{\partial}{\partial x}\psi\right) - \left(\frac{\partial}{\partial x}\psi^*\right)\psi\right]$$

with its discrete analogue given by equation (4.22). To calculate the current in the system at hand, define the total propagating wavefunction $\psi = \sum_n |u_n\rangle$ where n runs over all propagating channels with $E + n\hbar\omega > 0$. The total current on the left hand side of the potentials is then given by

$$\begin{aligned} J_- &= \int_{-\infty}^{0} j(x)\mathrm{d}x \\ &= \frac{\hbar}{2mi}\sum_n ik_n \int_{-\infty}^{0} \Big[\left(\delta_{n,0}e^{-ik_0x} + r_n^* e^{ik_nx}\right)\left(\delta_{n,0}e^{ik_0x} - r_n e^{-ik_nx}\right) \\ &\qquad - \left(-\delta_{n,0}e^{-ik_0x} + r_n^* e^{ik_nx}\right)\left(\delta_{n,0}e^{ik_0x} + r_n e^{-ik_nx}\right)\Big]\mathrm{d}x \\ &= \underbrace{\frac{\hbar}{m}L_-k_0}_{\text{incoming}} - \underbrace{\frac{\hbar}{m}L_-\sum_n k_n|r_n|^2}_{\text{reflected}} \end{aligned} \tag{6.18}$$

where the infinite length of the system on the left hand side of the potentials L_- was introduced which

will cancel out later. Analogously, the total current on the right hand side of the potentials is given by

$$\begin{aligned} J_+ &= \int_l^\infty j(x)\mathrm{d}x \\ &= \frac{\hbar}{2mi}\sum_n ik_n \int_l^\infty \left[t_n^* e^{-ik_n x} t_n e^{ik_n x} + t_n^* e^{-ik_n x} t_n e^{ik_n x}\right]\mathrm{d}x \\ &= \frac{\hbar}{m} L_+ \sum_n k_n \left|t_n\right|^2 . \end{aligned} \tag{6.19}$$

In a next step, all currents are normalized such that the total incoming current from equation (6.18) is 1. The transmission probability is then given by the ratio of transmitted and incoming current:

$$\begin{aligned} J_{\text{in}} &= \frac{1}{\nu}\frac{\hbar}{m} L_- k_0 \stackrel{!}{=} 1 \qquad \Rightarrow \qquad \nu = \frac{\hbar}{m} L_- k_0 \\ T &= \frac{\frac{1}{\nu} J_+}{J_{\text{in}}} = \sum_n \left|t_n\right|^2 \frac{k_n}{k_0}. \end{aligned} \tag{6.20}$$

where $L_- = L_+$ was used which is valid for an infinite system and for a finite system where the potential barriers are placed in the center. As in M_{TDD}, where transmission is given by equation (4.25), the transmission probability in M_{TDC} is given by the sum over the transmission probabilities of all unbound channels weighted by the particle velocity. Comparison of equations (4.25) and (6.20) demonstrates that the respective particle velocities form a main difference between M_{TDC} and M_{TDD}.

The transmission probability can, finally, be expressed in terms of the coefficients η_n by demanding current conservation $J_- = J_+$. Equating the integrated currents of equations (6.18) and (6.19) and writing r_n in terms of η_n by means of relation (6.11) gives the transmission

$$T = 2\,\mathrm{Re}\left(\eta_0\right) - \sum_n \left|\eta_n\right|^2 \frac{k_n}{k_0}$$

where the sum runs again over all unbound channels. This expression only differs from equation (4.26) for M_{TDD} in the particle velocity factors $k_n \leftrightarrow \sin(k_n)$. Analogously to the derivation for M_{TDD} in section 4, we have obtained a way to calculate transmission in M_{TDC} numerically. In order to use M_{TDC} to gain insight into M_{TDD}, the two models need to be related to each other. This relation is discussed in the following subsection.

6.1.3 Relation between discrete and continuous time-dependent models

In section 5, transport through the high frequency effective model M_{HFD} was explained by means of a continuous model M_{HFC}. Due to the good agreement between the transmission spectra of the two models which were shown to coincide in the limit of small momenta $k_0 \to 0$, an analogue continuous model M_{TDC} to the original model M_{TDD} was derived in section 6.1.1. A method to numerically calculate transport in M_{TDC} was presented in the previous section 6.1.2. In order to use M_{TDC} to explain transport in M_{TDD}, it is necessary to determine a relation between the two models.

In section 5.2, it was argued that, when working with dimensionless momentum rescaled by the inverse lattice spacing, the continuum limit of M_{HFD} corresponds to $k \to 0$ (equations (5.24) to (5.26)).

Any discrete and analogue continuous model are therefore expected to coincide at small momenta which was used in section 5.2.3 to relate the two high frequency models to each other. Since they were found to be time-independent, the only momentum appearing in any equation was the incoming momentum k_0. However, as discussed in sections 4.2 and 6.1.2, Floquet analysis of M_{TDD} and M_{TDC} leads to multiple Floquet channels with index n where waves propagate with momentum k_n. One finds that for the momenta k_n to coincide in time-dependent systems, the limits of small momenta $k_0 \to 0$ and low driving frequencies $\omega \to 0$ need to be taken simultaneously. To see this, first express k_n in M_{TDC} in terms of k_0 and ω using relations (6.9) and (6.10):

$$\frac{\hbar^2 k_0^2}{2m} + n\hbar\omega = \frac{\hbar^2 k_n^2}{2m} \qquad \Rightarrow \qquad k_n = \sqrt{k_0^2 + \frac{2m}{\hbar} n\omega}. \tag{6.21}$$

Using the tight binding dispersion relation (4.14), one finds the same dependence $k_n(k_0, \omega)$ when taking the simultaneous limits $k_0, \omega \to 0$:

$$\begin{aligned} & -2\cos\left(k_0\right) + n\omega' = -2\cos\left(k_n\right) \\ \Rightarrow \quad & \cos\left(k_n\right) = \cos\left(k_0\right) - \frac{n\omega'}{2} = 1 - \frac{k_0^2}{2} - \frac{n\omega'}{2} + O\left(k_0\right)^4 \\ \Rightarrow \quad & k_n = \arccos\left(1 - \frac{k_0^2}{2} - \frac{n\omega'}{2} + O\left(k_0\right)^4\right) = \sqrt{k_0^2 + n\omega'} + O\left(k_0\right)^3 + O\left(\omega'\right)^{\frac{3}{2}}. \end{aligned} \tag{6.22}$$

By comparing equations (6.21) and (6.22), one finds that the dispersion relations of M_{TDD} and M_{TDC} coincide in the limit $k_0, \omega \to 0$ if the driving frequency M_{TDC} is rescaled as

$$\omega' = \frac{2m}{\hbar}\omega.$$

In order to find a quantitative relation between the two models, let us expand the coefficients α_n^n and β_n that are given by equation (4.20). They are required to calculate transmission in M_{TDD} via equations (4.21) and (4.26). In order to obtain a result that is valid for any distance between impurities

l, the product $k_n l$ is kept finite. One obtains

$$\begin{aligned}
\beta_0 =& -2ik_0k_1k_{-1}\left[k_0e^{-ik_0l}+2\left(\frac{1}{(J_2')^2}-1\right)\sin\left(k_0l\right)\right]+O\left(k_0\right)^6+O(\omega)^2\\
\beta_{\pm1} =& -i\left(-\frac{\mu_2'}{(J_2')^2}\right)e^{\mp i\phi}k_0k_{\pm1}k_{\pm2}\sin\left(k_0l\right)+O\left(k_0\right)^5+O(\omega)^2\\
\beta_n =& 0 \quad \text{else}\\
\alpha_0^{(n)} =& k_{n+1}k_{n-1}2\left(\frac{1}{(J_1')^2}-1\right)2\left(\frac{1}{(J_2')^2}-1\right)\sin\left(k_nl\right)\\
&+\frac{1}{4}\left(-\frac{\mu_1'}{(J_1')^2}\right)\left(-\frac{\mu_2'}{(J_2')^2}\right)k_n\left[e^{-i\phi}k_{n+1}\sin\left(k_{n-1}l\right)+e^{i\phi}k_{n-1}\sin\left(k_{n+1}l\right)\right]+O\left(k_0\right)^4+O(n\omega)^2\\
\alpha_{\pm1}^{(n)} =& k_{n\mp1}\left[\frac{1}{2}\left(-\frac{\mu_1'}{(J_1')^2}\right)2\left(\frac{1}{(J_2')^2}-1\right)k_{n\pm1}\sin\left(k_nl\right)+\frac{1}{2}\left(-\frac{\mu_2'}{(J_2')^2}\right)2\left(\frac{1}{(J_1')^2}-1\right)e^{\pm i\phi}k_n\sin\left(k_{n\pm1}l\right)\right]\\
&+O\left(k_0\right)^4+O(n\omega)^2\\
\alpha_{\pm2}^{(n)} =& \frac{1}{4}\left(-\frac{\mu_1'}{(J_1')^2}\right)\left(-\frac{\mu_2'}{(J_2')^2}\right)e^{\pm i\phi}k_nk_{n\mp1}\sin\left(k_{n\pm1}l\right)+O\left(k_0\right)^4+O\left(n\omega'\right)^2
\end{aligned}\tag{6.23}$$

where the rescaled hopping amplitudes $J_i' = J_i/J$ to the impurities are used.

Comparison of these expanded coefficients of M_{TDD} to the analogue coefficients of M_{TDC} given by equation (6.16) immediately yields that, up to orders $O\left(k_0\right)^3$ and $O(\omega)^1$, the two systems are related to each other by

$$\begin{aligned}
v_i' = 2\left(\frac{1}{(J_i')^2}-1\right) \quad &\Leftrightarrow \quad J_i' = \frac{1}{\sqrt{v_i'/2+1}}\\
\text{and} \quad \gamma_i' = -\frac{\mu_i'}{(J_i')^2} \quad &\Leftrightarrow \quad \mu_i' = -\frac{(\gamma_i')^2}{v_i'+2}.
\end{aligned}\tag{6.24}$$

Note that, in section 5.2.3, we found that the high frequency models are related by $V_i' = 2\left(1/(J_{i,\mathrm{eff}'}')^2-1\right)$ (equation (5.42)). Since these models are obtained from M_{TDD} and M_{TDC} by setting

$$v_i' \mapsto V_i \qquad J_{i,\mathrm{eff}'}' \mapsto J_i' \qquad \mu_i' = 0 \qquad \gamma_i' = 0$$

the relations (6.24) between the time-dependent models match with our findings of section 5.2.3.

In this section, we have derived a model M_{TDC} that is expected to show similar transport characteristics as M_{TDD}. A method to numerically calculate transport through this model M_{TDC} was presented and a relation between the parameters of M_{TDD} and M_{TDC} was found. We now have the tools at hand to analyze the transport characteristics of the driven tight binding chain at arbitrary driving frequencies. Before turning to two driven impurities in section 6.3, in the following section 6.2, results

from literature on transmission through a single driven impurity are summarized.

6.2 Single impurity transport

In section 4, we used Floquet theory to show that the periodically driven tight binding chain M_{TDD} can be treated as a static system of multiple tight binding chains coupling to each other at the driven sites with coupling strengths $\mu_i/2$ (figure 4.1). In the previous section 6.1.2, we found an equivalent picture for the analogue continuous model M_{TDC} describing coupled one-dimensional systems with continuous position parameter and coupling strengths $\gamma_i/2$ (figure 6.1). Furthermore, we found that the two models behave similarly in the limit of small momenta and small driving frequencies.

Using the systems' Floquet pictures, in this section we will get an insight into their transport properties by first considering only a single driven impurity. For this, we will, first, discuss how the spectrum changes with respect to the high frequency limit discussed in section 5.3.1 when lowering the driving frequency. We will then get an analytic insight into single impurity transmission by regarding M_{TDC}. The findings in this model will, afterwards, be compared to single impurity transmission of M_{TDD}. For more detailed discussions of the single impurity systems, consider references [21, 26, 27] (discrete system) and [23, 45, 47, 48] (continuous system). The main results of these references will be summarized in the following.

6.2.1 From high to low frequencies

We begin by drawing a relation to the single impurity driven at high frequencies which was discussed in section 5.3.1. In section 5.1.1, we found that in the high frequency limit, the transmission probability depends on the ratio $\mu_i/\omega \equiv \lambda_i$ (equation (5.8)). In order to compare spectra at different driving frequencies to the high frequency limit transmission (5.43), in figure 6.2, the ratio of driving amplitude and frequency λ_i is kept constant. Here, the transmission at finite driving frequencies is computed from equation (4.20) by setting $J_2' = 1$ and $\mu_2' = 0$.

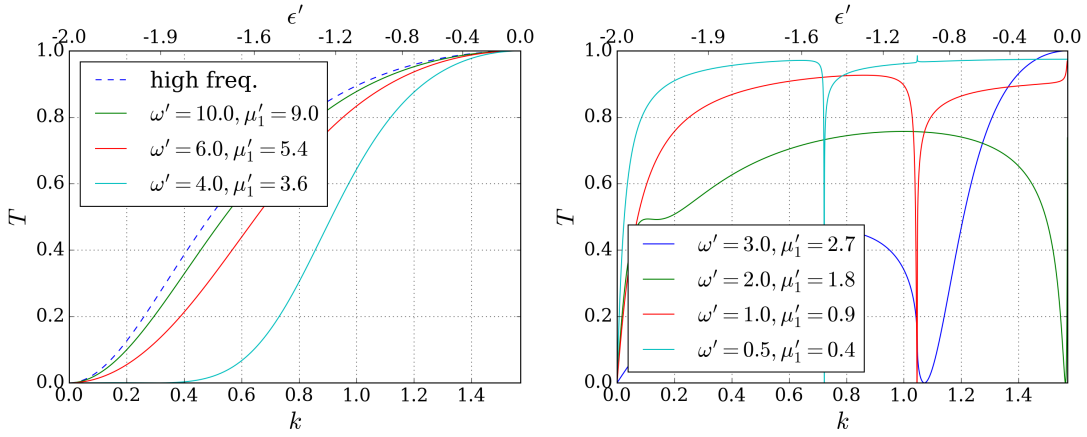

Figure 6.2: Transmission spectra of the driven discrete system with a single impurity at different driving frequencies compared to the high frequency limit discussed in section 5.3.1. A homogeneous chain with $J_1' = 1$ is considered. Left: High frequencies, where qualitatively the spectra do not differ from the high frequency approximation. Right: Lower frequencies where zero transmission resonances appear.

The figure demonstrates that the transmission spectrum at $\omega' = 10$ is well described by the high frequency approximation. For lower frequencies and correspondingly lower driving amplitudes,

the transmission spectrum decreases at all momenta but does not change qualitatively until $\omega' = 4$. While at lower driving frequencies the transmission for most incoming momenta increases, zero transmission resonances occur at certain momenta. The widths of these resonances seem to decrease with decreasing frequency and driving amplitude. To explain these resonances of zero transmission let us take a step back and consider M_{TDC} with a single driven impurity in the following subsection.

6.2.2 Time-dependent continuous model with a single impurity

The model M_{TDC} with a single driven impurity has been discussed thoroughly in references [23, 45, 47, 48]. The main transport characteristics of this model will be explained in the following. By setting $\gamma_2' = v_2' = 0$ in equation (6.16), the recurrence relation (6.15) for a single impurity becomes [26]

$$-2ik_0\delta_{0,n} = \eta_n\left(-2ik_n + v_1'\right) + \frac{\gamma_1'}{2}\left(\eta_{n-1} + \eta_{n+1}\right). \tag{6.25}$$

As explained in sections 4 and 6.1.2, by means of Floquet theory, periodically driven one-dimensional systems can be regarded as multiple channels coupling to each other. The according physical picture is obtained from figure 6.1 and illustrated in the left figure 6.3. Plotting transmission through this model for fixed frequency $\omega' = 1$ and different driving amplitudes in the right figure 6.3 shows resonances which are similar to the ones of M_{TDD} shown in the right figure 6.2.

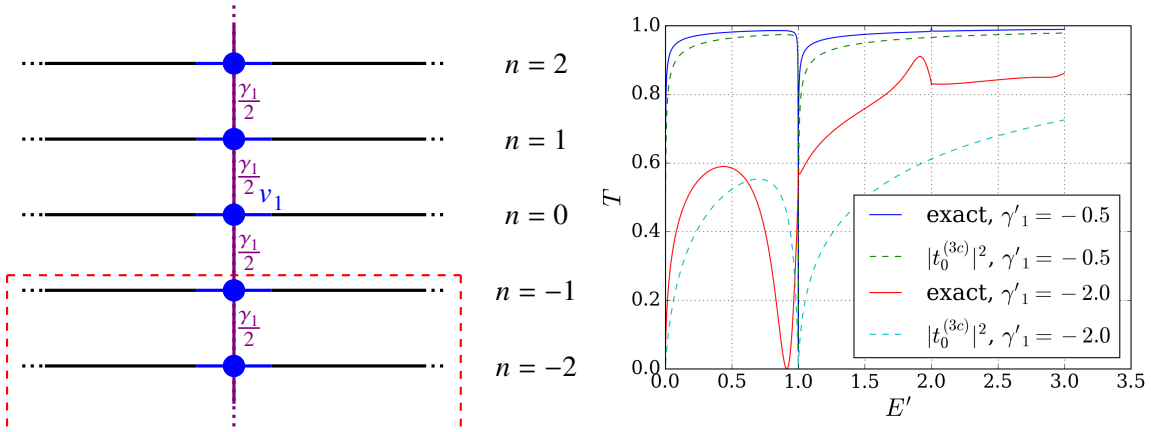

Figure 6.3: Left: As explained in sections 4 and 6.1.2, by means of Floquet theory, periodically driven one-dimensional systems can be understood as a set of coupled channels. Here, the model M_{TDC}, described by the Floquet equation (6.7), with a single impurity is illustrated. The red boxes indicates the side system which, at low incoming energies, only contains bound channels. Right: Transmission spectrum of the continuous driven system with a single impurity with $\omega' = 1$ and without a static potential $v_1' = 0$. The numerically exact spectra considering 41 channels ($n_{\mathrm{max}} = 20$) are compared to the spectra of the three channel approximation ($n_{\mathrm{max}} = 1$).

For an analytic understanding of these resonances, consider the limit of weak driving amplitude $\gamma_1' \ll \omega'$ where the channels with $|n| \geq 2$ couple to the zeroth channel with orders of at least $O(\gamma_1)^2$ and are thus neglected[1]. The resulting three channel approximation corresponds to choosing the cutoff index of matrix A in equation (6.17) as $n_{\mathrm{max}} = 1$.

[1] For a quantitative justification of the finite channel approximation see appendix A in reference [23].

In this approximation, the recurrence relation (6.25) becomes

$$\underbrace{\begin{pmatrix} (-2ik_{-1}+v_1') & \gamma_1'/2 & 0 \\ \gamma_1'/2 & (-2ik_0+v_1') & \gamma_1'/2 \\ 0 & \gamma_1'/2 & (-2ik_1+v_1') \end{pmatrix}}_{A_{3c}} \underbrace{\begin{pmatrix} \eta_{-1} \\ \eta_0 \\ \eta_1 \end{pmatrix}}_{\vec{\eta}_{3c}} = \underbrace{\begin{pmatrix} 0 \\ -2ik_0 \\ 0 \end{pmatrix}}_{\vec{\beta}_{3c}}$$

where the labels '3c' indicate the three channel approximation. The coefficient η_0 is obtained by inverting A_{3c}

$$\vec{\eta}_{3c} = A_{3c}^{-1}\vec{\beta}_{3c}.$$

According to equations (6.8) and (6.11), in the case of a single driven impurity $r_n' = 0$ and thus $t_n = t_n' = \eta_n$. In this way, one finds the transmission amplitude of the zeroth channel [23]

$$t_0^{(3c)} = \eta_0^{(3c)} = \frac{4ik_0}{4ik_0 - 2v_1' - \frac{\gamma_1'}{2}\left(\frac{1}{[ik_1 - v_1'/2]}\right)\frac{\gamma_1'}{2} - \frac{\gamma_1'}{2}\left(\frac{1}{[ik_{-1} - v_1'/2]}\right)\frac{\gamma_1'}{2}} \tag{6.26}$$

which illustrates that transitions from channel 0 to the channels $n = \pm 1$ take place. Even though transmission also takes place through the $n = 1$ channel, its transmission amplitude only contains terms of at least $O(\gamma_1')$. In the weak driving limit, the transmission probability is therefore approximately given by $\left|t_0^{(3c)}\right|^2$. The right figure 6.3 demonstrates that for small γ_1' this approximation describes the exact transmission very well.

One now finds that the transmission amplitude (6.26) can only vanish for imaginary momentum $k_{-1} = i\kappa_{-1}$ with $\kappa_{-1} \in \mathbb{R}$, that is for incoming energies E' where the channel $n = -1$ is bound. According to the dispersion relation (6.10), this is the case for (rescaled) energies

$$E' \equiv \frac{2m}{\hbar^2}E \lesssim \omega'.$$

In this energy range, one finds the transmission amplitude to be identically zero at [23]

$$E_{zt}' = \omega' - \frac{1}{4}\left(v_1'\right)^2.$$

This energy agrees with the location of the zero transmission resonances in figure 6.3 for weak driving amplitudes.

The shape of the transmission resonances is further characterized by the pole of the transmission

amplitude (6.26) which is found as [23]

$$
\begin{aligned}
& E'_{\mathrm{p}} = \tilde{E}' - i\Gamma' \\
\text{with} \quad & \tilde{E}' \simeq \omega' - \frac{1}{4}\left(v'_1\right)^2 \left(1 - \frac{\left(\gamma'_1\right)^2/8}{\tilde{k}_0^2 + \left(v'_1\right)^2/4}\right) \qquad \Gamma \simeq -\frac{\tilde{k}_0 v'_1 \left(\gamma'_1\right)^2/32}{\tilde{k}_0^2 + \left(v'_1\right)^2/4} \\
\text{and} \quad & \tilde{k}_0 \equiv \sqrt{\omega' - \left(v'_1\right)^2/4}
\end{aligned}
$$

such that the transmission amplitude around the impurity becomes

$$
t_0^{(3c)} \sim \frac{E' - E'_{\mathrm{zt}}}{E' - \tilde{E}' + i\Gamma'}. \tag{6.27}
$$

The situation at hand describes a so-called Fano resonance [49], which occurs when a propagating state in the continuum interacts with a discrete energy level, which is, in our case, the bound state energy of the $n = -1$ side system. If the energy of the incoming particle matches a discrete energy level of the attached side system (marked in red in the left figure 6.3), destructive Fano interference with this quasibound state leads to a vanishing transmission amplitude. For this reason, the single driven delta potential has been named 'Fano mirror' in reference [23]. The asymmetric resonance line shape described by equation (6.27) is characteristic for a Fano resonance [21, 23].

At energies $E' > \omega'$, the channel $n = -1$ opens up and due to its real momentum k_{-1} the transmission amplitude (6.26) possesses no real zeros. Nevertheless, it still exhibits complex poles which are observed as kinks in the transmission spectra of figure 6.3). Furthermore, with increasing driving amplitude γ'_1, the three channel approximation loses its validity. Here, the discrete states of the side attached system shift towards lower energies leading to a shift of the zero transmission energy.

Having associated the zero transmission resonances of M_{TDC} with a single impurity to the Fano effect, let us compare the findings to transmission in M_{TDD} with a single impurity in the following subsection.

6.2.3 Discrete model with a single impurity

The discrete system with a single driven impurity has been analyzed thoroughly in references [21, 26]. However, the relation to the time-dependent continuous model M_{TDC} has only been discussed briefly in reference [26]. The according physical picture of multiple tight binding chains coupling to each other at site 0 is obtained from figure 4.1 by setting $\mu'_2 = 0$ and $J'_2 = 1$. It is illustrated in the left figure 6.4.

As for M_{TDC} in figure 6.3, transmission through the discrete system M_{TDD} is plotted for fixed frequency $\omega' = 1$ and varying driving amplitude μ'_1. A comparison of the right figures 6.3 and 6.4 shows that, even outside of the limits $\omega, k_0 \to 0$, the transmission spectra behave stunningly similar.

As pointed out before, the main difference between the spectra of M_{TDD} and M_{TDC} lies in the different dispersion relations (4.14) and (6.9). Firstly, the discrete dispersion relation (4.14) leads to a symmetric spectrum around $k_0 = \pi/2$. Secondly, the continuum energy band is not only bounded from below, as in the continuous case, but also from above. As discussed in section 4.2, this leads to unbound channels with $|\varepsilon'_n| < 2$ and bound channels outside this band. In the following, let us discuss whether the zero transmission resonances of M_{TDD} can be understood in terms of Fano interference, as

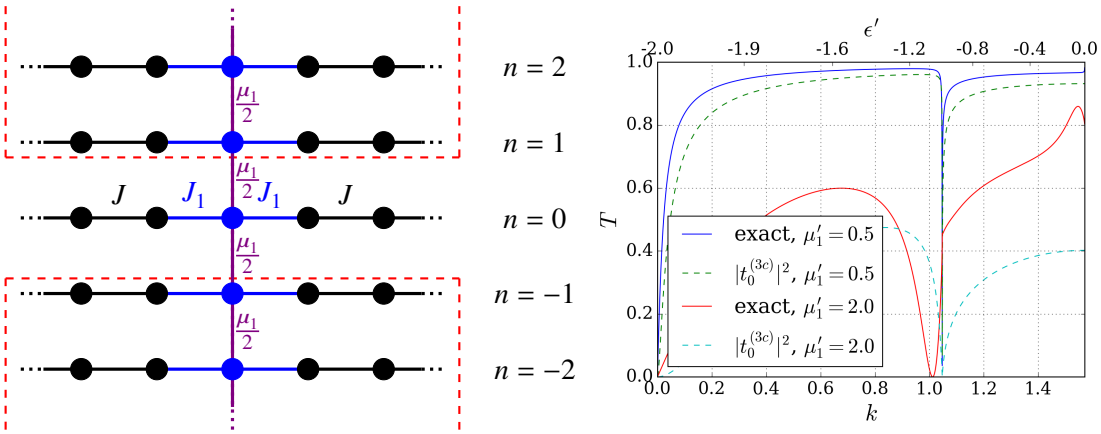

Figure 6.4: Left: Illustration of the discrete system described by the Floquet equation (4.3) with a single impurity. The red boxes indicate the virtual side systems which contain a number of propagating channels that depends on the incoming particle's energy and the driving frequency. The illustration is adapted from reference [21]. Right: Transmission spectrum of the discrete system with a single impurity and $\omega' = 1$. A homogeneous chain with $J_1' = 1$ is considered. The numerically exact spectra calculated from 41 channels ($n_{\max} = 20$) are compared to the spectra of the three channel approximation ($n_{\max} = 1$). Note the striking similarity to the transmission spectra of M_{TDC} shown in the right figure 6.3. The driving amplitudes μ_1' and γ_1' are related to each other according to relation (6.24).

was the case in the continuous system, or whether the different dispersion relation requires a different explanation.

For this, consider the recurrence relation (4.19) with coefficients (4.20) for a single impurity [26]

$$-2i\sin(k_0)\delta_{n,0} = E_n\left[-2i\sin(k_n) + 2\left(\frac{1}{(J_1')^2} - 1\right)\cos(k_n)\right] - \frac{\mu_1'}{2(J_1')^2}\left(E_{n+1} + E_{n-1}\right).$$

This recurrence relation coincides with the continuous recurrence relation (6.25) when mapping

$$k_n \mapsto \sin(k_n) \qquad v_1' \mapsto 2\left(\frac{1}{(J_1')^2} - 1\right)\cos(k_n) \qquad \gamma_i' \mapsto -\frac{\mu_1'}{(J_1')^2} \tag{6.28}$$

which, in the limits $k, \omega' \to 0$, leads to the relations (6.24) which were found in section 6.1.3.

At this point, one could proceed as for M_{TDC} above, by considering small driving amplitudes $\mu_i' \ll \omega'$ and applying the three channel approximation. However, to obtain the transmission amplitude of channel zero in the three channel approximation, it is sufficient to insert the mappings (6.28)

between discrete and continuous models with a single impurity into the transmission amplitude (6.26):

$$\begin{aligned} t_0^{(3c)} =& \eta_0^{(3c)} \\ =& 4i\sin(k_0)\cdot\left[4i\sin(k_0) - 4\left(\frac{1}{(J_1')^2}-1\right)\cos(k_0) - \frac{\mu_1'}{(J_1')^2}\frac{1}{\left[i\sin(k_1) - \left(\frac{1}{(J_1')^2}-1\right)\cos(k_1)\right]}\frac{\mu_1'}{(J_1')^2}\right. \\ & \left. - \frac{\mu_1'}{(J_1')^2}\frac{1}{\left[i\sin(k_{-1}) - \left(\frac{1}{(J_1')^2}-1\right)\cos(k_{-1})\right]}\frac{\mu_i'}{(J_i')^2}\right]^{-1}. \end{aligned} \tag{6.29}$$

As argued in section 6.2.2, in the weak driving limit, the transmission probability is well approximated by $\left|t_0^{(3c)}\right|^2$, because, even though channels $n = \pm 1$ might be unbound as well, they only contain terms of at least $O(\gamma_1')$. The right figure 6.4 demonstrates the validity of this approximation for weak driving amplitudes.

To find the zero transmission energy, note that in the spectra of figure 6.4, the zero transmission resonances with small μ_i' are observed at energies just below $\varepsilon' = -2 + \omega'$ where channel $n = -1$ is still bound. Due to the spectra's symmetry around $\varepsilon' = 0$, the same resonance is observed just above $\varepsilon' = 2 - \omega'$ before channel $n = 1$ becomes unbound. Writing all momenta in the transmission amplitude (6.29) in terms of ε' and ω' by means of equations (4.14) and (4.15) and solving $t_0 = 0$ for ε', one finds zero transmission at [26]

$$\varepsilon_{\mathrm{zt}}' = \pm\left(\omega' - \frac{2\left(J_1'\right)^2}{\sqrt{2\left(J_1'\right)^2 - 1}}\right).$$

Again, this resonance energy agrees with the spectra in figure 6.4. As discussed above for M_{TDC}, Fano interference is responsible for the observed resonance when propagating solutions of the continuum interact with discrete energy levels of the side system [21]. One of these discrete levels, which in an isolated system would lie outside of the continuum, is pushed inside unbound energy band by the interaction term μ_1'. The resulting quasibound state affects transmission and leads to the typical asymmetric line shape of a Fano resonance. However, note that, exactly at the energies of zero transmission $\varepsilon_{\mathrm{zt}}'$, the wavefunction in channel 0 at the position of the impurity η_0 vanishes. Therefore, the side systems decouple from the central chain and what was a quasibound state in the continuum before becomes a bound state in the continuum (BIC). Such BIC were first described in reference [50] and are known to influence transport [51, 52].

Besides these zero transmission resonances which occur at $|\varepsilon'| > |\omega' - 2|$, weaker Fano resonances with finite transmission probability are observed at energies closer to $\varepsilon' = 0$ whenever ε' matches another quasibound state of the side attached systems (see the right figure 6.4, just at $\varepsilon' \lesssim 0$).

Before switching on the second impurity in the next section and discussing how the described transport phenomena change, let us briefly discuss transmission outside of the weak driving limit. For this, in the left figure 6.5, transmission in M_{TDC} is calculated for fixed (low) driving frequency and varying driving amplitude. According to the relation between M_{TDD} and M_{TDC} (6.24), the driving

amplitudes γ_1' are translated into driving amplitudes of the discrete system μ_1' and the corresponding transmission probabilities for M_{TDD} are illustrated in the right figure 6.5. The similarity between continuous and discrete transmission for weak drivings is stunning.

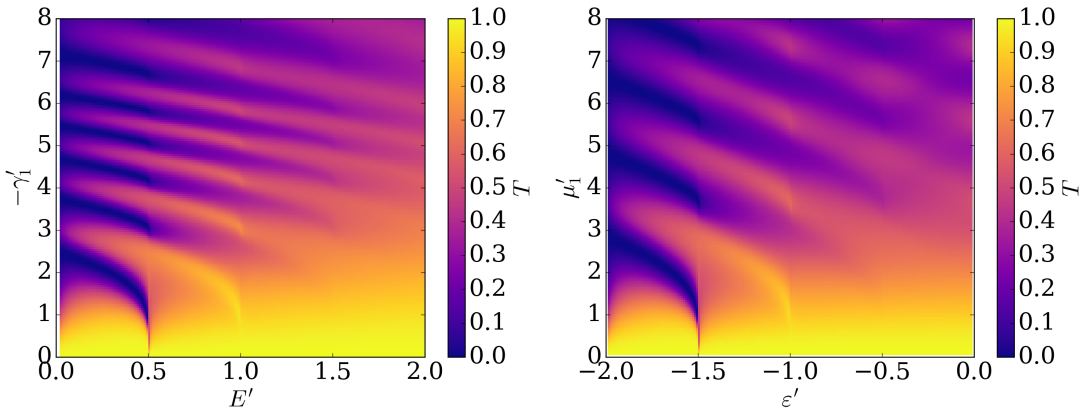

Figure 6.5: Comparison of the transmission spectra M_{TDC} (left) and M_{TDD} (right) for a single driven impurity driven at $\omega' = 0.5$. Both systems are chosen homogeneous with $v_1' = 0$ and $J_1' = 1$. According to relation (6.24), the driving amplitudes of the left plot correspond to those in the discrete model plotted in the right.

Above, we found that, in the weak driving limits $\gamma_1', \mu_1' \to 0$ and for homogeneous chains, the zero transmission resonance is located close to $E' = \omega'$ and $\varepsilon_{\mathrm{zt}}' = \pm\left(\omega' - 2\right)$ respectively. When increasing the driving amplitude, this resonance shifts towards lower energies. At a certain driving amplitude $\mu_1' \approx 2.8$ the resonance energy reaches $\varepsilon_{\mathrm{zt}}' \approx \mp 2$ and the resonance vanishes for larger μ_1'. In a repeating fashion, the resonance is then restored at $\varepsilon_{\mathrm{zt}}' \approx \pm(\omega' - 2)$ and shifts towards $\varepsilon_{\mathrm{zt}}' \approx \mp 2$ again. Again, this effect can be understood by means of Fano interference with a quasibound state of the side attached system [26]. With increasing coupling between channels, the energy of this discrete state is lowered until it is pushed out of the continuum when the resonance disappears. When further increasing the coupling to the side system, another discrete level is pulled inside the band and the resonance is restored.

In conclusion, we are able to explain the zero transmission resonances of continuous and discrete systems by means of Fano interference. In the discrete system, this effect leads to bound states in the continuum occurring at the critical point of zero transmission where the side systems decouple from the zeroth channel. Having understood the transmission spectrum for a single impurity, let us switch on the second impurity and discuss, in the following section, how this affects the transmission spectrum.

6.3 Two impurity transport

In the previous section 6.2, transmission through a tight binding chain with a single driven impurity was discussed. The three channel approximation to the multichannel scattering problem, which is justified in the limit of small driving amplitudes, was used to identify Fano resonances which equally appear in the analogue continuous model M_{TDC} derived in section 6.1. These Fano resonances were explained by means of the Floquet picture consisting of multiple interacting channels which was derived in sections 4 (discrete model M_{TDD}) and 6.1.2 (continuous model M_{TDC}): Due to the interaction between channels, discrete levels of the side systems are pushed inside the continuum and, thus, lead to quasibound states. For the discrete model M_{TDD}, it was found that, at the energy of zero transmission, the side systems decouple from the zeroth channel, such that the quasibound states become bound states in the continuum.

In this section, we regard the full model of two driven impurities which was introduced in section 2 and Floquet transformed in section 4 and which, to our knowledge, has not been analyzed before. For this, we take advantage of the analogous model M_{TDC} with two driven delta potentials. This system has been analyzed previously in references [24, 53].

In order to connect the full time-dependent model M_{TDD} to the high frequency effective model M_{HFD} which was discussed in section 5, we will first observe how the transmission spectrum changes when leaving the high frequency limit. Analogously to the discussion of a single impurity in section 6.2, the appearing features will, then, be explained in the limit of small driving amplitudes using the three channel approximation.

6.3.1 From high to low frequencies

In section 5.1.1, we found that, in the limit of high driving frequencies, the time-dependent model M_{TDD} reduces to a static effective model M_{HFD} with effective hopping amplitudes $J_{i,\mathrm{eff}}$ to the impurities. The transmission probability through these static impurities was calculated in section 5.1.2 and several interesting transport characteristics were discussed in section 5.3. For symmetrically driven systems with strong impurities (that is small effective hopping amplitudes), we identified maxima of perfect transmission accompanied by confined wavefunction modes. For weaker impurities, the transmission resonances become broader which leads to a broadening of the perfect transmission peaks. Due to a shift in the resonant momenta and the effect of multiple resonances overlapping, the perfect transmission peaks were furthermore observed to shift towards lower momenta. As soon as the effective hopping amplitudes exceed the bulk hopping amplitude, bound states emerge which lead to the critical phenomenon of finite transmission at zero incoming momentum, a so-called threshold anomaly.

It is the purpose of this section, to observe how these transmission features change when leaving the high frequency limit and considering M_{TDD}. In order to reduce the number of free parameters and focus on the effect of the driving field, we will consider a homogeneous tight binding chain $J_1' = J_2' = 1$ and symmetric impurities with $\mu_1' = \mu_2' \equiv \mu'$ and $\phi = 0$. In figure 6.6, the high frequency transmission (5.23) is compared to the transmission spectra at finite frequencies calculated with the method explained in section 4.2. For a valid comparison to the high frequency limit where the transmission probability only depends on the ratio of driving amplitude and frequency $\mu'/\omega' = \lambda$ (equation (5.8)), this ratio is kept constant for all plotted spectra.

The left figure 6.6 illustrates that for frequencies $\omega' \gtrsim 6$ the transmission spectrum is well described

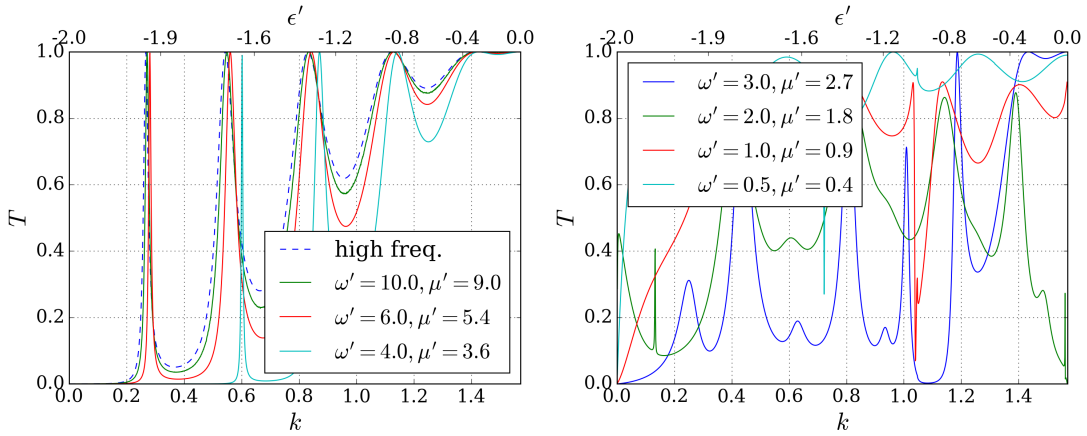

Figure 6.6: Transmission spectra of M_{TDD} with two symmetrically driven impurities at a distance of $l = 10$ sites and at various driving frequencies compared to the high frequency limit discussed in section 5.3.1. A homogeneous chain with $J' = 1$ is considered. Compare to the single impurity spectra in figure 6.2 to observe the effect of a second impurity. Left: High frequencies, where qualitatively the spectra do not differ from the high frequency approximation. Right: Lower frequencies where sharp transmission features appear.

by the high frequency approximation. In this range, the main difference between infinite and finite frequencies is a slight decrease of transmission for most of the spectrum which is due to the fact that at finite frequencies the driving is less averaged and effectively creates a stronger impurity.

As demonstrated in the right figure 6.6, for lower frequencies $\omega' \lesssim 3$, the transmission spectrum deviates strongly from the high frequency result. In this frequency range, it seems like the overall transmission increases with decreasing frequency. Furthermore, many transmission maxima and minima are observed at different particle energies. A comparison to the corresponding single impurity spectra in the right figure 6.2 suggests that the single impurity Fano resonances occur at similar incoming energies but are accompanied by new features stemming from the second impurity. As in the discussion of single impurities in section 6.2, let us get an analytic insight into these new features by considering the time-dependent continuous model M_{TDC} in the limit of weak driving amplitudes in the following section.

6.3.2 Time-dependent continuous model with two impurities

We have seen before, that properties of the periodically driven tight binding chain M_{TDD} could be understood by considering the analogue continuous model M_{TDC}. In section 6.1.3 we found that M_{TDD} and M_{TDC} coincide in the limit of small incoming momenta and small driving frequency. We can, therefore, expect to identify resonances of M_{TDD} by comparing its transmission spectrum to the one of M_{TDC} at low driving frequencies.

In order to get analytic insight into the transmission spectrum of M_{TDC}, let us proceed as in section 6.2 and consider the weak driving limit where the three channel approximation is valid[2]. Considering only the central Floquet channels $n \in \{-1, 0, 1\}$ corresponds to reducing the matrix A in equation (6.17) to the central 3×3 entries. Inversion of this matrix and multiplication with $\vec{\beta}$ leads

[2] The validity of the three channel approximation is shown in appendix A of reference [23].

to the three channel approximation of the vector $\vec{\eta}$ denoted $\vec{\eta}_{3c}$. The transmission amplitude is then calculated by combining equations (6.11) and (6.14) which yields

$$t_0^{(3c)} = 2ie^{-ik_0 l}\sin(k_0 l) + \eta_{3c,0}\left[1 - \left(2i - \frac{v_1'}{k_0}\right)e^{-ik_0 l}\sin(k_0 l)\right] + \left[\eta_{3c,-1} + \eta_{3c,1}\right]\frac{\gamma_1'}{2}e^{-ik_0 l}\frac{\sin(k_0 l)}{k_0}. \tag{6.30}$$

Inserting the components of $\vec{\eta}_{3c}$ into this equation (6.30) gives a very long expression. To obtain manageable terms, let us consider symmetric impurities with $\gamma_1' = \gamma_2' \equiv \gamma'$ and $v_1' = v_2' \equiv v'$ and no phase between the two drivings, $\phi = 0$. As for the single driven impurity discussed in section 6.2.2, one finds that a drop in transmission to identically zero is only possible for incoming energies $E' < \omega'$ where the channel $n = -1$ is bound and thus has imaginary momentum $k_{-1} = i\kappa_{-1}$. Including terms of $O(\gamma')^2$, one then finds vanishing transmission at energies E_{zt} that solve the equation [24]

$$\left[-\left(v' + 2\kappa_{-1}\right)\cosh\left(\frac{\kappa_{-1}l}{2}\right) + \kappa_{-1}e^{-\frac{\kappa_{-1}l}{2}}\right] \times \left[-\left(v' + 2\kappa_{-1}\right)\sinh\left(\frac{\kappa_{-1}l}{2}\right) + \kappa_{-1}e^{-\frac{\kappa_{-1}l}{2}}\right] = \frac{(\gamma')^2\kappa_{-1}}{4k_0}\sin\left(\frac{k_0 l}{2}\right)\cos\left(\frac{k_0 l}{2}\right). \tag{6.31}$$

For a given combination of l and ω', solutions to this equation are plotted in figure 6.7. The physical reason for the zero transmission resonances produced by the two terms on the left hand side of equation (6.31) can be understood by further investigating the analytic structure of the transmission amplitude calculated from equation (6.30). In section 6.2.2, we explained that vanishing transmission through a single impurity is caused by Fano interference between the propagating particle's state and the discrete level of the $n = -1$ side system. This resonance was identified as a pole in the transmission amplitude in three channel approximation.

In reference [24], it was reported that the transmission amplitude (6.30) for two impurities exhibits two possible poles arising from Fano interference. These poles are accompanied by wavefunctions that are either symmetric (bonding states) or anti-symmetric (antibonding). Up to $O(\gamma')^2$, the pole associated to symmetric (bonding) wavefunctions is determined from equation [24]

$$-\left(v' + 2\kappa_{-1}\right)\cosh\left(\frac{\kappa_{-1}l}{2}\right) + \kappa_{-1}e^{-\frac{\kappa_{-1}l}{2}} = \frac{(\gamma')^2}{4}\frac{\cosh\left(\frac{\kappa_{-1}l}{2}\right)\cos\left(\frac{k_0 l}{2}\right)}{\left(2ik_0 - v'\right)\cos\left(\frac{k_0 l}{2}\right) - ik_0 e^{i\frac{k_0 l}{2}}} \tag{6.32}$$

whereas the anti-symmetric (anti-bonding) wavefunctions arise at the pole given by [24]

$$-\left(v' + 2\kappa_{-1}\right)\sinh\left(\frac{\kappa_{-1}l}{2}\right) + \kappa_{-1}e^{-\frac{\kappa_{-1}l}{2}} = \frac{(\gamma')^2}{4}\frac{\sinh\left(\frac{\kappa_{-1}l}{2}\right)\sin\left(\frac{k_0 l}{2}\right)}{\left(2ik_0 - v'\right)\sin\left(\frac{k_0 l}{2}\right) - k_0 e^{i\frac{k_0 l}{2}}}. \tag{6.33}$$

As for the single particle transmission poles, these two poles result from interaction with the discrete energy levels of the $n = -1$ channel. In fact, we have already come across the bound state spectrum of

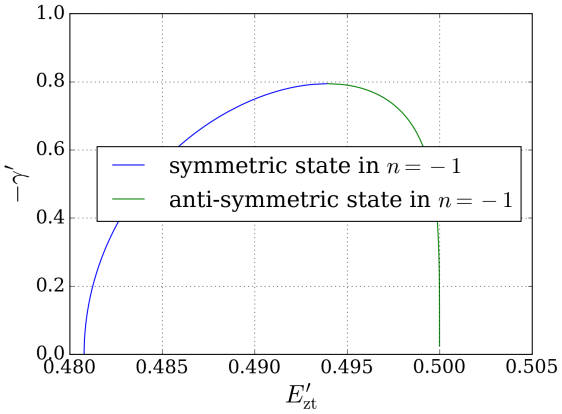

Figure 6.7: Energies where, in three channel approximation, zero transmission occurs in the model M_{TDC} with two impurities at a distance $l = 5$, driven at frequency $\omega' = 0.5$. These energies are calculated according to equation (6.31) as a function of the driving amplitude. This equation is only valid for small driving amplitudes up to $O(\gamma')^2$. At larger values of γ', we expect the two solutions to lie very close to each other and shift towards lower energies.

a one-dimensional continuous system when discussing discrete states of the high frequency continuous model M_{HFC} in section 5.3.5. It was found that M_{HFC} exhibits a single symmetric bound state for weak impurities (quantified by the impurity strength $V' \lesssim 0$) with a second anti-symmetric bound state appearing for sufficiently strong impurities. Analogously the bound channel $n = -1$ can also either feature a single symmetric or a second anti-symmetric state. These two bound states lead to the two poles described by equations (6.32) and (6.33) and, thus, give two Fano resonances in the transmission spectrum. These resonances are thoroughly discussed in reference [24]. Here, I will only briefly summarize their effect on the transmission amplitude before turning to the driven discrete system M_{TDD} that is the subject of this thesis.

A comparison of equations (6.32) and (6.33) to the zero transmission relation (6.31) suggests that the first term on the left hand side of equation (6.31) is associated to the pole with symmetric wavefunction whereas the second term corresponds to the pole of anti-symmetric wavefunction. Therefore, at least in the limit of small driving amplitudes, the two poles produce the two zero transmission resonances depicted in figure 6.7. In fact, in the limit $\gamma' \to 0$, the energies of zero transmission are identical to the real energies $E_{\mathrm{p}}^{\prime(s,a)(0)}$ solving the pole equations (6.32) and (6.33). The finding of real pole energies at vanishing driving strength corresponds to infinitely sharp resonances in this limit [24].

For finite driving amplitudes the energies of zero transmission can be found as a perturbation to the energies at vanishing drivings [24]:

$$E_{\mathrm{zt}}^{\prime(s,a)} = E_{\mathrm{p}}^{\prime(s,a)(0)} + \frac{1}{8}\left(\gamma'\right)^2 v' \frac{1}{k_0} \sin\left(\frac{k_0 l}{2}\right) \cos\left(\frac{k_0 l}{2}\right).$$

Furthermore, outside the limit $\gamma' \to 0$, the poles are located at complex energies

$$E_{\mathrm{p}}^{\prime(s,a)} = \tilde{E}'_{s,a} - i\Gamma'_{s,a}$$

where the upper indices 's' and 'a' denote the pole with symmetric and anti-symmetric wavefunction

respectively. The transmission spectum around the resonances is therefore again described by the Fano line shape (6.27)

$$t_0(E') \sim \frac{E' - E'_{\mathrm{zt}}}{E' - \tilde{E}'_{s,a} + i\Gamma'_{s,a}}.$$

We have thus found that, just as for a single impurity, Fano resonances occur as a result of propagating states interacting with discrete energy levels of the side system. Due to the second impurity, this side system exhibits a more complex energy spectrum than the one with a single impurity. In the three channel approximation, which is valid for weak driving amplitudes, a symmetric and an anti-symmetric state arise which are characteristic for a symmetric double delta potential as discussed in section 5.3.5. In the following and last section, we will transfer these findings to the model M_{TDD} to analyze its transmission spectrum.

6.3.3 Discrete model with two impurities

In the previous section, it was discussed that, at low driving amplitudes, the three channel approximation of M_{TDC} reveals two Fano resonances which lead to zero transmission. These two resonances are associated to a symmetric and an anti-symmetric bound state of the $n = -1$ channel. In this section, we will use the relation between M_{TDC} and M_{TDD} that was found in section 6.1.3 to identify analogous bound states in the discrete model M_{TDD} and relate them to resonances of the transmission amplitude.

One approach to locate energies/momenta of zero transmission in M_{TDD}, would be the usage of the three channel approximation as for M_{TDC} in the previous section. The three channel transmission amplitude can be calculated analogously to the three channel approximated transmission amplitude of M_{TDC} (6.30). Unfortunately, the resulting expression is so long that standard symbolic computation software can not determine a common denominator within a reasonable computation time. This, however, would be necessary to analyze its poles and zeros.

In the limit of small driving frequency, approximate equations for zero transmission and the location of poles can be found by inserting the relations between M_{TDD} and M_{TDC} (6.24) into equations (6.31) to (6.33). In this way, one obtains equations for zeros and poles of the transmission amplitude that are valid in the simultaneous limits of small driving amplitudes μ', where the finite channel approximation is valid, and in the limits of small driving frequencies ω' and momenta k_0, where the relation between M_{TDD} and M_{TDC} holds. One finds zero transmission at

$$\left[-2\left(\left(\frac{1}{(J'_{\mathrm{imp}})^2} - 1\right) + \kappa_{-1}\right)\cosh\left(\frac{\kappa_{-1}l}{2}\right) + \kappa_{-1}e^{-\frac{\kappa_{-1}l}{2}}\right]$$
$$\times\left[-2\left(\left(\frac{1}{(J'_{\mathrm{imp}})^2} - 1\right) + \kappa_{-1}\right)\sinh\left(\frac{\kappa_{-1}l}{2}\right) + \kappa_{-1}e^{-\frac{\kappa_{-1}l}{2}}\right] = \frac{\left(\frac{\mu'}{(J'_{\mathrm{imp}})^2}\right)^2 \kappa_{-1}}{4k_0}\sin\left(\frac{k_0 l}{2}\right)\cos\left(\frac{k_0 l}{2}\right) \tag{6.34}$$

and the two poles at

$$
\begin{aligned}
&-2\left(\left(\frac{1}{(J'_{\mathrm{imp}})^2}-1\right)+\kappa_{-1}\right)\cosh\left(\frac{\kappa_{-1}l}{2}\right)+\kappa_{-1}e^{-\frac{\kappa_{-1}l}{2}} \\
&=\frac{\left(\frac{\mu'}{(J'_{\mathrm{imp}})^2}\right)^2}{4}\frac{\cosh\left(\frac{\kappa_{-1}l}{2}\right)\cos\left(\frac{k_0 l}{2}\right)}{2\left(ik_0-\left(\frac{1}{(J'_{\mathrm{imp}})^2}-1\right)\right)\cos\left(\frac{k_0 l}{2}\right)-ik_0e^{i\frac{k_0 l}{2}}}
\end{aligned}
\tag{6.35}
$$

(symmetric wavefunction) and

$$
\begin{aligned}
&-2\left(\left(\frac{1}{(J'_{\mathrm{imp}})^2}-1\right)+\kappa_{-1}\right)\sinh\left(\frac{\kappa_{-1}l}{2}\right)+\kappa_{-1}e^{-\frac{\kappa_{-1}l}{2}} \\
&=\frac{\left(\frac{\mu'}{(J'_{\mathrm{imp}})^2}\right)^2}{4}\frac{\sinh\left(\frac{\kappa_{-1}l}{2}\right)\sin\left(\frac{k_0 l}{2}\right)}{2\left(ik_0-\left(\frac{1}{(J'_{\mathrm{imp}})^2}-1\right)\right)\sin\left(\frac{k_0 l}{2}\right)-k_0e^{i\frac{k_0 l}{2}}}.
\end{aligned}
\tag{6.36}
$$

(anti-symmetric wavefunction). Here, the dimensionless hopping amplitude to the impurities $J'_{\mathrm{imp}} \equiv J_1/J = J_2/J$ was introduced. Thus, we have thus found analytic expressions to determine zeros and poles of the transmission amplitude of M_{TDD}.

In figure 6.8, using equation (6.34), the energies of zero transmission in three channel approximation are calculated as a function of the driving amplitude μ'. As shown for the continuous model M_{TDC} in figure 6.7, for low driving frequencies, two resonances are predicted, which lead to zero transmission. Again, these are associated to two Fano resonance poles, given by equations (6.35) and (6.36).

In figure 6.9, for certain parameter sets where the three channel approximation and the relation between M_{TDC} and M_{TDD} are valid, the predicted momenta of zero transmission are compared to the numerically determined transmission spectra. It seems like the number of resonances and the corresponding momenta are well approximated. The deviations from equation (6.34) are, presumably, mostly due to the finite frequency ω'. According to the recurrence relation's coefficients (6.23), the relation between M_{TDC} and M_{TDD} only holds up to $O(\omega')^1$.

Since the analytic expressions (6.34) to (6.36) are only valid in the simultaneous limits $\mu', \omega', k_0 \to 0$, let us now analyze how these transmission characteristics evolve outside of these limits. For this, in figure 6.10, the transmission spectrum of M_{TDD} is compared to the one of M_{TDC}. At the chosen driving frequency $\omega' = 0.5$, it is apparent that the two transmission spectra agree very well for weaker driving amplitudes $\mu' \approx -\gamma' \lesssim 2$.

For small driving amplitudes, the predicted momenta of perfect transmission are highlighted according to equations (6.31) (M_{TDC}) and (6.34) (M_{TDD}). They appear as single red lined, but, as depicted in figures 6.7 and 6.8, they actually consist of two zero transmission resonances within a narrow energy range. For stronger drivings $\mu' \approx -\gamma' \gtrsim 0.7$, the three channel approximation seems to lose its validity and equations (6.31) and (6.34) do not hold any more. It is therefore not possible to

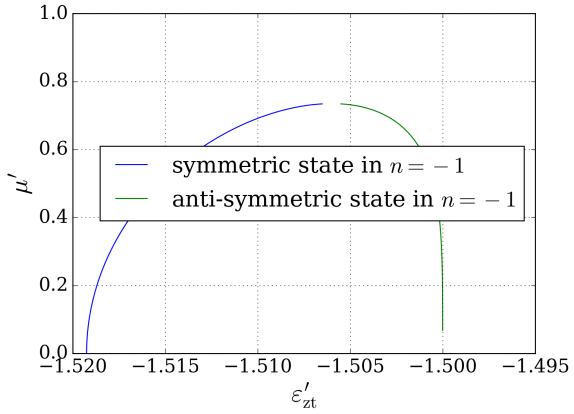

Figure 6.8: Energies where, in three channel approximation, zero transmission occurs in the model M_{TDD} with two impurities at a distance $l = 5$, driven at frequency $\omega' = 0.5$. These energies are calculated according to equation (6.34) as a function of the driving amplitude. This equation is only valid for small driving amplitudes up to $O(\mu')^2$. At larger values of μ', we expect the two solutions to lie very close to each other and shift towards lower energies.

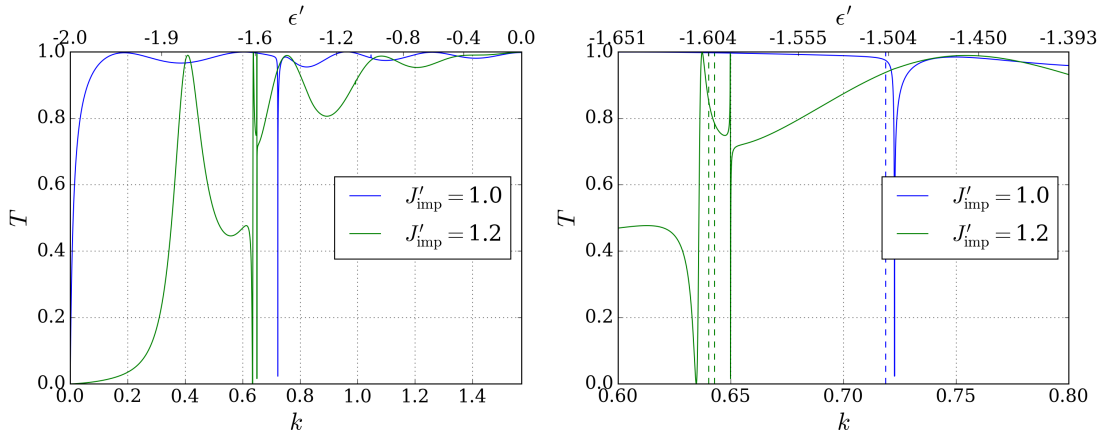

Figure 6.9: Left: Transmission spectrum for two driven impurities at a distance $l = 10$, driven at a frequency $\omega' = 0.5$ with amplitude $\mu' = 0.2$. Right: Zoom into the momentum range where the transmission resonances occur. The dashed lines indicate the momenta of zero transmission determined from to the approximate equation (6.34) (green lines $J'_{\mathrm{imp}} = 1.2$, blue line $J'_{\mathrm{imp}} = 1$). This figure demonstrates that, as predicted, at $J'_{\mathrm{imp}} = 1.2$ two zero transmission resonances lie close together.

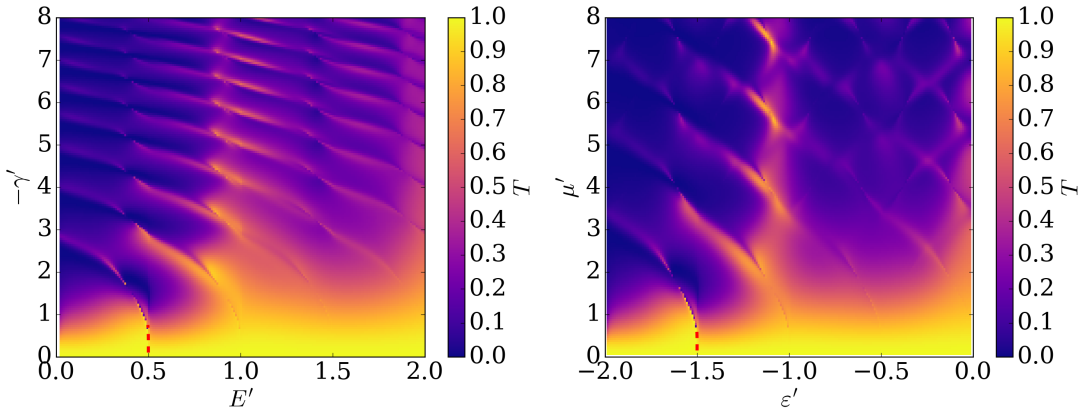

Figure 6.10: Comparison of the transmission spectra of M_{TDC} (left) and M_{TDD} (right) for two driven impurities at a distance $l = 5$ and driven at $\omega' = 0.5$. Both systems are chosen homogeneous with $v' = 0$ and $J'_{\mathrm{imp}} = 1$. According to relation (6.24), the driving amplitudes of the left plot correspond to those for M_{TDD} plotted in the right. The red dashed lines at energies $E' \approx \omega'$ (left) and $\varepsilon' \approx -2+\omega'$ indicate the energies of zero transmission calculated from equations (6.31) and (6.34) that hold for small driving amplitudes. They appear as single lines, but as shown in figures 6.7 and 6.8, they actually consist of two zero transmission resonances very close to each other.

determine analytically, whether outside of the three channel approximation, a single resonance or two resonances close to each other exist. In figure 6.10, only a single prominent feature is visible which, for increasing driving amplitude, shifts towards lower energies until it is pushed out of the continuum at $\mu' \approx 3$ ($-\gamma' \approx 2.7$) . Furthermore, at higher energies, the resonance structure seems to repeat after energy intervals of ω'.

A comparison of figure 6.10 to the corresponding transmission plots for a single impurity in figure 6.5 shows that the same resonance shifts and repeating structures at energy intervals of ω' are observed for a single impurity. Therefore, let us, first, focus on the similarities between single impurity and two impurity systems and explain the occurring features analogously to the single impurity discussion in section 6.2: For energies $\varepsilon' < -2+\omega$, the Floquet channel $n = -1$ is bound and, depending on the driving amplitude, features either one or two discrete states. Due to the interaction between channels, quantified by the interaction strength $\mu'/2$ (see figure 4.1), the energies of these discrete states are pushed inside the energy continuum.

When the energy of a propagating state lies close to this discrete state's energy, Fano interference leads to sharp features in the transmission amplitude and a strong decrease in the transmission probability. For weak driving amplitudes, these discrete states can be determined from equations (6.35) and (6.36) which yield resonant energies with real parts close to $-2+\omega'$ and very small imaginary parts corresponding to very sharp resonances. At stronger driving strengths, the energies of the discrete states in the continuum are lowered which leads to the Fano resonances occurring at lower energies until they are pushed out of the continuum. At energies $\varepsilon' > -2+\omega$, where the $n = -1$ channel is unbound, the interaction between propagating states and discrete states of lower channels which lie at energy distances of integer multiples of ω', lead to further Fano resonances. These give the repeating structures in the plots of figure 6.10.

After having focused on the similarities between single impurity and two impurity systems, let us explore the differences between the corresponding transmission spectra by, again, comparing figures

6.5 and 6.10. First of all, for driving strengths $\mu' \approx -\gamma' \gtrsim 1.5$, the second impurity leads to a global decrease of the transmission probability. The fact that a second impurity leads to increased scattering and, thus, to a decrease in transmission is intuitive. Secondly, the transmission features at the Fano resonances seem to have a more complex structure. In fact, for various parameter combinations, sharp minima and maxima of transmission appear close to each other which is not observed for single impurities. Thirdly, a dominant transmission maximum appears at $\varepsilon' \approx -1.1$, independently of the driving amplitude μ'.

There is no analytic tool at hand to understand the sharp Fano resonances and the maxima μ'-independent for arbitrarily large driving amplitude. However, an insight into these features can be expected from a numerical analysis of the quasienergy operator which, as explained in section 3.2, governs the behavior of Floquet systems. The quasienergy operator of M_{TDD} was derived in section 4.1. It is given by equations (4.2) and (4.3) and illustrated in figure 4.1. In order to understand the system's resonance and bound state spectrum, we proceed by analyzing the eigensystem of the quasienergy operator for a finite number of sites N and a cutoff Floquet index n_{max}. Numerical diagonalization yields eigenvalues ε'_α and the corresponding eigenstates $|u_\alpha\rangle\rangle$ which contain the eigenstates for all Floquet channels $\left|u_{\alpha,n}\right\rangle$ (see equation (4.3)).

To understand the relation between the transmission spectrum and the quasienergy spectrum, in figure 6.11, two cuts through the transmission heat map in the right figure 6.10 at $\mu' = 1.5$ and $\mu' = 2.2$ are plotted. For $\mu' = 1.5$, one finds that the prominent feature at $k \approx 0.65$ consists of a transmission maximum at $\varepsilon' = -1.587$ and a minimum at $\varepsilon' = -1.584$. At $\mu' = 2.2$, the transmission maximum is broadened and shifted to $\varepsilon' = -1.680$ and the sharp minimum disappeared.

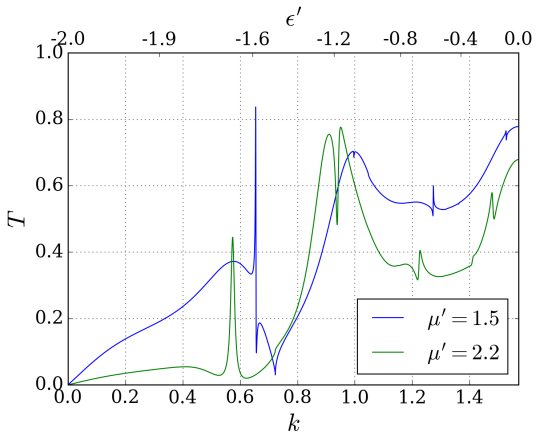

Figure 6.11: Transmission spectrum for two driven impurities at a distance $l = 5$, driven at a frequency $\omega' = 0.5$ at different driving amplitudes. A homogeneous chain with $J'_{\mathrm{imp}} = 1$ is considered. These plots present cuts through the right plot in figure 6.10.

In figure 6.12, those eigenstates of the quasienergy operator for a finite system size are plotted, whose energies are the closest to the sharp features in the transmission spectra of figure 6.11. It is apparent that, for both driving amplitudes $\mu' = 1.5$ and $\mu' = 2.2$, the transmission features occur at an energy, where the first bound channels $n \in \{-1, -2, -3\}$ feature a symmetric bound state while the propagating wavefunction in the $n = 0$ channel is strongly enhanced in between the impurities. This enhancement increases for stronger driving amplitude while the probability density in the bound

state of channel $n = -1$ decreases. This trend might explain the difference in the resonance shapes which is visible in figure 6.11: At low driving strengths, Fano interference with the discrete state of channel $n = -1$ dominates the transmission spectrum and leads to the asymmetric line shape with a sharply peaked transmission spectrum. In turn, for stronger driving amplitudes, the wavefunction enhancement in the zeroth channel increases which yields a cavity-like mode and thus a broader and more symmetric resonance shape with a prominent transmission maximum. Similar cavity modes have already been identified for the high frequency effective model M_{HFD} in section 5.3.3.

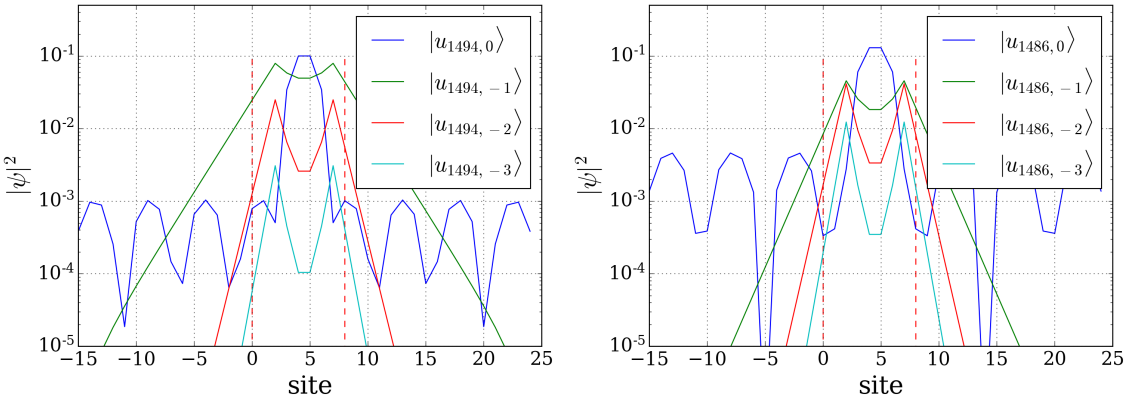

Figure 6.12: Eigenstates of the quasienergy operator with quasienergies that are the closest to the sharp transmission features in the spectra of figure 6.11. Those components of the eigenstates $|u_{\alpha,n}\rangle$ are plotted which correspond the the propagating channel $n = 0$ and the first bound channels $n \in \{-1, -2, -3\}$. They are obtained by diagonalizing the quasienergy operator for a finite system of $N = 40$ sites with impurities at a relative distance of $l = 5$ sites which are driven at frequency $\omega' = 0.5$. The cutoff Floquet index is $n_{\mathrm{max}} = 40$. The index α indicates the number of the eigenstate out of all $(2n_{\mathrm{max}} + 1) \cdot N$ eigenstates. The impurity sites are indicated by red dashed lines. Due to the logarithmic scaling, localized bound states can be easily distinguished from propagating states. Left: $\mu' = 1.5$, quasienergy $\varepsilon'_{1494} = -1.586$. Right: $\mu' = 2.2$, quasienergy $\varepsilon'_{1486} = -1.681$.

Furthermore, it is instructive to perform a similar comparison between transmission spectrum and eigenstates of the quasienergy operator at the broad transmission peak around $\varepsilon' \approx -1.15$ that features a little dip at $\varepsilon' = -1.086$ for $\mu' = 1.5$ and at $\varepsilon' = -1.183$ for $\mu' = 2.2$. Similarly to figure 6.12, in figure 6.13, those eigenstates are plotted whose quasienergies are the closest to the small dips in the transmission spectra. One observes that the corresponding eigenstates look very similar to those plotted in figure 6.12, with the difference that all channels are shifted by one: The enhanced wavefunction is now observed in channel $n = -1$ whereas the channels $n = -2$ and $n = -3$ show bound states. The fact that these eigenstates are located almost exactly at the energies of the small dips in transmission, suggests that the dips are the result of Fano interference between the propagating states in channels $n \geq -1$ and the bound states in channels $n \leq -2$.

By analyzing the eigensystem of the quasienergy operator we have, thus, demonstrated that the repeating resonances illustrated in figure 6.10 are due to a combined effect of Fano interference and cavity effects. At low driving amplitudes, it was shown that Fano interference leads to sharp drops in the transmission probability. For increasing driving strength, the two impurities produce an enhancement of the propagating wavefunction which is accompanied by an increase in transmission. This is, again, the cavity-like behavior that has already been observed for the effective high frequency model M_{HFD} in section 5.3.3. At intermediate driving amplitudes $\mu' \approx 1.5$, a competition between

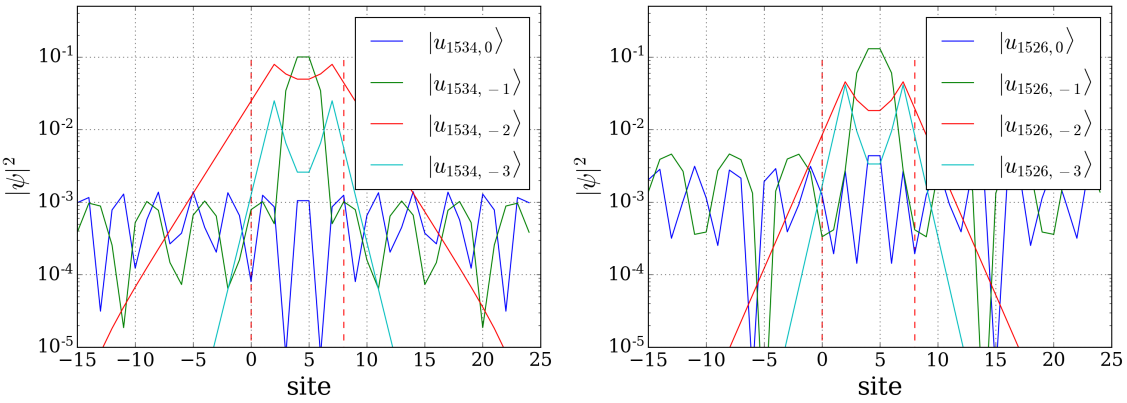

Figure 6.13: Eigenstates of the quasienergy operator with quasienergies that are the closest to the small transmission dips around $\varepsilon' \approx -1.15$ in the spectra of figure 6.11. Those components of the eigenstates $\left|u_{\alpha,n}\right\rangle$ are plotted which correspond the the propagating channel $n = 0$ and the first bound channels $n \in \{-1, -2, -3\}$. They are obtained by diagonalizing the quasienergy operator for a finite system of $N = 40$ sites with impurities at a relative distance of $l = 5$ sites which are driven at frequency $\omega' = 0.5$. The cutoff Floquet index is $n_{\max} = 40$. The index α indicates the number of the eigenstate out of all $(2n_{\max} + 1) \cdot N$ eigenstates. The impurity sites are indicated by red dashed lines. Left: $\mu' = 1.5$, quasienergy $\varepsilon'_{1534} = -1.086$. Right: $\mu' = 2.2$, quasienergy $\varepsilon'_{1526} = -1.181$.

these two effects was observed.

Finally, let us discuss the broad transmission maximum that occurs at $\varepsilon' \approx -1.1$, independently of the driving strength (see right figure 6.10). One finds that, at this energy, the $n = -1$ channel is unbound and, at all driving strengths, exhibits a confined mode. Two examples of these confined modes are illustrated in figure 6.14. In fact, for the given frequency $\omega' = 0.5$ and distance between impurities $l = 5$, exactly at energy $\varepsilon' = -1.118$, the momentum in channel $n = -1$ is (equation (4.14))

$$\varepsilon' - \omega' = -2\cos(k_{-1}) \qquad \Rightarrow \qquad k_{-1} = \arccos\left(\frac{\varepsilon' - \omega'}{-2}\right) = \frac{\pi}{l}$$

which is the characteristic condition for the first mode of a cavity. This observation suggests that a prominent, μ'-independent transmission maximum appears, whenever the $n = -1$ channel exhibits a cavity mode.

To investigate this assumption, consider figure 6.15, where, with respect to the right figure 6.10, the distance between impurities was increased from $l = 5$ to $l = 8$. Here, the first cavity mode in channel $n = -1$, $k_{-1} = n\pi/l$, gives an expected transmission maximum at energy $\varepsilon' = -1.348$ which is highlighted in figure 6.15. It is apparent that this mode is clearly accompanied by a μ'-independent increase in transmission. To identify this cavity mode in the quasienergy operator's eigensystem, in figure 6.16, eigenstates for different driving strengths are plotted, where the cavity-like wavefunction enhancement is visible. Indeed, independently of μ', these eigenstates lie close the highlighted energy of figure 6.15. This confirms the assumption that the cavity-like behavior of channel $n = -1$ leads to a transmission maximum which does not depend on the driving strength. For energies $0 < \varepsilon' < 2$, the $n = 1$ channel takes the same role.

With this explanation of the prominent μ'-independent transmission maximum, we can close the

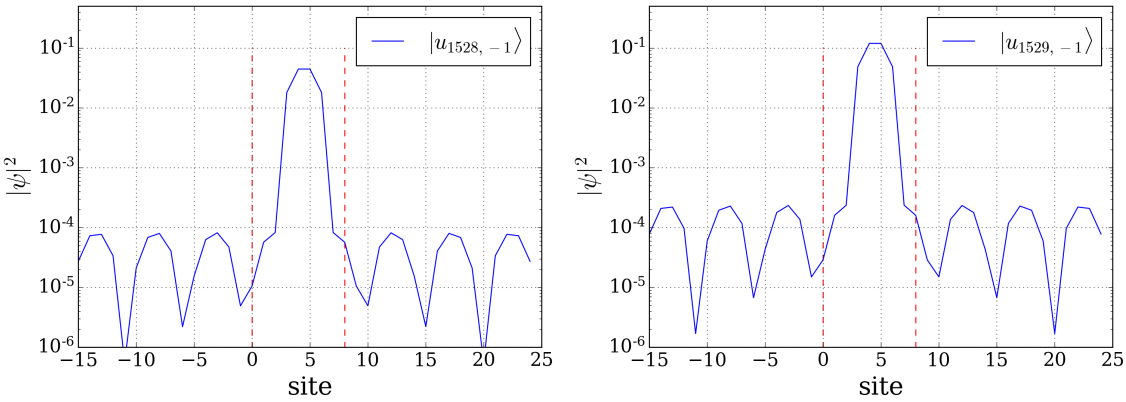

Figure 6.14: Eigenstates of the quasienergy operator where the $n = -1$ channel has a confined mode with $k_{-1} \approx \frac{\pi}{l}$. The components of the eigenstates $\left|u_{\alpha,-1}\right\rangle$ in the propagating channel $n = -1$ are plotted. It seems like these states lead to a μ'-independent transmission maximum. They are obtained by diagonalizing the quasienergy operator for a finite system of $N = 40$ sites with impurities at a relative distance of $l = 5$ sites which are driven at frequency $\omega' = 0.5$. The cutoff Floquet index is $n_{\max} = 40$. The index α indicates the number of the eigenstate out of all $(2n_{\max} + 1) \cdot N$ eigenstates. The impurity sites are indicated by red dashed lines. Left: $\mu' = 3.2$, quasienergy $\varepsilon'_{1528} = -1.137$. Right: $\mu' = 4.5$, quasienergy $\varepsilon'_{1529} = -1.138$.

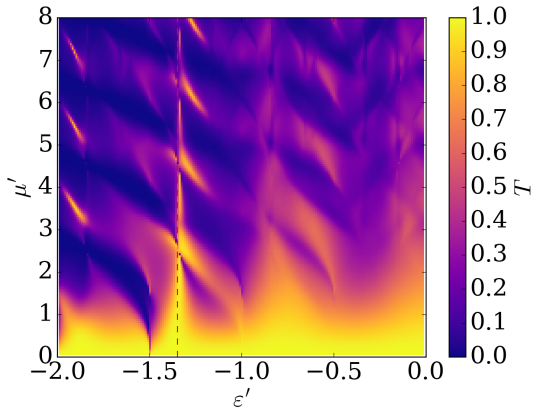

Figure 6.15: Transmission spectrum of M_{TDD} for two driven impurities at a distance $l = 8$ and driven at $\omega' = 0.5$. The system is homogeneous with $J'_{\mathrm{imp}} = 1$. A comparison to the right figure 6.10 illustrates the influence of the distance in between impurities. At the highlighted energy, channel $n = -1$ exhibits a cavity mode with $k_{-1} = \pi/l$ which is clearly accompanied by a transmission maximum.

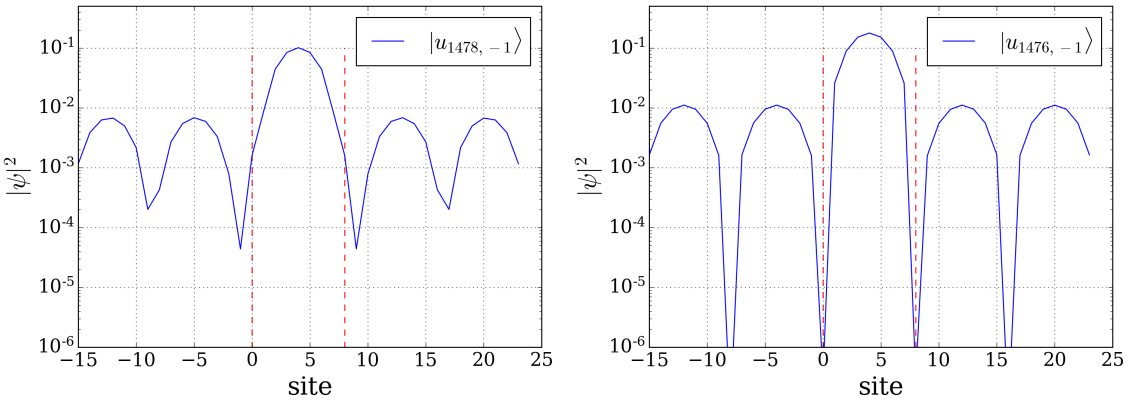

Figure 6.16: Eigenstates of the quasienergy operator where the $n = -1$ channel has a confined mode with $k_{-1} \approx \frac{\pi}{l}$. It appears like these states lead to a μ'-independent transmission maximum. The components of the eigenstates $\left|u_{\alpha,-1}\right\rangle$ in the propagating channel $n = -1$ are plotted. It seems like these states lead to a μ'-independent transmission maximum. They are obtained by diagonalizing the quasienergy operator for a finite system of $N = 39$ sites with impurities at a relative distance of $l = 8$ sites which are driven at frequency $\omega' = 0.5$. The cutoff Floquet index is $n_{\max} = 40$. The index α indicates the number of the eigenstate out of all $(2n_{\max} + 1) \cdot N$ eigenstates. The impurity sites are indicated by red dashed lines. Left: $\mu' = 3.2$, quasienergy $\varepsilon'_{1478} = -1.323$. Right: $\mu' = 4.5$, quasienergy $\varepsilon'_{1476} = -1.348$.

discussion of the driven discrete model with two impurities. We used the analogy between the continuous model M_{TDC} and the discrete model M_{TDD} at low driving amplitudes, to associate peaked drops in the transmission amplitude to Fano interference effects between propagating states interacting with discrete states of bound channels. By diagonalizing the quasienergy operator, we found that, for increasing driving amplitude, these Fano resonances compete with cavity resonances which stem from a wavefunction enhancement between the impurities. These cavity effects were shown to lead to a broader and more symmetric resonance shape and a transmission maximum. Furthermore, a prominent, driving-amplitude-independent transmission maximum was associated to the cavity mode of the first side channel.

CHAPTER 7

Conclusion

In this work, the transport properties of a one-dimensional tight binding system with two periodically driven impurities was analyzed. The unperturbed system is described by bulk hopping amplitude J, hopping amplitudes to the impurities J_1 and J_2 and the distance l between impurities. The external driving fields oscillate at frequency ω, a relative phase ϕ and at driving amplitudes μ_1 and μ_2 at the first and second impurity respectively. Floquet theory was applied to the periodically time-dependent Hamiltonian to derive the system's time-independent quasienergy operator. It consists of an infinite set of Floquet replicas of the original tight binding chain which lie at quasienergies shifted by integer multiples of $\pm\hbar\omega$. In this way, the original one-dimensional Hilbert space was extended by an additional virtual dimension. We found that at the impurity sites each Floquet channel couples to the energetically neighboring channels with coupling constant $\mu_i/2$, $i \in \{1, 2\}$.

In order to characterize the system's transport properties, we then considered the limit of high driving frequencies $\omega/J \to \infty$. In this limit, we found that the original model reduces to an effective time-independent model where the impurities are represented by effective hopping amplitudes $J_{i,\mathrm{eff}}$, $i \in \{1, 2\}$, which depend on the original impurity hopping amplitude J_i and μ/ω. It was shown that in the continuum limit of vanishing lattice spacing a, while keeping Ja^2 finite, the change in hopping amplitudes at the impurity sites corresponds to a position-dependent mass in a continuous system. An expression for this position-dependent mass was found which was transformed into an effective potential consisting of two static delta potential peaks at the positions of the impurities. We demonstrated that the transmission spectrum of this analogue continuous model coincides with the spectrum of the discrete high frequency model in the limit of small momenta k when they are scaled in terms of the inverse lattice spacing.

We then made use of the analogy between high frequency discrete and continuous model to explain the transport features of the discrete model. In contrast to a single impurity, for the case of symmetric impurities with $J_{\mathrm{eff}} = J_{1,\mathrm{eff}} = J_{2,\mathrm{eff}}$ perfect transmission peaks were observed whose width and value depend on the effective impurity hopping amplitude J_{eff} and l. In the limit of strong impurities $J_{\mathrm{eff}} \to 0$, these peaks coincide with infinitely sharp resonances of the transmission amplitude. The peaks are furthermore accompanied by a strong enhancement of the wavefunction in between impurities. These features suggest that in the regime $J_{\mathrm{eff}} \to 0$ the high frequency model behaves like an optical cavity which leads to the interpretation of the confined wavefunctions as cavity modes.

Outside of the limit $J_{\mathrm{eff}} \to 0$, the sharp transmission peaks were observed to broaden and the momenta of perfect transmission shifted. These effects were explained by broader transmission

resonances, such that multiple resonances contribute to a single transmission peak. When leaving the limit $J_{\text{eff}} \to 0$, the wavefunction enhancement was observed to decrease. However, confined modes were still demonstrated to be present at the momenta of perfect transmission. For a certain value of the effective hopping amplitude $J_{\text{eff}} > 1$, a threshold anomaly was identified, which is the critical phenomenon of perfect transmission at zero momentum. This feature was associated to the appearance of a second bound state at this value of the hopping amplitude which boosts the transmission probability at vanishing momenta.

The discussion of the high frequency limit was finalized by considering asymmetric impurities $J_{1,\text{eff}} \neq J_{2,\text{eff}}$. In this case, transmission peaks are still observed but generally do not reach perfect transmission. However, we found that for effective hopping amplitudes above a certain threshold value, an asymmetric combination of hopping amplitudes can be found where perfect transmission occurs exactly at momenta $k = n\pi/l$. As in the symmetric case, these transmission peaks are accompanied by confined wavefunctions which yet do not reach the enhancement in between symmetric impurities. Furthermore, at asymmetric effective hopping amplitudes, the threshold anomaly leads to a finite, but not perfect transmission probability at vanishing momentum.

After the analysis of the high frequency limit, we returned to the Floquet picture of multiple replicas of the original chain which lie at equidistant quasienergies and couple to each other at the impurity sites. As in the high frequency limit, a general analogue continuous model to the Floquet picture was derived where the discrete tight binding chains are replaced by continuous channels. It was found that the two models coincide in the simultaneous limits of small momenta and small driving frequency. This analogy was utilized to gain analytic insight into the multichannel transport problem at hand.

To this end, first, previous results on transmission through a single driven impurity were summarized. It was explained that a given Floquet channel only contributes to the total transmission when it supports propagating solutions, that is when its quasienergy lies within the energy continuum. Otherwise, the channel only features bound solutions. Whilst these bound states do not directly contribute to particle transmission, due to the interaction between channels, they can influence propagating states in neighboring channels. This effect is called Fano interference and, for single impurities, was observed to produce resonances of zero transmission.

The same effect of Fano interference was found to occur with two driven impurities. At weak driving amplitudes, the resulting Fano resonances were shown to produce very sharp dips in the transmission spectra. At stronger driving amplitudes, these Fano resonances were demonstrated to compete with cavity-like wavefunction enhancement in between the impurities. As in the high frequency model, this enhancement was observed to produce broad transmission maxima which dominate the Fano effects at large driving amplitudes.

The discussion of asymmetric impurities outside of the high frequency limit remains for future work. The same holds for the discussion of a nonzero phase between the driving fields. Moreover, an interesting direction of further research would be the addition of an interaction between multiple particles. For sufficiently large interaction, the formation of pairs is expected which may exhibit very different transmission characteristics as single particles.

Bibliography

[1] V. B. and Alberto Credi and Margherita Venturi, *Molecular Devices and Machines*, John Wiley and Sons, Ltd, 2008, ISBN: 9783527621682, eprint: https://onlinelibrary.wiley.com/doi/pdf/10.1002/9783527621682, URL: https://onlinelibrary.wiley.com/doi/abs/10.1002/9783527621682 (cit. on p. 1).

[2] L. Shen et al., *Electron Transport Properties of Atomic Carbon Nanowires between Graphene Electrodes*, Journal of the American Chemical Society **132** (2010) 11481, PMID: 20677763, eprint: https://doi.org/10.1021/ja909531c, URL: https://doi.org/10.1021/ja909531c (cit. on p. 1).

[3] S. P. Giblin et al., *Rectification in mesoscopic alternating current-gated semiconductor devices*, Journal of Applied Physics **114** (2013) 164505, eprint: https://doi.org/10.1063/1.4825329, URL: https://doi.org/10.1063/1.4825329 (cit. on p. 1).

[4] I. Bloch, *Ultracold quantum gases in optical lattices*, Nature Physics **1** (2005) 23, ISSN: 1745-2481, URL: https://doi.org/10.1038/nphys138 (cit. on p. 1).

[5] N. Spethmann et al., *Dynamics of Single Neutral Impurity Atoms Immersed in an Ultracold Gas*, Phys. Rev. Lett. **109** (23 2012) 235301, URL: https://link.aps.org/doi/10.1103/PhysRevLett.109.235301 (cit. on p. 1).

[6] R. Scheunemann, F. S. Cataliotti, T. W. Hänsch, and M. Weitz, *An optical lattice with single lattice site optical control for quantum engineering*, Journal of Optics B: Quantum and Semiclassical Optics **2** (2000) 645, URL: https://dx.doi.org/10.1088/1464-4266/2/5/312 (cit. on p. 1).

[7] C. Weitenberg et al., *Single-spin addressing in an atomic Mott insulator*, Nature **471** (2011) 319 (cit. on p. 1).

[8] D. W. Hone and M. Holthaus, *Locally disordered lattices in strong ac electric fields*, Phys. Rev. B **48** (20 1993) 15123, URL: https://link.aps.org/doi/10.1103/PhysRevB.48.15123 (cit. on p. 1).

[9] G. Floquet, *Sur les équations différentielles linéaires à coefficients périodiques*, Annales Scientifiques De L Ecole Normale Superieure **12** (1883) 47 (cit. on pp. 1, 5).

[10] J. H. Shirley, *Solution of the Schrödinger Equation with a Hamiltonian Periodic in Time*, Phys. Rev. **138** (4B 1965) B979, URL: https://link.aps.org/doi/10.1103/PhysRev.138.B979 (cit. on pp. 1, 5).

[11] H. Sambe, *Steady States and Quasienergies of a Quantum-Mechanical System in an Oscillating Field*, Phys. Rev. A **7** (6 1973) 2203, URL: https://link.aps.org/doi/10.1103/PhysRevA.7.2203 (cit. on pp. 1, 5).

[12] A. Eckardt and E. Anisimovas, *High-frequency approximation for periodically driven quantum systems from a Floquet-space perspective*, New Journal of Physics **17** (2015) 093039, URL: https://doi.org/10.1088/1367-2630/17/9/093039 (cit. on pp. 1, 5–8).

[13] H. Lignier et al., *Dynamical Control of Matter-Wave Tunneling in Periodic Potentials*, Phys. Rev. Lett. **99** (22 2007) 220403, URL: https://link.aps.org/doi/10.1103/PhysRevLett.99.220403 (cit. on p. 1).

[14] A. Alberti, G. Ferrari, V. V. Ivanov, M. L. Chiofalo, and G. M. Tino, *Atomic wave packets in amplitude-modulated vertical optical lattices*, New Journal of Physics **12** (2010) 065037, URL: https://dx.doi.org/10.1088/1367-2630/12/6/065037 (cit. on p. 1).

[15] M. Aidelsburger et al., *Experimental Realization of Strong Effective Magnetic Fields in an Optical Lattice*, Phys. Rev. Lett. **107** (25 2011) 255301, URL: https://link.aps.org/doi/10.1103/PhysRevLett.107.255301 (cit. on p. 1).

[16] A. Zenesini, H. Lignier, D. Ciampini, O. Morsch, and E. Arimondo, *Coherent Control of Dressed Matter Waves*, Phys. Rev. Lett. **102** (10 2009) 100403, URL: https://link.aps.org/doi/10.1103/PhysRevLett.102.100403 (cit. on p. 1).

[17] M. Bakhtiari, P. Vignolo, and M. Tosi, *Coherent transport in linear arrays of quantum dots: The effects of period doubling and of quasi-periodicity*, Physica E: Low-dimensional Systems and Nanostructures **28** (2005) 385, ISSN: 1386-9477, URL: https://www.sciencedirect.com/science/article/pii/S1386947705002146 (cit. on p. 1).

[18] X.-G. Zhang, P. S. Krstić, and W. H. Butler, *Generalized tight-binding approach for molecular electronics modeling*, International Journal of Quantum Chemistry **95** (2003) 394 (cit. on p. 1).

[19] A. Tikhonov, R. D. Coalson, and Y. Dahnovsky, *Calculating electron transport in a tight binding model of a field-driven molecular wire: Floquet theory approach*, The Journal of Chemical Physics **116** (2002) 10909, eprint: https://doi.org/10.1063/1.1448292, URL: https://doi.org/10.1063/1.1448292 (cit. on p. 1).

[20] C. Eckhardt et al., *Quantum Floquet engineering with an exactly solvable tight-binding chain in a cavity*, Communications Physics **5** (2021) 1 (cit. on p. 1).

[21] D. Thuberg, S. A. Reyes, and S. Eggert,
Quantum resonance catastrophe for conductance through a periodically driven barrier,
Phys. Rev. B **93** (18 2016) 180301,
URL: https://link.aps.org/doi/10.1103/PhysRevB.93.180301
(cit. on pp. 1, 2, 37, 74, 77–79).

[22] H. Schmidt, K. L. Campman, A. C. Gossard, and A. Imamoğlu,
Tunneling induced transparency: Fano interference in intersubband transitions,
Applied Physics Letters **70** (1997) 3455, eprint: https://doi.org/10.1063/1.119199,
URL: https://doi.org/10.1063/1.119199 (cit. on p. 1).

[23] C. S. Kim and A. M. Satanin, *Coherent resonant transmission in temporally periodically driven potential wells: the Fano mirror*,
Journal of Physics: Condensed Matter **10** (1998) 10587,
URL: https://dx.doi.org/10.1088/0953-8984/10/47/010
(cit. on pp. 1, 2, 74–77, 82).

[24] C. S. Kim and A. M. Satanin,
Coherent interaction of Fano resonances in nonstationary quantum structures,
Physica E: Low-dimensional Systems and Nanostructures **5** (1999) 62, ISSN: 1386-9477,
URL: https://www.sciencedirect.com/science/article/pii/S1386947799000302
(cit. on pp. 1, 81, 83, 84).

[25] K. K. Das, J. Garner, and K. Ruppert,
Dynamical resonances and stepped current in an attractive quantum pump,
Phys. Rev. A **97** (3 2018) 033614,
URL: https://link.aps.org/doi/10.1103/PhysRevA.97.033614 (cit. on p. 1).

[26] S. A. Reyes, D. Thuberg, D. Pérez, C. Dauer, and S. Eggert,
Transport through an AC-driven impurity: Fano interference and bound states in the continuum,
New Journal of Physics **19** (2017) 043029,
URL: https://doi.org/10.1088/1367-2630/aa66fe
(cit. on pp. 1, 2, 13, 15, 17, 18, 29, 37, 74, 75, 77–80).

[27] F. Hübner, C. Dauer, S. Eggert, C. Kollath, and A. Sheikhan,
Floquet-engineered pair and single-particle filters in the Fermi-Hubbard model,
Phys. Rev. A **106** (4 2022) 043303,
URL: https://link.aps.org/doi/10.1103/PhysRevA.106.043303
(cit. on pp. 2, 37, 74).

[28] F. Hübner, *Bound Pairs Scattering off a Floquet Driven Impurity*,
MA thesis: Rheinische Friedrich-Wilhelms-Universität Bonn, 2021 (cit. on pp. 20, 21).

[29] K. Takegoshi, K. Sharma, N. Miyazawa, and P. Madhu,
Comparison among Magnus/Floquet/Fer expansion schemes in solid-state NMR,
The Journal of Chemical Physics **142** (2015) 1 (cit. on p. 21).

[30] *NIST Digital Library of Mathematical Functions*,
http://dlmf.nist.gov/, Release 1.1.6 of 2022-06-30,
F. W. J. Olver, A. B. Olde Daalhuis, D. W. Lozier, B. I. Schneider, R. F. Boisvert, C. W. Clark, B. R. Miller, B. V. Saunders, H. S. Cohl, and M. A. McClain, eds.,
URL: https://dlmf.nist.gov/10.12 (cit. on p. 23).

[31] C.-K. Chiu, J. C. Y. Teo, A. P. Schnyder, and S. Ryu,
Classification of topological quantum matter with symmetries,
Rev. Mod. Phys. **88** (3 2016) 035005,
URL: https://link.aps.org/doi/10.1103/RevModPhys.88.035005 (cit. on p. 28).

[32] A. D. Alhaidari,
Solutions of the nonrelativistic wave equation with position-dependent effective mass,
Phys. Rev. A **66** (4 2002) 042116,
URL: https://link.aps.org/doi/10.1103/PhysRevA.66.042116 (cit. on p. 30).

[33] I. GEL'FAND and G. SHILOV, "CHAPTER I - DEFINITION AND SIMPLEST PROPERTIES OF GENERALIZED FUNCTIONS," *Properties and Operations*,
ed. by I. GEL'FAND and G. SHILOV, Academic Press, 1964 18, ISBN: 978-1-4832-2976-8,
URL:
https://www.sciencedirect.com/science/article/pii/B9781483229768500076
(cit. on p. 31).

[34] T. Pang, "Ordinary differential equations," *An Introduction to Computational Physics*, 2nd ed., Cambridge University Press, 2006 105 (cit. on pp. 32, 106, 108).

[35] E. Kujawski, *Additivity of Phase Shifts for Scattering in One Dimension*,
American Journal of Physics **39** (1971) 1248,
eprint: https://doi.org/10.1119/1.1976615,
URL: https://doi.org/10.1119/1.1976615 (cit. on p. 33).

[36] I. R. Lapidus, *Resonance scattering from a double δ-function potential*,
American Journal of Physics **50** (1982) 663 (cit. on pp. 33, 39, 40, 54).

[37] P. Senn, *Threshold anomalies in one-dimensional scattering*,
American Journal of Physics **56** (1988) 916, eprint: https://doi.org/10.1119/1.15359,
URL: https://doi.org/10.1119/1.15359 (cit. on pp. 33, 54).

[38] Z. Ahmed, S. Kumar, M. Sharma, and V. Sharma, *Revisiting double Dirac delta potential*,
European Journal of Physics **37** (2016) (cit. on pp. 33, 39, 42, 48, 51, 54, 57).

[39] D. J. Griffiths, "Time-Independent Schrödinger Equation,"
Introduction to Quantum Mechanics, Pearson Prentice Hall, 2004, chap. 2 24,
ISBN: 9780131118928 (cit. on p. 37).

[40] D. Meschede, "Coherence and Interferometry," *Optics, Light, and Lasers*,
John Wiley and Sons, Ltd, 2017, chap. 6 181, ISBN: 9783527685486,
eprint: https://onlinelibrary.wiley.com/doi/pdf/10.1002/9783527685486.ch6,
URL: https://onlinelibrary.wiley.com/doi/abs/10.1002/9783527685486.ch6
(cit. on pp. 41, 42, 44, 59).

[41] F. Schwabl, "One-Dimensional Problems," *Quantum Mechanics*,
Berlin, Heidelberg: Springer Berlin Heidelberg, 2007 47, ISBN: 978-3-540-71933-5,
URL: https://doi.org/10.1007/978-3-540-71933-5_3 (cit. on pp. 42, 43, 51).

[42] A. Uma Maheswari, P. Prema, and C. Shastry,
Resonant states and transmission coefficient oscillations for potential wells and barriers,
American Journal of Physics - AMER J PHYS **78** (2010) (cit. on pp. 42, 48).

[43] K. Rapedius,
Calculating resonance positions and widths using the Siegert approximation method,
European Journal of Physics - EUR J PHYS **32** (2011) (cit. on p. 42).

[44] S. Weinberg, "GENERAL SCATTERING THEORY," *Lectures on Quantum Mechanics*,
2nd ed., Cambridge University Press, 2015 282 (cit. on p. 53).

[45] P. F. Bagwell and R. K. Lake, *Resonances in transmission through an oscillating barrier*,
Phys. Rev. B **46** (1992) 15329,
URL: https://link.aps.org/doi/10.1103/PhysRevB.46.15329
(cit. on pp. 65, 74, 75).

[46] F. Schwabl, "The Wave Function and the Schrödinger Equation," *Quantum Mechanics*,
Berlin, Heidelberg: Springer Berlin Heidelberg, 2007 13, ISBN: 978-3-540-71933-5,
URL: https://doi.org/10.1007/978-3-540-71933-5_2 (cit. on p. 69).

[47] J. A. Støvneng and E. H. Hauge, *The Büttiker-Landauer model generalized*,
Journal of Statistical Physics **57** (1989) 841,
eprint: https://doi.org/10.1007/BF01022836,
URL: https://doi.org/10.1007/BF01022836 (cit. on pp. 74, 75).

[48] D. F. Martinez and L. E. Reichl, *Transmission properties of the oscillating δ-function potential*,
Phys. Rev. B **64** (24 2001) 245315,
URL: https://link.aps.org/doi/10.1103/PhysRevB.64.245315 (cit. on pp. 74, 75).

[49] U. Fano, *Effects of Configuration Interaction on Intensities and Phase Shifts*,
Phys. Rev. **124** (6 1961) 1866,
URL: https://link.aps.org/doi/10.1103/PhysRev.124.1866 (cit. on p. 77).

[50] J. von Neumann and E. P. Wigner, "Über merkwürdige diskrete Eigenwerte," vol. 30,
Stuttgart: S. Hirzel Verlag, 1929 465 (cit. on p. 79).

[51] F. H. Stillinger and D. R. Herrick, *Bound states in the continuum*,
Phys. Rev. A **11** (2 1975) 446,
URL: https://link.aps.org/doi/10.1103/PhysRevA.11.446 (cit. on p. 79).

[52] S. Longhi and G. D. Valle, *Floquet bound states in the continuum*,
Scientific Reports **3** (2013) 2219, URL: https://doi.org/10.1038/srep02219
(cit. on p. 79).

[53] C. S. Kim and A. M. Satanin,
Dynamic confinement of electrons in time-dependent quantum structures,
Phys. Rev. B **58** (23 1998) 15389,
URL: https://link.aps.org/doi/10.1103/PhysRevB.58.15389 (cit. on p. 81).

[54] Z. Fedorova et al., *Limits of topological protection under local periodic driving*, Light: Science and Applications **8** (2019) 63 (cit. on p. 103).

APPENDIX A

Time evolution in the Floquet picture

As explained in section 4.1 the time evolution of the tight binding chain with two periodically driven impurities can be obtained by solving the Floquet equation 3.10, that is by diagonalizing the quasienergy operator $\bar{Q}$ of this equation. According to equation 3.9, the extended Hilbert space, where the quasienergy operator lives, is given by the product of the Hilbert space of the quantum mechanical system, which for an infinite tight binding chain is infinite dimensional, and the infinite dimensional space of T-periodically time dependent functions. In order to numerically diagonalize the quasienergy operator one therefore needs to approximate the quasienergy operator as a finite dimensional matrix. The physical Hilbert space can be made finite by considering a finite chain of N sites. Similarly $\mathcal{L}_T$ can be made finite by choosing some cutoff Fourier index $n_{\max}$.

The explicit form of the Floquet equation for the tight binding chain with two driven impurities is given by equation 4.3. It states that numerical diagonalization yields quasienergies ε_n with corresponding eigenstates $|u_\alpha\rangle\!\rangle$ that contain the eigenstates all all Floquet channels $|u_{\alpha n}\rangle$ labeled by the Floquet indices $n \in \{-n_{\max}, -n_{\max}+1, ..., n_{\max}\}$. The time evolution of any initial wavefunction can be determined as explained in [54]. As explained in section 3.2, this eigensystem contains a lot of redundant information and can be reduced by considering eigenvalues within an energy interval of width $\hbar\omega$. We can therefore limit the analysis to those eigenvalues within the first Floquet Brillouin zone $\varepsilon \in [-\omega/2, \omega/2]$.

According to equation 3.6, for a given index α, the quasienergy of the Floquet mode $|u_{\alpha n}\rangle$ is given by $\varepsilon_{\alpha n} = \varepsilon_\alpha + n\hbar\omega$. The time evolution of a given initial wavefunction $|\psi(0)\rangle$ can then be calculated as [54]

$$|\psi(t)\rangle = \sum_\alpha c_\alpha \sum_n \exp(-i\varepsilon_{\alpha n} t)\, |u_{\alpha n}\rangle$$

where the coefficients

$$c_\alpha = \langle u_\alpha(0)|\psi(0)\rangle$$

c_α are calculated from the initial wavefunction. Here, the Floquet mode at $t = 0$ is given by

$$|u_\alpha(0)\rangle = \sum_n |u_{\alpha n}\rangle\,.$$

This formalism illustrates the simplicity of determining a wavefunction's time evolution by means of the Floquet formalism. The presented method can be utilized to depict the scattering process of an incoming Gaussian wave packet

$$\left|\psi_{\mathrm{wp}}(t)\right\rangle = \sum_j \exp\left(-\frac{(j-j_0)^2}{2\sigma} + ikj\right) c_j^\dagger \left|0\right\rangle$$

initially centered around site j_0 with width σ. For a given set of system and driving parameters, this scattering process is illustrated in figure A.1. The plots nicely show a decrease in transmission for altered driving amplitude which is predicted from the transmission spectrum in the right figure 6.10. In principle, the transmission probability can be calculated from the analysis of such scattering processes. However, compared to the method presented in section 4.2, the calculation of the wavefunction after the scattering process $\left|\psi_{\mathrm{wp}}(t_\mathrm{f})\right\rangle$ is computationally more costly. Furthermore, the initial wave packet features a finite momentum bandwidth which reduces the momentum resolution of the scattering process.

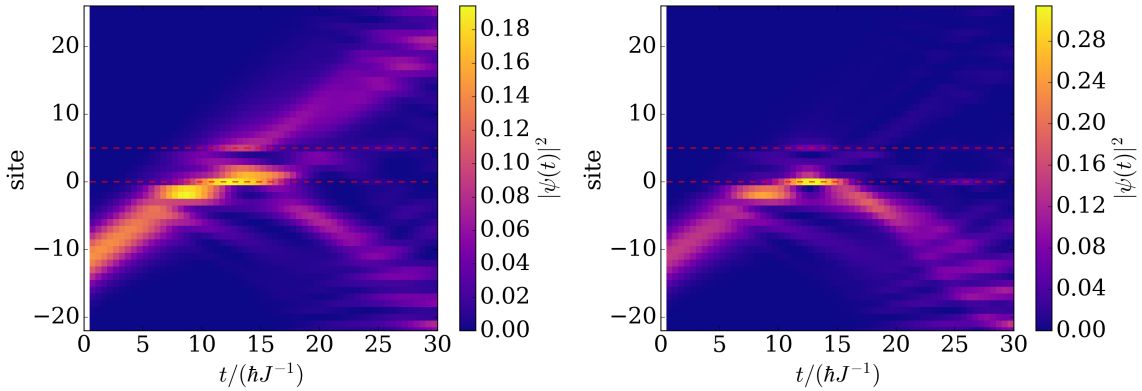

Figure A.1: Time evolution of incoming wave packets of energy $\epsilon' = -1.6$ on a homogeneous tight binding chain with $J'_{\mathrm{imp}} = 1$ scattered at two impurities at a distance of $l = 5$ driven at frequency $\omega' = 0.5$. The cutoff parameters to make system finite are chosen as $N = 50$ and $n_{\mathrm{max}} = 20$. The red dashed lines indicate the impurity sites. Left: driving amplitude $\mu' = 1$. Right: driving amplitude $\mu' = 2$. These scattering processes can be compared to the transmission spectrum in the right figure 6.10 which indeed show a drop in transmission at $\mu' = 2$ compared to $\mu' = 1$.

APPENDIX B

Supplements to the high frequency limit

B.1 High frequency transmission rewritten

In this appendix, a different way to write equation (5.23) is given which describes particle transmission in the high frequency discrete model M_{HFD}. Using various addition theorems for triangular functions, one obtains the following representation:

$$
\begin{aligned}
T =& 8(J'_{1,\mathrm{eff}})^4 (J'_{2,\mathrm{eff}})^4 \sin^4(k) \\
&\cdot \left(\left(-\frac{16}{7}(J'_{1,\mathrm{eff}})^2 (J'_{2,\mathrm{eff}})^2 + \left((J'_{1,\mathrm{eff}})^2 + (J'_{2,\mathrm{eff}})^2 \right)^2 + 7 \left((J'_{1,\mathrm{eff}})^4 - \frac{4}{7}(J'_{1,\mathrm{eff}})^2 \right) \left((J'_{2,\mathrm{eff}})^4 - \frac{4}{7}(J'_{2,\mathrm{eff}})^2 \right) \right) \right. \\
&\quad + 8\cos(2k) \left(\left((J'_{1,\mathrm{eff}})^2 - 1 \right)^2 \left((J'_{2,\mathrm{eff}})^2 - 1 \right)^2 - \frac{1}{2}(J'_{1,\mathrm{eff}})^4 (J'_{2,\mathrm{eff}})^4 \right) \\
&\quad + \cos(4k) \left(\left((J'_{1,\mathrm{eff}})^2 - 1 \right)^2 \left((J'_{2,\mathrm{eff}})^2 - 1 \right)^2 + \left(2(J'_{1,\mathrm{eff}})^2 - 1 \right) \left(2(J'_{2,\mathrm{eff}})^2 - 1 \right) \right) \\
&\quad - 8\cos(2k)\cos(2kl) \left((J'_{1,\mathrm{eff}})^2 - 1 \right)^2 \left((J'_{2,\mathrm{eff}})^2 - 1 \right)^2 \\
&\quad - 2\cos(4k)\cos(2kl) \left((J'_{1,\mathrm{eff}})^2 - 1 \right) \left((J'_{2,\mathrm{eff}})^2 - 1 \right) \left(2(J'_{1,\mathrm{eff}})^2 (J'_{2,\mathrm{eff}})^2 - (J'_{1,\mathrm{eff}})^2 - (J'_{2,\mathrm{eff}})^2 + 1 \right) \\
&\quad - 16\sin(k)\cos^3(k)\sin(2kl) \left((J'_{1,\mathrm{eff}})^2 - 1 \right) \left((J'_{2,\mathrm{eff}})^2 - 1 \right) \left(2(J'_{1,\mathrm{eff}})^2 (J'_{2,\mathrm{eff}})^2 - (J'_{1,\mathrm{eff}})^2 - (J'_{2,\mathrm{eff}})^2 \right) \\
&\quad \left. + 4\sin^2(kl) \left(3 \left((J'_{1,\mathrm{eff}})^2 - 1 \right)^2 \left((J'_{2,\mathrm{eff}})^2 - 1 \right)^2 - \left((J'_{1,\mathrm{eff}})^4 - (J'_{1,\mathrm{eff}})^2 \right) \left((J'_{2,\mathrm{eff}})^4 - (J'_{2,\mathrm{eff}})^2 \right) \right) \right)^{-1}
\end{aligned}
\tag{B.1}
$$

B.2 Comparison of position-dependent mass system and double delta potential

In section 5.2.1, we found that the position-dependent mass of the high frequency analogue continuous model can be translated into the potential (5.35). According to equation (5.38), in the limit of small

peak width $\sigma \to 0$, the effective potential (5.35) is expected to be described by a double Dirac delta potential. This potential is investigated in section 5.2.2. In this appendix, the numerical transmission through the effective potential (5.35) is compared to the analytical transmission through a double delta potential given by equation (5.41). We will find that, except for numerical deviations, the two models match very well.

Transport through the effective potential (5.35) is calculated numerically by means of the numerical method described in reference [34]. In figure B.1, the resulting transmission spectrum is compared to the one of the delta potential for different values of the impurities' spatial extent σ.

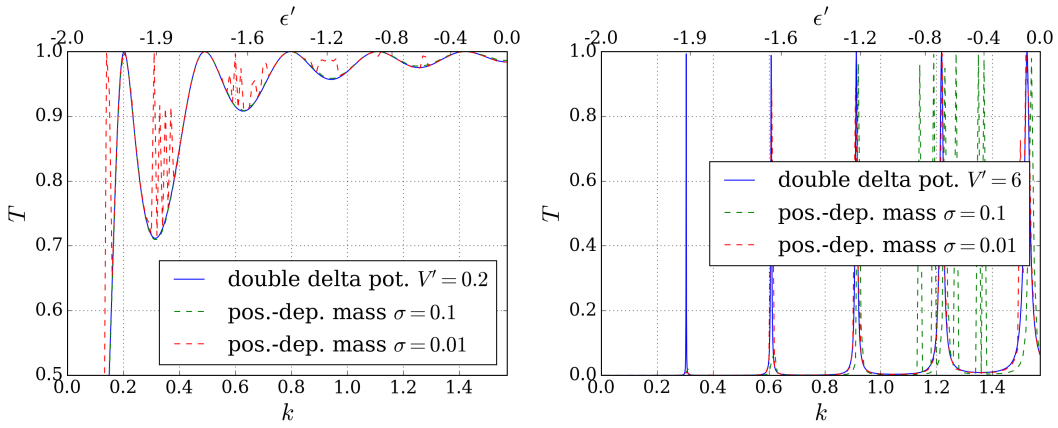

Figure B.1: Transmission through the double delta potential with $l = 10$ compared to the numerically calculated transmission through the effective potential (5.35) resulting from the position-dependent mass described in section 5.2.1 for different values of σ.

For $\sigma = 0.1$, the numerical transmission spectrum is smooth, but for the case of strong impurities, it deviates from the spectrum of the corresponding double delta potential. The spectrum for $\sigma = 0.01$ matches very well with the corresponding result for the delta potential. However, its spectrum features many spikes. Since the potential peaks are very narrow here, the numerical algorithm sometimes struggles at determining the correct wavefunction and transmission.

In figure B.2, the four momenta of perfect transmission of the double delta potential are compared to those for the position-dependent mass system, again relating the two with equation (5.38). As observed in figure B.1, the spectra seem to match very well. For $\nu \in (0, 1)$, in the limit $\sigma \to 0$, the position-dependent mass system seems to be described very well by the double delta potential. Since, in contrast to the position-dependent mass system, the double delta potential can be solved analytically, the latter system is the only one considered from section 5.2.3 on.

B.3 Resonant wavefunctions and confined eigenstates

In section 5.3.3, we found that at perfect transmission, the wavefunction of an incoming particle is enhanced in between the impurities. Furthermore, we found confined eigenfunctions of the Hamiltonian with non-degenerate eigenvalues exactly at these energies of perfect transmission.

To illustrate the relation between transmission maxima and confined modes on the one hand, and the relation between the high frequency discrete model M_{HFD} and the high frequency analogue continuous

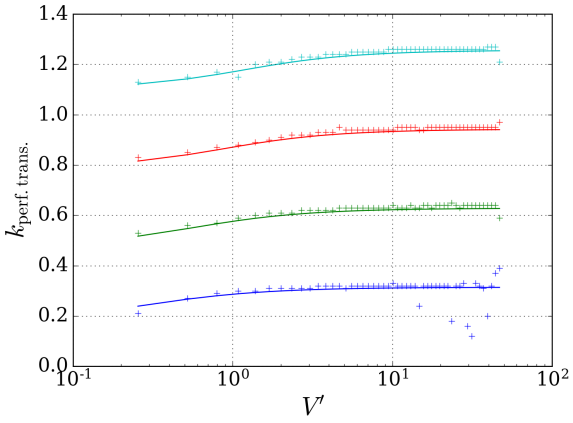

Figure B.2: The four momenta of perfect transmission for the delta potential as a function of $V_0 > 0$ (solid line) compared to the values for the corresponding position-dependent mass system with $\sigma = 0.1$ (plus symbols).

model M_{HFC} on the other hand, the following procedure is pursued:

1. For a given J', the energies of perfect transmission $\epsilon'_{\text{perf. trans.}} = -2\cos\left(k_{\text{perf.trans.}}\right)$ of M_{HFD} are determined numerically, using equation (5.23).

2. The corresponding Hamiltonian for a finite system (5.51) is diagonalized and the eigenvalues that are the closest to the energies of perfect transmission are identified. These confined eigenstates are normalized to the region in between the impurities such that

$$\sum_{j=0}^{l} |\psi_j|^2 = 1$$

   where ψ_j is the wavefunction at site j.

3. Using relation (5.42), the effective hopping amplitude J' of M_{HFD} is related to an impurity strength V' of M_{HFC}. For the determined energies of perfect transmission $\epsilon'_{\text{perf.trans.}}$, the wavefunction of M_{HFC} is determined using equations (5.39) and (5.40). In between the impurities, the wavefunction's density can be written in terms of the transmission as

$$|\psi_{\text{in btw. impurities}}(x)|^2 = T\left(1 + \frac{2V^2}{k^2}\left[1 - \cos\big(2k(x-l)\big) - \frac{k}{V}\sin\big(2k(x-l)\big)\right]\right).$$

   It is normalized to match the density of the discrete eigenstates. Since the step size is chosen as $\Delta x = 0.2$ (yielding $1/\Delta x = 5$ sampling points per discrete site), the probability density is normalized such that

$$\int_0^l \mathrm{d}x|\psi(x)|^2 = \frac{1}{\Delta x} = 5$$

4. Using relation (5.38), the double delta potential is related to the position-dependent mass system

described in section 5.2.1. For different values of the impurity extent σ, the wavefunction of a particle with the energy $\epsilon'_{\text{perf.trans.}}$ is determined numerically using the method described in reference [34]. Its probability density is normalized in the same fashion as the one of the double delta potential.

5. The probability densities of all these wavefunctions are plotted for different values of J' in figures B.3 to B.4.

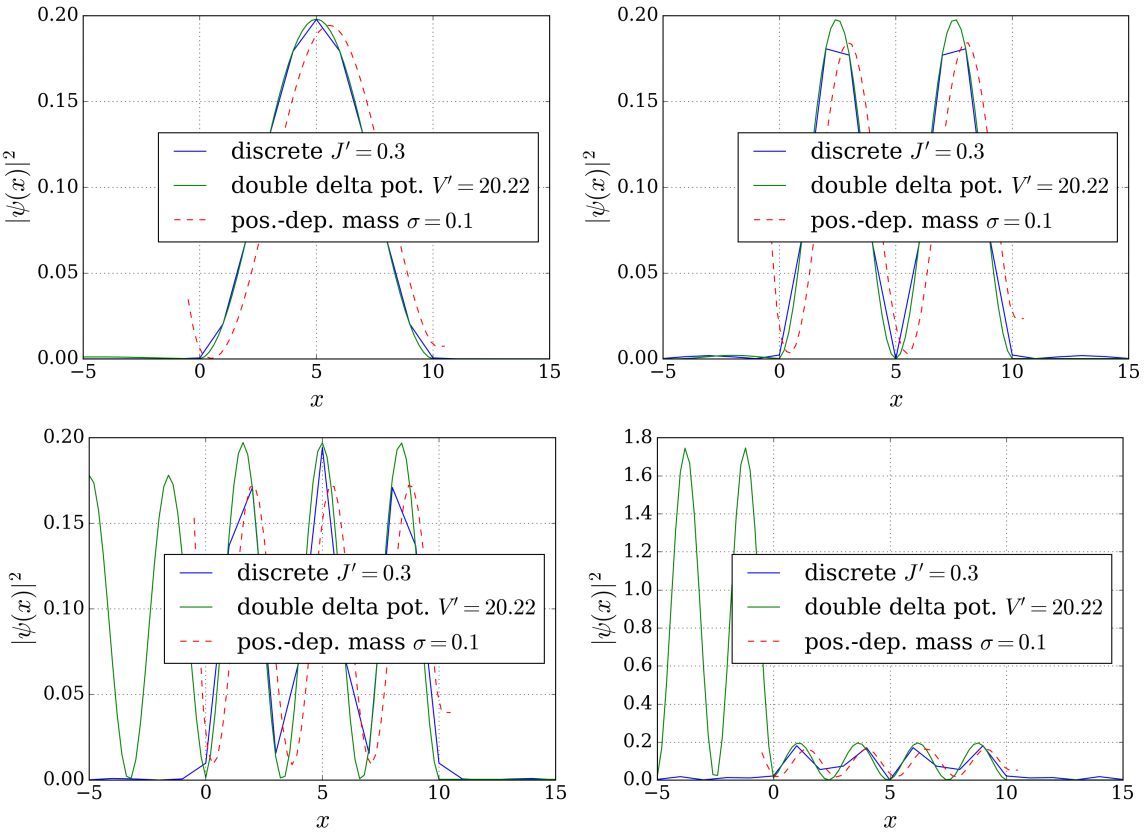

Figure B.3: Comparison of the wavefunctions at the energies of perfect transmission in the discrete model $\epsilon'_{\text{perf.trans.}}$ for $J' = 0.3$ and $l = 10$. The discrete eigenvectors are determined for a finite system size of $N = 101$ sites.

On the one hand, from these plots, one nicely sees that one is able to relate the three models (M_{HFD}, continuous model with position-dependent mass and M_{HFC}) to each other. Not only the transmission spectra match, as shown in chapter 5.3, but also the wavefunctions do, at least at the energies/momenta of perfect transmission.

Secondly, one nicely sees that in the discrete and the continuous model transmission maxima appear when the wavefunction shows a confined mode. This feature is discussed thoroughly in sections 5.3.3 and 5.3.4.

In these plots, only the case of decreased hopping amplitude $J' < 1$ and correspondingly positive delta barrier with $V' > 0$ has been analyzed. This is for the fact that, as explained in section 5.2.1,

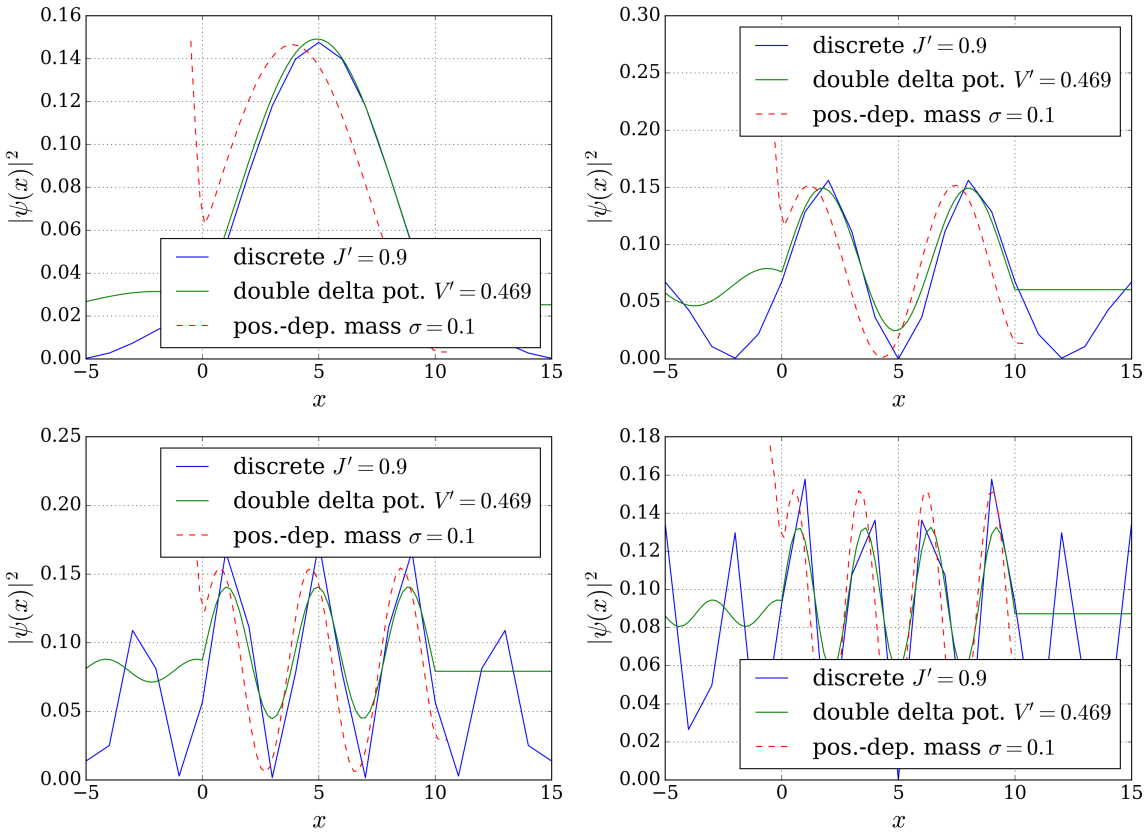

Figure B.4: Comparison of the wavefunctions at the energies of perfect transmission in the discrete model $\epsilon'_{\text{perf.trans.}}$ for $J' = 0.9$ and $l = 10$. The discrete eigenvectors are determined for a finite system size of $N = 101$ sites.

the continuous position-dependent mass system can only be quantitatively related to the double delta potential for $0 \leq \nu \leq 1$ which limits the double delta potential to $V \geq 0$. In figure 5.5, one sees that $V \geq 0$ limits the discrete system to $0 \leq J' \leq 1$. However, as discussed in section 5.3.5, one finds that $J' > 1$ relates to $V < 0$ where both models feature bound states.

List of Figures